CRANFIELD UNIVERSITY

K. GEORGIEV

BIOLOGICALLY INSPIRED PROCESSING OF RADAR AND SONAR TARGET ECHOES

CRANFIELD DEFENCE AND SECURITY
Centre for Electronic Warfare, Information and Cyber

PhD
Academic Year: 2014–2017

Supervisor: Dr A. Balleri
August 2017

CRANFIELD UNIVERSITY

CRANFIELD DEFENCE AND SECURITY
Centre for Electronic Warfare, Information and Cyber

PhD

Academic Year: 2014–2017

K. GEORGIEV

Biologically inspired processing of radar and sonar target echoes

Supervisor: Dr A. Balleri
August 2017

This thesis is submitted in partial fulfilment of the requirements for the degree of Doctor of Philosophy.

Abstract

Modern radar and sonar systems rely on active sensing to accomplish a variety of tasks, including detection and classification of targets, accurate localization and tracking, autonomous navigation and collision avoidance. Bats have relied on active sensing for over 50 million years and their echolocation system provides remarkable perceptual and navigational performance that are of envy to synthetic systems.

The aim of this study is to investigate the mechanisms bats use to process echo acoustic signals and investigate if there are lessons that can be learned and ultimately applied to radar systems. The basic principles of the bat auditory system processing are studied and applied to radio frequencies.

A baseband derivative of the Spectrogram Correlation and Transformation (SCAT) model of the bat auditory system, called Baseband SCAT (BSCT), has been developed. The BSCT receiver is designed for processing radio-frequency signals and to allow an analytical treatment of the expected performance. Simulations and experiments have been carried out to confirm that the outputs of interest of both models are “equivalent”.

The response of the BSCT to two closely spaced targets is studied and it is shown that the problem of measuring the relative distance between two targets is converted to a problem of measuring the range to a single target. Nearly double improvement in the resolution between two close scatterers is achieved with respect to the matched filter.

The robustness of the algorithm has been demonstrated through laboratory measurements using ultrasound and radio frequencies (RF). Pairs of spheres, flat plates and vertical rods were used as targets to represent two main reflectors.

Keywords

SCAT; echolocation; spectrogram transformation; high resolution; target recognition; radar; sonar; bat auditory system; eptesicus fuscus; matched filter, HRRP, close scatterers, BSCT, spacing profile, range profile, frequency profile.

Table of Contents

List of Figures

List of Tables

List of Abbreviations

ACF	Autocorrelation Function
ADC	Analogue-to-Digital Converter
BSCT	Baseband Spectrogram Correlation and Transformation
CDS	Cranfield Defence and Security
FFT	Fast Fourier Transform
FT	Fourier Transform
HRRP	High Resolution Range Profile
IF	Intermediate Frequency
IFBW	Measurement bandwidth
IFFT	Inverse Fast Fourier Transform
IFT	Inverse Fourier Transform
IIR	Infinite Impulse Response
LO	Local Oscillator
MF	Matched Filter
NLS	Nonlinear Least Square
RF	Radio Frequency
rms	Root-mean-square
SCAT	Spectrogram Correlation And Transformation
SNR	Signal-to-Noise-Ratio

VNA	Vector Network Analyzer

Acknowledgements

I would like to thank my academic supervisor Dr. Alessio Balleri for the continuous support during my long journey. I would also like to thank Dr. Andy Stove and Dr. Marc Holderied for the inspiring discussions and helpful edits of our research papers.

This work was funded by Cranfield Defence and Security under the CDS PhD bursary scheme.

Chapter 1

Introduction

Bats and other mammals use echolocation to sense the environment actively. Over a period of 50 million years, they have evolved an echolocation system that allows them to hunt insects, to forage for fruit or flowers in the presence of clutter, to manoeuvre in a complex environment and to find their way in the open space.

A close analogy can be made with modern radars and sonars which rely on active sensing to support a variety of tasks, including detection and classification of targets, accurate localization and tracking, autonomous navigation and collision avoidance. Current improvements in the radar technology bring not only design flexibility but also impose increased expectations towards synthetic systems performance.

The basic principles of echolocation and those of radar and sonar are largely the same. Bats emit an ultrasound chirp-like echolocation call (a pulse) and then listen. By analysing the echo returns they decide if there is a target or only noise. The delay in the echo is translated to distance, the strength of the echo indicates the size of the target. The change in the sound frequency (the so called Doppler effect) measures the speed of the target. More subtle changes of the "timbre" (i.e. the spectral content) of the sound can bring information about the fine structure of the reflecting objects (e.g. shape and the texture).

The similarities between natural and artificial active sensing systems can be expanded further. As in the case of the pulse radar, during transmit bat ear sensitivity is significantly reduced to prevent its damage. Both bats and radars/sonars deploy waveforms modulated in frequency. Both have to deal with the limitation of signal acquisition rate and the real time computations. The availability of energy resources can put additional constraints for applications in small autonomous devices as surveillance drones.

All these similarities mean that a lot can be learned by studying bats echolocation. However, there are various key differences to explore. Unlike radar which mostly use linear chirp, echolocation calls of frequency modulating bats can be non-linear, e.g. hyperbolic. While conventional radar rely on a small set of predetermined waveforms, bats vary multiple parameters as call duration, pulse repetition frequency, bandwidth and frequency content on pulse to pulse basis. Behavioural experiments have demonstrated that bats are able to resolve closely located scatterers. The fact that they are able to do this successfully suggests that they have access to robust "superresolution" techniques.

There is biological evidence that indicates that the way bats process signals in the receiving auditory system is not equivalent to the matched filter used in radar and sonar systems. While the aim of existing bat auditory system models is to reproduce the acoustic images as it is believed, from a variety of behavioural experiments, that bats perceive them, there is no explanation on what exactly brings the performance improvement so it could be exploited in a technological system. Therefore it will be useful to investigate differences and similarities and study how these can be used to improve the performance of synthetic sensors.

The aim of this study is to investigate the mechanisms bats use to process echo acoustic signals. The basic principles of the bat auditory system processing are extracted and applied to radio frequencies. The reason why we looked at bats is because bat echolocation is much more sophisticated than echolocation is other animals. The waveform design is so much more complex and diverse and different from environment to environment and for different type of foraging. This is not the case for dolphins for example that send clicks.

1.1 Aim and objectives

The goal of the research is to study the bat type signal processing and investigate its advantages and disadvantages for radar and sonar applications.

The broad goal was split into several more specific objectives:

- implement a prototype of the Spectrogram Correlation and Transformation (SCAT) receiver (an auditory computational models of echo-locating bats);
- carry out experiment trials to assess the output of the SCAT with real measurements;
- develop a receiver based on the SCAT (BSCT) that can process baseband signals;
- model analytically the response of the BSCT for two scatterers;
- evaluate the expected resolution performance;
- implement a prototype of the BSCT that can process time signal;
- perform measurements at ultrasound with phantom echoes and real targets;
- experimentally confirm the model performance with ultrasound;
- implement a prototype of the BSCT that can process frequency response;
- perform measurements at RF of different real targets;
- experimentally confirm that the BSCT model generalizes for higher frequency signals;

- experimentally confirm that the BSCT model is robust to real targets, noise and surroundings;

1.2 Thesis layout

The thesis is organized as follows. An overview and scoping of the study is provided in Chapter 1. A further review of bat echolocation related to perceptual capabilities and the existing bat auditory system models is presented in Chapter 2.

Chapter 3 gives a brief introduction to the main concepts and models on which this thesis is based. This includes the main forms currently used to represent deterministic and stochastic signals including matched filter compression. The Spectrogram Correlation and Transformation (SCAT) model of the bat auditory system is reviewed, implemented and discussed in the context of other monaural models.

Chapter 4 introduces the developed baseband version of the SCAT (BSCT) together with analytical treatment and discussion of the expected theoretical resolution. The performance of the BSCT is investigated theoretically for the case of two closely located targets. In Chapter 5 it is experimentally confirmed that the BSCT allows SCAT-like signal processing using ultrasound. The expected enhancement in resolution is also demonstrated. The applicability of the BSCT model at radio frequencies (RF) is the subject of Chapter 6.

A further discussion of additional research challenges relating to the developments presented in this thesis is presented in Chapter 7. In particular, an approximation of the signal-to-noise ratio, an interpretation of the model for multiple scatterers and connection with the autocorrelation function are provided.

1.3 Novel aspects of the work

The main original contributions from this thesis are:

- A baseband receiver was proposed that allows an analytical treatment of the output of a SCAT-like processing and that can also be applied to RF signals (Chapter 4).
- The output of the BSCT was derived analytically for two closely spaced scatterers and compared with that of a conventional matched filter (Chapter 4).
- Results have shown that a bat-inspired spectrogram transformation can provide better range resolution performance than that of a matched filter output envelope (Chapter 4). The problem of measuring the relative distance between two targets is converted to a problem of measuring the range to a single target.
- In Chapter 5 the equivalence between the SCAT and BSCT was demonstrated experimentally. Results show that the technique used for smoothing the output of the band-pass filters is not important for the frequency interference patterns and the corresponding fine delay profiles.
- In Chapter 5 the enhanced resolution of two scatterers was demonstrated experimentally by processing ultrasound measurements with BSCT receiver. The frequency range and bandwidth were based on bat echolocation call.
- The feasibility of the BSCT receiver for radio frequency signals was demonstrated in Chapter 6. The experimental work is an evidence that the bat-inspired approach is robust to real targets. Pairs of flat plates, vertical rods and spheres were used to represent targets with two main reflectors.
- In Chapter 6 the enhanced resolution of two scatterers was demonstrated experimentally by processing radio frequency with the BSCT receiver.

- A new interpretation of the bat-inspired model output was proposed. At local scale the target is represented by the spacing between the scatterers and not by their absolute arrangement (Chapter 7).

Additional support activities include:

- Implementation of the SCAT algorithm. It was further explored with simulated and measured data.
- Preparation of a dataset of laboratory measurements with ultrasound of two close targets at different separations. Ideal point targets were artificially created through the speaker. Two vertical rods represented the real objects. The frequency range and bandwidth were based on bat echolocation call.
- Preparation of a dataset of laboratory measurements at radio frequency of two close targets at different separations. The RF measurements were collected in the frequency domain using Vector Network Analyser. Vertical rods, flat plates and small spheres were used as main scatterers.

1.4 Publications

As a result of the work presented in this thesis the following publications have arisen:

Journal papers

- K. Georgiev, A. Balleri, A. Stove, and M. Holderied, "Bio-inspired Resolution of Closely Spaced Targets," in submission for *IET Radar, Sonar & Navigation*.

Conference papers

- K. Georgiev, A. Balleri, A. Stove, and M. Holderied, "Baseband version of the bat-inspired spectrogram correlation and transformation receiver," in *2016 IEEE Radar Conference*, Philadelphia, USA, May 2016.
- K. Georgiev, A. Balleri, A. Stove, and M. Holderied, "Bio-inspired Two Target Resolution at Radio Frequencies," in *2017 IEEE Radar Conference*, Seattle, USA, May 2017.

Book chapters

- K. Georgiev, A. Balleri, A. Stove, and M. W. Holderied, "Enhanced range resolution: comparison with the matched filter," in *Biologically-Inspired Radar and Sonar: Lessons from Nature*, A. Balleri, H. Griffiths, and C. Baker, Eds. Stevenage, UK: IET, 2017, ch. 3.
- A. Balleri, K. Georgiev, A. Stove, H. Griffiths, C. Baker and M. W. Holderied, "Biologically inspired processing of target echoes," in *Novel Radar Techniques and Applications*, Richard Klemm, Eds. Stevenage, UK: IET, 2017.

Chapter 2

Literature review

Modern radar and sonar rely on active sensing to accomplish a variety of tasks, including detection and classification of targets, accurate localization and tracking, autonomous navigation and collision avoidance. Research on these topics started with investigations looking at resolving individual scatterers within a single target in complex clutter environments and, in the course of the years, has advanced towards much more sophisticated challenges that relate to modern cognitive sensing capabilities [1, 2, 3].

Bats use echolocation to discover, select and capture their food often in dense clutter, to manoeuvre in complex environment and to find their way in the open space [4, 5, 6, 7]. Behavioral experiments have demonstrated they can deal successfully with many of the challenges faced by synthetic sensors. They exploit waveform, spatial and temporal adaptations in the process of target detection, resolution and recognition. At the same time, adaptive waveform diversity techniques [8], as well as cognitive guidance and control [8, 7] and memory [9, 7], are all characteristics that are studied in the context of cognitive synthetic sensing. Bats are biological realisation of the cognitive sensing concept.

In radar, multiple analogue and digital processing steps are performed before the higher level tasks of target detection, resolution, classification, position and speed measurement and tracking. For example, the return signal is collected and shaped by an antenna which acts as a spatial filter that passes energy coming from selected directions only. Then in the receiver the signal is amplified and downconverted by analogue devices to lower frequencies that can be digitised and processed by existing digital hardware. Next in the signal processor the energy is compressed through matched filtering and Doppler processing. This destroys undesired information and allows the desired signal to be separated. The output of the processor is often referred to as image (especially in the 2-D case of range–cross-range) or high range resolution profile (HRRP) in the 1-D case.

Matched filter is a linear filter designed to detect a particular waveform and provide maximum attainable by linear filter signal to noise ratio in case of single perfect match buried in additive white noise [10]. If the white noise is Gaussian the filter output is deterministically connected to the likelihood to have the target at different locations [11, 12]. For single target matched filtering combined with peak extraction provide an ideal detection and measurement. The measurement accuracy is defined as the standard deviation of the measurement. The theoretically-possible accuracy with which the time delay can be measured is, according to Woodward [11, p. 105] and Rihaczek [1, Sec. 3.1.]

$$\sigma_T = \frac{1}{\beta\sqrt{2E/N_0}} \tag{2.1}$$

where β is the r.m.s. bandwidth, E is signal energy, N_0 is the noise power spectrum, and $2E/N_0$ is the signal-to-noise ratio. Matched filtering, ranging and accuracy are discussed in more detail in Chapter 3.

In the general case, there is a multiple-target environment and a particular return must be detected in the sum of the system noise and interference from other targets [1]. If the targets are not sufficiently separated to prevent overlap of their returns the applicability of matched-filter concept discriminate the targets becomes questionable [1]. The concept of resolution is introduced and explained further in Chapter 3. For waveform with flat spectrum the time resolution δ_T is quantified as the reciprocal of the bandwidth.

The way bats process echoes from targets and the surrounding environment is considered different from that of modern radar and sonar systems. Different aspects of bat echolocation are studied in the literature, including range accuracy, range resolution, directional accuracy, obstacle avoidance mechanisms, neural coding, clutter suppression, etc. Bats have demonstrated performance that is hard to explain. This section is restricted to models that use only range information, a single receiver, and do not account for directional sensitivity [13, 14, 15]. In these models frequency modulated signals (emitted call and received echoes) are passed through a filter bank to generate auditory spectrograms (a model for the auditory periphery) which is followed by temporal processing (a model for delay tuned neurons in the brain) for ranging the targets and a spectral processing to resolve close target interferences.

The focus of this research is to understand the features of the bat-echolocation inspired processing that can differentiate it from the conventional signal compression in range. The following literature review questions can support the research objectives. What are the tasks that bats can perform using echolocation, what are their capabilities and limitations (Sec. 2.2)? How bat physiology can support this performance when the neural coding latency is of the order of milliseconds (Sec. 2.3)? What are the main applications in radar and sonar of the bats echolocation research results (Sec. 2.4)?

2.1 Bat echolocation basics

A good introduction to bats in general and echolocation is provided in [16]. The anatomical and neurophysiological basis of the echolocation in bats are presented in [17]. Both psychophysical experiments and the neurophysiology of bat echolocation are covered in [18]. A review on bat auditory system physiology as compared to other mammals is provided in [19, 20].

Bats emit echolocation sounds in pulses. These pulses could be constant frequency (CF), frequency modulated (FM) or mixed (CF/FM) as some species hunt insects in open air but others forage for fruit or flowers in the clutter of trees and vegetation. Echolocation is used in different phases of bat hunting and for different tasks - searching to detect a target, approach during which the target is identified and terminal chasing which requires precise localization of the target. The call waveform parameters like duration, bandwidth or even the harmonic structure are correspondingly changed [21]. The spectrogram of a field record of the sound of the big brown bat *Eptesicus fuscus* is shown in Fig. 2.1. All three stages are clearly separable.

This review will be limited to frequency modulating bats (FM bats) because they are able to discriminate stationary targets in dense interfering clutter. Doppler information is not available so the bat receiving chain will be specialized for range processing, the main field of interest for this research.

Broadband FM pulses are typically 2–5 ms long, often more than 10 ms during search and less than 0.2 mm in the terminal phase [16]. The waveform has fundamental frequency sweeping from about 60 to 30 kHz and can have one or more harmonics (Fig. 2.1, Fig. 2.2, Fig. 2.3). The pulse repetition frequency is about 10 Hz during search and more than 200 Hz at the final buzz (Fig. 2.1). The ultrasound beam width is approx. ±30° at 80 kHz and ±70° at 25 kHz (as summarized in [22]).

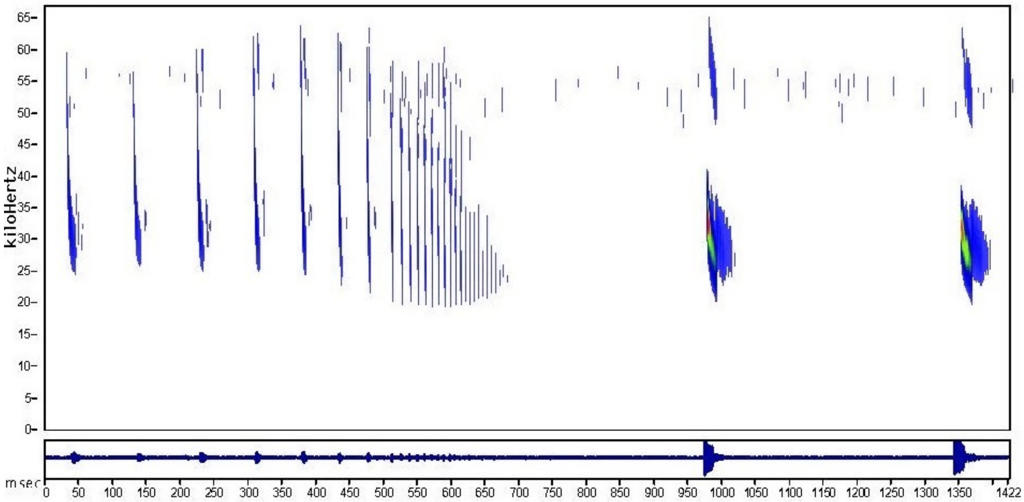

Figure 2.1: The big brown bat (*Eptesicus fuscus*). Approach call, feeding buzz, pause, followed by two echolocation calls. Recorded in Rio Blanco County, Colorado, August 2, 2013, Katy Warner, CWU, 2016-04-14, Image source: https://www.nps.gov/subjects/bats/echolocation.htm, Last accessed: July 18, 2017

2.2 FM bats echolocation performance and experiments

This review section will discuss the basic discriminatory capabilities and limitations of FM bats as observed in behavioural experiments. The big brown bat *Eptesicus fuscus* will be the default subject if something else is not explicitly stated. Most of the experiments reviewed use so called “phantom targets”. Phantom targets are produced by replacing the returns from a real target with a synthesized one generated by a speaker. The sound emitted by the bat is recorded, digitally processed to achieve appropriate delay and filtering and played back to the bat. This way the target exists only in the acoustic world – guaranteeing that the echolocation is the only sense used.

Assessment of bat’s performance in terms of range accuracy that bats can achieve is not a trivial task. Behavioural experiments are discrimination experiments by their nature and cannot give accurate numbers. It is not possible to perform a sequence of range measurements and calculate the variance. The accuracy is derived by exploring the bat’s

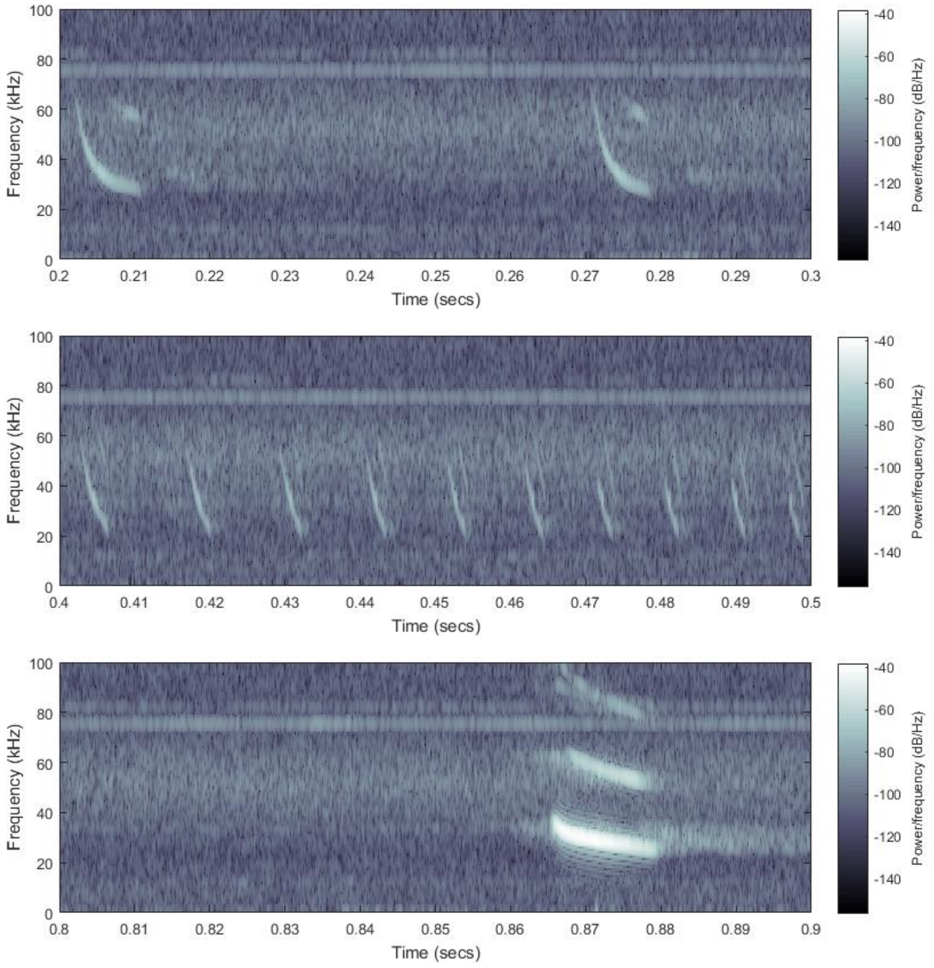

Figure 2.2: Approach call, feeding buzz and echolocation call spectrograms for the big brown bat (*Eptesicus fuscus*). These spectrograms were produced using 199 points Hanning window and 512 points FFT for signals sampled at 440 kHz. Source: sound record by Katy Warner, https://www.nps.gov/av/nri/avElement/nri-10xTEfeedingbuzzEPFU.mp3. Last accessed: July 18, 2017.

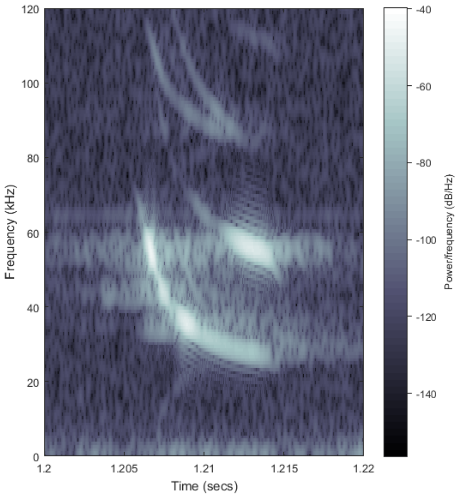

Figure 2.3: Big brown bat's (*Eptesicus fuscus*) multi-harmonic echolocation call. This spectrogram is produced using a sound record by Katy Warner available at https://www.nps.gov/av/nri/avElement/nri-10xTEEPFU.mp3. Accessed: July 18, 2017

capability to select the closest of two targets at different angular positions. The minimal difference in range at which the success rate is 75% is used as a measure of accuracy.

Simmons described experiments where four species of bats had to select the closer of two targets [23]. *Eptesicus fuscus* correctly identified the closer one in at least 75 % of the trials for range differences above 12–14 mm. This corresponds to echo arrival differences as small as 60 μs. The measured bandwidth of the chirp was less than 30 kHz (from 25 kHz to 50 kHz). The same experiments were repeated with phantom targets in order to remove potential cues for the bat as different echo intensity and spectral characteristics for different distances. In that case the recorded bat call was delayed and played back to the bat. The signal was high-passed at 25 kHz and low-passed at 75 kHz. Therefore the matched filter resolution is about 40 μs (assuming bandwidth of 25 kHz) and strictly above 20 μs (at the equipment limited bandwidth of 50 kHz). The accuracy based on multiple psychophysical experiments is between 30 and 90 μs as summarized in [24]. Distance discrimination trials have shown "accuracy" compatible with the matched filter compressed waveform width.

The above experiments are not suitable for sub-millimetre accuracy testing as they introduce additional error from movement of the bat. To overcome this limitation the so called target jittering experiments were designed [25]. The task of the bat was to discriminate in a sequence of echolocating calls between a phantom target with fixed delay and a phantom target that changes its delay (range) at each call thus switching between two possible values (Fig. 2.4). Multiple experiments were performed with jitter reduced from 100 μs to 0.4 μs [25, 26, 27]. The minimal jitter detected with 75% success rate was called acuity and also used as a measure of range accuracy. The threshold of jitter discrimination reported was 0.5 μs or less, a value consistent between all the studies. The false alarm rate was about 10 %.

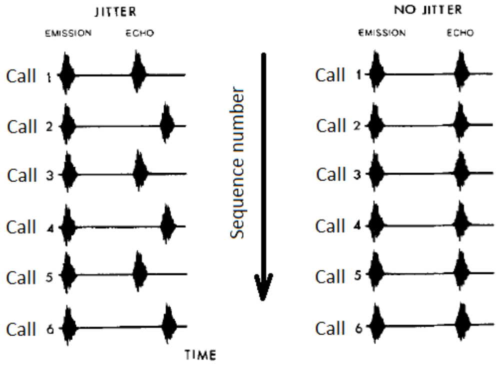

Figure 2.4: Jittering target [26]

Moss and Schnitzler repeated the experiment with filtering the harmonics (cutoff at 55 kHz) and even the higher frequencies of the fundamental waveform (cutoff at 40 kHz) [26]. Bat jitter discrimination was the same. In [28, 29], Simmons managed to go even further, showing that the big brown bat (*Eptesicus fuscus*) can perceive the arrival-time of virtual echoes with an acuity of 40 ns for signal-to-noise ratio of 36 dB and of 10–15 ns in quiet ambient laboratory conditions (49 dB).

The waveform emitted by the bats in the above experiments was a frequency modulated down chirp with fundamental frequency swapping from 55 kHz to 25 kHz [26], (55–23) kHz [25] and (50–25) kHz [27]. The sound consisted of two or three harmonics between 15–25 kHz and 100 kHz. The duration of the call was between 0.4 ms and 1.9 ms with mean values significantly different for different bats, between 0.91 ms and 1.54 ms [27]. Similar durations were reported by [25, 26]. Bats emitted about 20 calls per decision [25, 27] (several pulse trains of 5 to 20 or more echolocation calls for more complex cases [30]).

To evaluate the meaning of the experiment results, the theoretical possible accuracy σ_t was calculated using (2.1). The rms bandwidth β can be calculated from the spectrum of the signal (see Sec. 3.1.3) as the square root of the second moment of the PSD of the signal about a suitably chosen point. For a flat spectrum with a width B_C of 80 kHz the rms bandwidth is $\beta = 1.8B_C = 145$ kRad/s and the limiting accuracies for single measurement are shown in Tab. 2.1. For non-flat spectrum β will be lower and the uncertainty σ_t higher. For multiple measurements (i.e. multiple calls per decision), σ_t is reduced by the square root of the number of observations, i.e. 3 times for 9 observations and 4 times for 16 observations. Different bandwidths and measures for the theoretical limits were discussed in [28]. The term “semicoherent” processing was used when the envelope of the autocorrelation is used. This can create confusion as for radar signals processing a signal translated to baseband is still considered coherent processing. It is also not clear whether the rms bandwidth is properly calculated in terms of radian frequency. In any case the reported acuity looks comparable to the accuracy provided by an ideal receiver as bats make decision based on multiple calls.

Menne et. al. showed that bats are sensitive to phase jittering [27]. The group delay was fixed. Through a sequence of experiments with different combinations of delay and phase jitter it was also shown that bats perceive delay and phase jitter independently.

SNR, dB	Theoretical σ_t	Reported acuity [28]
5	4 μs	—
—	—	< 0.5 μs
36	110 ns	40 ns
49	24 ns	10 ns
55	12 ns	—

Table 2.1: Theoretically possible timing error expressed as standard deviation σ_t for 80 kHz linear chirp compared to the reported acuity in target jitter experiments [28]

Models of populations of neurons can also provide a mechanism to achieve hyperacuity in the temporal representation of the signal [31]. How a high constant sampling rate can be replaced by high latency neural spikes on a continuous time axis will be excluded from the scope of this study even though it can give important hints for the hardware implementation of the bat inspired algorithms.

These experiments arguably demonstrate a bat's ability to discriminate between ranges that differ by much less than the wavelength of the signal. The bats are able to preserve time accuracy by several orders of magnitudes better than the neural cell firing rates (millisecond time scale). While this could be an argument that bats are capable of exploiting the phase of the ultrasound signal, it does not show an ability to resolve the ambiguity in the absolute range estimation which arises if the phase of the carrier is used.

One of the very attractive features of bat echolocation is the ability of bats to resolve very closely located scatterers and various experiments have been carried out to assess and better understand this capability. In [28, 29], for example, Simmons showed that the big brown bat (*Eptesicus fuscus*) could discriminate a single-point target from a two-point target for spacings generating time delays above as little as 2 μs with chirp-like echolocation calls of 2-3 ms duration and a bandwidth of 85 kHz. For this type of echolocation call, the corresponding conventional (or nominal) range resolution of a radar or sonar system, defined as the half power width of a point target response [32], would be about 12 μs and hence six times worse than the resolution of the bat. Similarly, Schmidt showed that the greater false vampire bat (*Megaderma lyra*) could discriminate between two phantom target echoes separated by a time-delay of about 1 μs with 0.5 ms long waveforms and a bandwidth of up to 100 kHz [30]. The corresponding nominal resolution is 10 μs. Discrimination performance in the presence of surface structures was demonstrated in [33] where *Glossophaga soricina* were trained to distinguish a smooth surface from a coarse structure with a depth bigger than 0.38 mm. The emitted signal in these experiments was a frequency modulated down-chirp consisting of three harmonics spanning the bandwidths between 95–55 kHz, 150–86 kHz and 190–140 kHz. The predicted range resolution is 1.26 mm. There might be little difference in the various reportings but overall the literature presents a consistent story of the bat resolution ability being better than expected.

Eptesicus fuscus were trained to discriminate between two-component (complex) and one-component (simple) targets in [34]. The effect of the variation of the size of the simple target and corresponding neural latencies were used to make conclusions about the acoustic images in the bat's brain. The spectral information used to represent close targets is expressed in terms of absolute target range [34]. A good review of target resolution behaviour experiments is provided in [35]. Through a set of new experiments it was shown that big brown bats can separately perceive the delays of two-point biosonar echoes arriving as close together as 2 μs. This two-point resolution is "roughly five times smaller than the shortest periods in the bat's sounds" [35]. With the frequency response of the simulator loudspeakers ranging from 20 kHz to 85 kHz, the available spectral cues are also extremely limited.

It is interesting to provide more details on the target resolution experiment setups. One approach was to "probe" the internal time/range representation of the target perceived by the bat (e.g. see [35]). This was possible due to the observed bat confusion if the glint from a single scatterer overlapped with a glint from the two scatterer target representation. In phantom target experiment the task of the bat was to select the two-scatterers target instead of the one scatterer target. The one scatterer target location was varied and the resulted error rate profile was used as an indication of the target range representation. Another more straightforward approach was to discriminate a two scatterer phantom target with fixed spacing from other two scatterer phantom targets with variable spacing [30].

The perception of the target scatterer is changed if another scatterer becomes closer than 350 μs [36]. This value is provided as an estimate of the integration time of the bat's sonar receiver. Similar masking of a scatterer is described in [22] where the interference between two distant scatterers and a single point clutter was investigated. It was observed that a delay of less than 50 μs from the clutter to a scatterer of the target leads to an increase in the discrimination error.

The sensitivity of bats to disruption of the echo spectrograms was examined by Bates and Simmons [37]. By introducing different delays to the echo harmonics it was shown that misalignments as small as 2.6 μs can degrade echo delay discrimination significantly. This effect is described as "defocusing" of the bat's delay image. It was presented as a clutter suppression mechanism [38, 37, 22].

Other experiments involve stochastic targets. Natural objects like trees and bushes have thousands of reflective surfaces so discrimination based on discrete number of scatterers does not make sense. It was demonstrated that the bat *Phyllostomus discolor* spontaneously evaluate and generalize the roughness of chaotic impulse responses [39]. The surface roughness discrimination was quantified in [40, 41] (threshold 2.5 in units of base 10 logarithm of the stimulus fourth moment). Both psychophysical and neurophysiological data were provided.

Phase sensitivity of the bat's sonar was studied explicitly by manipulating only the phase response of the phantom target and keeping the magnitude response unchanged [42]. This procedure is equates to replacing the impulse representation of the scatterer with white noise of a specific duration. The 75 % discrimination threshold was at a white noise duration of approx. (206–372) μs. This strongly argues that the target is represented through the magnitude response. The phase is accounted only indirectly through a mechanism for delay encoding. An explanation of the controversial results compared to the phase jittering experiments was proposed [42]. It pointed out that the phase differences could be converted into spectral cues due to the non-linearities introduced through the auditory spectrogram.

The hypothesis that bats recognize places by remembering their echo signature rather than their 3D layout is proposed and examined [43]. This suggests that accurate absolute localization is not always critical and can be augmented by target shape or surface characteristics.

Above observations are used to understand the acoustic images that bats perceive and the key features of the way bats process signals. They answer the first literature review question (p. 11): what are the tasks that bats can perform using echolocation, what are their capabilities and limitations. To summarize, it seems like bats *Eptesicus fuscus* are able to discriminate small shifts in the range of a single target close to the statistical limit, to resolve two target spacing differences as small as 2 μs (less than one third of the Rayleigh limit) and to discriminate stochastic targets based on their roughness. Their signal processing chain most likely does not rely on phase information. The absolute ranging is not so accurate – about 60 μs. The perception of the target also changes if another target is closer than about 60 μs. The next section will review existing models that try to describe how bat's physiology can support above performance or are designed to reproduce similar features.

2.3 Monaural bat auditory system models

The above review shows that bats are able to achieve performance far better than would be expected when standard radar and sonar signal processing (e.g. matched filtering) is applied to bat-like waveform bandwidths. This motivates the study of the bat echolocation calls, the bat receiving chain and the cognitive adaptation. The scope of this review will be limited to the bat auditory system models needed for processing the range dimension [13, 14, 15]. The other aspects of target localization, resolution and discrimination, as well as the elevation and azimuth information treatment will not be discussed. The way bats process echoes from targets and the surrounding environment is considered different from that of modern radar and sonar systems.

The bat auditory system based models try to mimic or implement functionally the physiology of the mammalian auditory system. The auditory system is divided into peripheral and central auditory system.

- The peripheral auditory system includes the outer, the middle and the inner ear of the bat. It carries out the "analogue" part of the signal processing [44]. The spectral content of the echo is first modified based on the elevation and the azimuth of the target due to the pinnae (outer ear) shape. Then the wideband high frequency signal is transformed into multiple channels of low frequency signals through the inner ear or the cochlea. The process is modelled as a bank of filters that provide a time-frequency representation of the input signal (the so called auditory spectrogram) [13, 15, 45, 46]. The output signals are encoded as neural spikes appropriate for further processing. These spikes are electrical discharges that can be represented as discrete impulses with analogue delays and fixed "refactory period" (minimal delay between consecutive spikes).
- The central auditory system provides monaural and binaural pathways for decoding

and combining the information from the ears. It is modelled either functionally or as a neural network accounting for the different levels of central nervous system processing. It provides an estimate of the time delay between the call and the echo and additional cues about the structure of each echo, fine delays, elevation and azimuth.

An important model in this group is the Spectrogram Correlation And Transformation (SCAT) receiver (Saillant *et al.* [13]). It is a model of the auditory system that accounts for the underlying neural organisation in FM bats *Eptesicus fuscus*. It is divided into three blocks called the cochlear block, the temporal (spectrogram correlation) block and the spectral (spectrogram transformation) block. As mentioned above, in the cochlear block time-frequency representation of the signal is generated. In the temporal block the signal is compressed by introducing appropriate delays for different frequency channels and summed over frequencies to get a general delay profile for the whole range of sight. In the spectral block the signal is integrated over time around each target location to get closely spaced scatterers interference patterns. It should be noted that while the signal in the temporal block is encoded by neural spikes, the spectral block is purely functional and uses continuous magnitudes. Finally cosine inverse transform is performed to get fine resolution delay profile of the target. This process is interpreted as a voting mechanism.

SCAT receiver performance is further studied analytically in [47] and [48] where the outputs of the bandpass filters were approximated with cosines shaped by Gaussian envelopes. Peremans and Hallam [47] show the limitations of the temporal block and that the spectral block will generate spurious arrival times if more than two echoes are present. Park and Allen [48] further explore the spectral output of the spectral block. They provide an interpretation of the inverse transform of the interference patterns into a fine delay profile as a pattern-matching process. Spurious targets are attributed to the the fact that closely spaced targets are represented by the sum of the interference patterns of all possible pairs of overlapping echoes [48]. It is interesting to note that the idea that the target is perceived as a set of pairs of echoes is supported by an unrelated experiment [22]. In this experiment the bat should recognize a known target (two scatterers at a predefined distance) in the presence of clutter expressed as a single scatterer with varied position. The interference between the clutter and the target was studied. It was observed that a delay of less than 50 μs from the clutter to a scatterer of the target leads to an increase in the discrimination error. If the delay is higher the clutter does not mask the target even if it is positioned between the target scatterers.

The Sanderson et al (2003) model [49] was proposed to study the range accuracy achievable by bats for single target. This model corresponds to the temporal processing part of SCAT, i.e. the cochlear block and the temporal block. The waveform used was linear chirp with single harmonic between 90 kHz and 20 kHz. The filter bank contained 22 Chebyshev IIR filters with central frequencies linearly distributed but also adjusted to integer multiples of the 0.5 μs sample period. Several delay estimation approaches (including the one defined in SCAT) were applied and compared with the cross-correlation output and the theoretical limit (2.1) at different SNR. Through simulations at different SNR of the echo and different smoothing of the filter bank outputs it was shown that full phase sensitivity can be preserved. Using a second-order smoothing filter with a cut-off frequency of 8 kHz, the model achieved a delay acuity of 83 ns at an SNR of 36 dB and a delay acuity of 17 ns at 50 dB. Even though some adjustments in the model are made, the results can be considered as a demonstration of SCAT compliance with the range-jitter experiments. This model is not studied for resolution of closely spaced targets as the echo interference is not accounted for, i.e. there is no equivalent of the SCAT spectral block.

The Neretti et al (2003) model [50] was developed to examine the fine range resolution achieved by bats. It operates directly over the time-frequency output of the auditory periphery so it can be considered a modified version of the cochlear block of SCAT. The spacing between the scatterers is evaluated using a template matching procedure. With simulations it is demonstrated that two target resolution of 1.2 μs is achieved at SNR above 35 dB and 10-25 μs for SNR below 30 dB. While the bat two point scatterers resolution was confirmed, a drawback of such an approach is that the templates are prepared for specific call waveform and just two targets. Changing for example the call duration will require change of the templates. Even though theoretically achievable resolution was shown, its robustness for physical targets and measurements was not evaluated.

An autocorrelation model of the bat sonar is proposed by Wiegrebe (2008) in [15]. This model provides and evaluates a time-frequency representation of the signal. The output of the auditory periphery is compressed by channel-wise normalised autocorrelation. This step combines in a way several steps of the SCAT model – the dechirping from the temporal block, the fixed time integration in the spectral block and the power equalization involved in the inverse transform. The output is preserved in time-frequency format in a so called image buffer and is not converted into the time domain – another difference from the SCAT model. Acoustic information across a sequence of echolocation calls could be integrated in the same image buffer. The whole image buffer was used for solving different tasks. It was compared with templates in terms of the Euclidean distance and a threshold was used to make decision. Templates were prepared by averaging 20 presentations of the rewarded target response. Simulation results were compatible to the behavioural experiments for the following tasks to: (1) discriminate the roughness of complex virtual targets, (2) discriminate phase randomization of the echo, (3) discriminate echo delay differences, (4) discriminate two target spacing differences, and to (5) discriminate low passed from high passed signal (targets with a spectral pass-band around 41 kHz from such with a pass band around 82 kHz). This model was not able to reproduce the sub-microsecond acuity of the range-jitter experiments.

Recent works emphasize the “first-spike latency coding” and the “amplitude-latency tradeoff” [51, 52, 53, 54]. More realistic models were proposed for both the peripheral and the central auditory systems where the information in the auditory brainstem is coded as neural spikes [51, 52]. The problem was how the magnitude of the signal is represented in the neural system. It was studied based on neural measurements of Local Field Potentials (LFPs) and single-unit responses from the Inferior Colliculus (IC) [53]. The spike rate which is normally used is not enough due to the limited duration of the stimulus – only one or at most a few spikes can be generated to represent the target in any one channel as demonstrated by Sanderson and Simmons [53]. The first-spike latency was used as an alternative to the number of spikes for encoding the amplitude [51, 54]. The neural encoding of the time-frequency analogue output of the cochlea by population of auditory neurons was studied in [54]. These works employ models that are closer to the physiology of the mammalian auditory periphery than the SCAT. The Reijniers and Peremans model [54] is a version of the Meddis model [46] with some parameters adapted for the bats. Fontaine and Peremans rely on the Patterson [45], Fontaine et al (2011) on the Brian simulator [55]. The peripheral model used in Loncich [52] is EarLab [56]. However this increased complexity does not help in achieving deeper understanding of the basic principles of the bat echolocation. Moreover Reijniers and Peremans paper has shown that the cochleogram can be reconstructed from the neural code and that the resulting spectral notch pattern is available to the bat [54].

Some of the recent research concentrates on reproducing in fine detail the processing of the signal in the bat auditory system, starting from the outer ear of the auditory periphery and proceeding to “coding a neural network that includes known auditory pathways and neuron types” [52]. Head-related transfer functions were investigated for both monaural and binaural spectral features [57, 58]. In contrast, this research extracts the basic principles of bat auditory system processing that differentiates it from the conventional radar and sonar target signature representations. While the aim of the bat auditory system models is to reproduce the acoustic images as it is believed, from a variety of behavioural experiments, that the bats perceive them, there is no explanation on what exactly brings the improvement in range resolution so it could be exploited in a technological system.

The amplitude-latency trade-off (amplitude induced latency shift) is measured experimentally for the bat auditory system [34, 59]. Reduction in spectral frequency power is converted in temporal misalignment in the auditory image. Behavioural experiments have shown that bats are sensitive to delays de-synchronization between channels of the order of a few microseconds [37, 22, 38, 60, 61]. So the neural spikes generated from stimuli with different magnitudes could be separated and processed through different computational paths [62]. The temporal binding hypothesis and the harmonic structure of the echoes [37, 38, 61] was used to explain the clutter "defocusing" capabilities of the bats. Due to the lower width of the sonar beam at higher frequencies there is attenuation of the higher frequencies for returns from objects not centred in the sonar beam. The idea to exploit spike latencies as a mechanism to extract spectral cues for independent processing was proposed in the context of both target shape perception and clutter rejection. It was also used to update the original SCAT with a neural network implementation of the spectral block [63].

The review of the target ranging algorithms inspired by bats echolocation cannot be complete if some prominent but purely functional mathematical models with minor physiological correlation algorithms are not mentioned. Matsuo research replaces the conventional constant frequency filter bank with a bank of Gaussian chirplets [14, 64, 65, 66]. The carrier frequency is matched with bat emission sweep rates in order to achieve higher time compression. Therefore a kind of channel-wise cross-correlation is performed. Next an iterative procedure allows estimation of the location and reflectivity of multiple closely-spaced scatterers.

Another approach for resolving closely spaced targets from bat echolocation signals was to apply the theory of sparse reconstruction [67]. The scatterers impulse response deconvolution is expressed as a convex optimization problem and L1-minimization is applied. Fontaine and Peremans have shown that this method performs comparably to the coherent receiver, can handle white noise and complex targets with many closely spaced reflectors with different reflection strengths [67]. Implementation of this approach over the multi-channel output of the cochlear block is demonstrated in Hague et al [68]. However, it was also noted that the lack of sparsity of the reconstructed target image would introduce multiple impulses [67]. In real measurements it is not likely that the return from a single scatterer will be an exact replica of the transmitted waveform. The robustness of the method to real targets has not been demonstrated experimentally.

This section discussed the second literature review question (p. 11): how bat physiology can support observed performance. Above models of the bat auditory system differ in the level of details and biological plausibility. Different waveforms (bandwidth and shape), different models of the peripheral system (number of filters in the filter bank, filter type and bandwidth, non-linear magnitude compression) and different models of the central auditory system (functional or neural, local integration or correlation) are used. A common theme is that first both the emitted call and the received echo are passed through an auditory periphery to produce a time-frequency representation of the echo. Than all frequency channels are aligned to achieve the first level of signal compression. Finally the range and frequency information are processed separately or together to provide the final target representation or decision for a specific problem. The exact mechanism for neural implementation of the signal processing will not be subject of this study even though it can bring valuable insight for low energy, highly parallel computations architecture. As the main goal is to investigate the differences and similarities between the way bats and the radar cross-correlation receiver process echolocation signal, the original SCAT receiver

[13] will be studied. It is relatively simple yet biologically plausible, can be considered a functional model but provides a neural implementation at all stages. The temporal and spectral processing can be modelled separately, which is also an advantage when analytical models have to be done. More details about SCAT are provided in Chapter 3.

2.4 Bioinspired applications for radar and sonar

The most general bioinspired models apply standard signal processing and classification algorithms over signals simulating bat waveforms and echoes. For example, a fully connected neural network is trained to discriminate cube from tetrahedron in [69]. The target was ensonified with ultrasonic pulses synthesized to mimic the call of the bat *Eptesicus fuscus* during the approach phase (bandwidth 75 kHz, duration 1-3 ms, two harmonics). The classification performance was evaluated for different echo representations used as input to the network - the raw time domain digitized record of the echo, the compressed time domain echo after matched filtering (cross-correlation with the emitted call), the frequency domain representation (the power spectrum) and the time-frequency representation (the spectrogram). It was found that the best performance is achieved by using the spectrogram representation of the echo (above 90 % accuracy). Both time domain representations failed to train the network. The frequency domain representation provided successful classification of 70 % of the echoes. The performance is also evaluated just by using the lower or the upper harmonic after low or high-pass filtering of the echo. The performance didn't degrade in the case of time-frequency representation. For the frequency representation case using only the first harmonic provided the same 70 % accuracy, but when only the second harmonic was available the accuracy dropped to 55 %. Another example of successful target discrimination from bat-like echolocation signals is provided in [70] for plants. A machine learning algorithm based on Primary Component

Analysis (PCA) and Support Vector Machines (SVM) was applied over the spectrogram of the echo.

While such models provide general proof that bat echolocation waveform can be used for target recognition, they do not bring insight of the unique features of the bat auditory system. In addition the results in the above studies were neither related to the bat performance for similar tasks nor explored the limitations in target discrimination. Recent developments in machine learning and deep neural networks can be applied directly for such kind of analysis (e.g. WaveNet provides a deep neural network architecture for processing raw time-domain audio data [71]).

The bio-inspired sensing research was concentrated mostly on the signal design used by bats. How bats are exploiting waveform diversity and how this can be exploited in future radar and sonar systems for autonomous navigation was reviewed in [72].

Other research tried to extract the specific features of the targets that are important for their discrimination through echolocation by bats [5]. Echo acoustic signatures of bat pollinated flowers were studied in [73, 5]. Data was collected using a linear frequency-modulated downchirp spanning the frequencies between 50 and 250 kHz. The main features were extracted by applying PCA over either the matched filtered time domain or the frequency domain signal. Classification was performed using either k-NN classifier or a Naıve Bayes classifier. It was shown that the contribution of the scattering from the flower petals is a key feature to determine if the flower is suitable for pollination. The difference in the backscattered power is also a feature. The k-NN performance was sensitive to the appropriate choise of the neighbours to match the cross-correlation properties between different angular perspectives [5].

Work by radar and sonar engineers on target classification inspired by what is known about how bats perform this task has generally assumed that the receiver includes a matched filter, e.g. see [5, 8]. An exception is the research by Burton and Lai [74] on underwater target classification based on SCAT filter. It compared the classification performance of specified neural networks using features generated by matched filter and by a SCAT filter and showed that in some cases SCAT had better performance. An existing dataset provided by NSWC Costal Systems Station, Dahlgren Division was used with added simulated reverberation noise. Emitted waveform was linear chirp with bandwidth of 40 kHz and different starting frequencies (5, 20, 40, ..., 120) kHz. It is worth to note that the filter bank (central frequencies distribution) was not adjusted for the waveform and frequencies used and yet it provided compatible performance to the matched filter.

A Bio-Inspired Range Finding algorithm (BIRA) was proposed and evaluated for range resolution for simulated ultrasound system [75]. It combined some features of [47, 14] but didn't prove to be robust to noise, multiple targets or the low pass filter effect of the air. This is not a surprising result as the limited integration time of the spectral block was not modelled.

The final literature review question (p. 11) was "What are the main applications in radar and sonar of the bats echolocation research results". Most applications of bat-inspired signal processing can be found in the literature for robotics for detection and localization using ultrasound (e.g. [76, 77]). These are binaural methods for 3-D space localization that build on the idea of studying the spectral interferences. To the best of author's knowledge, the bat auditory system based signal processing has not been applied at radar (microwave) frequencies.

2.5 Summary

Behavioural experiments performed by biologists show that the echolocating signal as perceived by the bats can differ significantly from the output of the radar receiver for comparable waveforms. Low resolution range information is combined with local high resolution capabilities. A variety of models of the bat auditory system exist in the literature that differ in level of details and biological plausibility. Such models have not been applied at radar frequencies. The SCAT receiver was selected as a representative model for the bat auditory system signal processing. In the next Chapter it will be described in more details together with the related principles of conventional signal processing for radar.

Chapter 3

Background theory

In this chapter the basic principles needed for understanding radar signal processing were presented. Considering the interdisciplinary nature of the work making it accessible to a wider audience is an important but challenging part of the research communication. The SCAT model of bat auditory system was discussed in detail with special emphasis on the interpretation of the model's functionality.

3.1 Signal representation and characteristics

3.1.1 The time and the frequency domain

The Fourier transform defines equivalent representation of a broad class of continuous signals. Signals connected through Fourier transformation are called Fourier transform pairs.

$$Y(f) = \int_{-\infty}^{\infty} y(t)\mathrm{e}^{-j2\pi ft}\mathrm{d}t \qquad \rightleftharpoons \qquad y(t) = \int_{-\infty}^{\infty} Y(f)\mathrm{e}^{j2\pi ft}\mathrm{d}f \tag{3.1}$$

If the signal energy is concentrated in one domain it will be spread in the other domain. If the signal is strictly limited in one domain it is infinite in extent in the other [78].

The ultimately narrow signal is the impulse. Its Fourier transform pair is a complex exponential with zero frequency, a signal with infinite duration and constant amplitude (Fig. 3.1). Shifting the position of the impulse will change the frequency of the complex exponential. Two time shifted impulses are transformed into a real cosine (Fig. 3.1). The closer the impulses are in the time domain, the lower the frequency of the cosine. It can be observed that the signal can be more readable in one of the domains. In the example above, while on the time axis the signal is represented by only two points, on the frequency axis there is an infinitely repeating sinusoidal pattern.

The impulses and the complex or real sinusoids are the building blocks of the signals. The complex representation is preferred as it allows the symmetry of the transformation to be preserved.

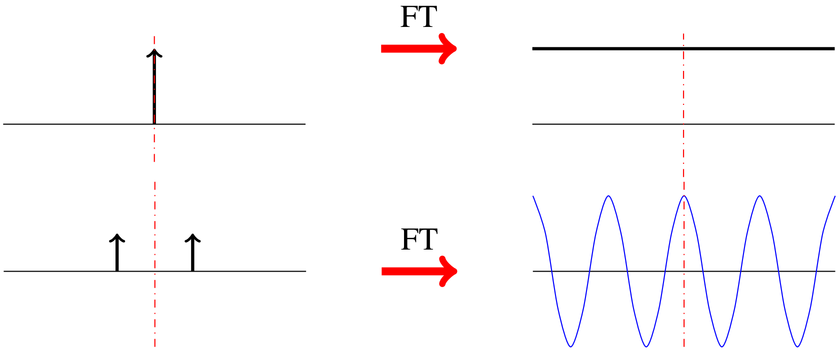

Figure 3.1: Fourier transform of single impulse and a pair of delayed impulses. The signal can be represented as a sum of complex or real sinusoids

Band limited impulse An impulse in a continuous signal (Dirac delta, $\delta(t)$) can be sampled as a discrete time impulse sequence (Kronecker delta, $\delta[n]$) under the following conditions (Fig. 3.2):

1. first filter $\delta(t)$ with ideal low-pass filter with cut of frequency equal to half the

sampling frequency F_s

$$\delta_{LP}(t) = \delta(t) * \mathrm{sinc}(F_s t)$$

2. sample exactly at times n/F_s

$$\delta[n] = \delta_{LP}(n/F_s)$$

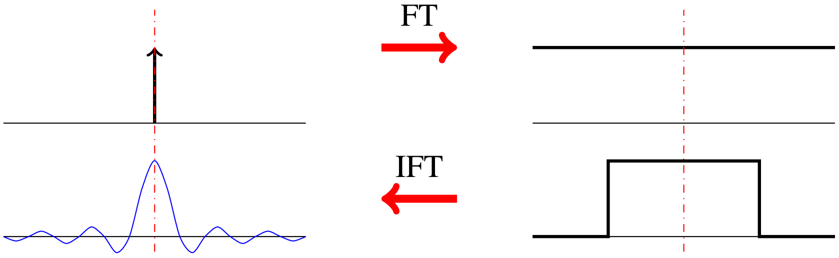

Figure 3.2: Relationship between Dirac delta and Kronecker delta

Time shifted impulse cannot generally be represented as a single discrete impulse. Either the zero location or the sampling frequency need to be adjusted. If there is a group of two time shifted impulses no shifting of the whole group can make them discrete. This can be achieved only if they are separated by a whole number of sampling intervals.

Discrete time sequence Band limited signals can be sampled without loss of information (sampling theorem). This allows the signal to be represented as a sequence of numbers. Let $y(n)$ denote a discrete time data sequence obtained by sampling a continuous-time signal. The frequency domain representation of a discrete signal is obtained through the Discrete Time Fourier Transform (DTFT). It is a continuous periodic function in which the original spectrum is repeated with a period equal to the sampling frequency.

$$Y(f) = \sum_{n=-\infty}^{\infty} y(n)\mathrm{e}^{-j2\pi fn} \qquad \rightleftharpoons \qquad y(n) = \int_{-0.5}^{0.5} Y(f)\mathrm{e}^{j2\pi fn}\mathrm{d}f \tag{3.2}$$

where the frequency f is in cycles per sampling interval, i.e. the analogue frequency in Hz f_{Hz} is normalised by the sampling frequency F_s, $f = f_{\mathrm{Hz}}/F_s$.

The equations (3.2) can be expressed as a function of the time and frequency:

$$Y(f_{\mathrm{Hz}}) = \sum_{n=-\infty}^{\infty} y(n)\mathrm{e}^{-j2\pi f_{\mathrm{Hz}} t} \qquad \rightleftharpoons \qquad y(t) = \frac{1}{F_s}\int_{-F_s/2}^{F_s/2} Y(f_{\mathrm{Hz}})\mathrm{e}^{j2\pi f_{\mathrm{Hz}} t}\mathrm{d}f_{\mathrm{Hz}} \tag{3.3}$$

Discrete Fourier Transform (DFT) DFT is used for transforming either discrete signal of finite length or periodic discrete signals.

$$Y(k) = \sum_{n=0}^{N-1} y(n)\mathrm{e}^{-j2\pi kn/N} \qquad \rightleftharpoons \qquad y(n) = \frac{1}{N}\sum_{k=0}^{N-1} Y(k)\mathrm{e}^{j2\pi kn/N} \tag{3.4}$$

Switching from indexes n and k to physical units t and f is trivial:

$$\begin{aligned} t &= n\Delta_T = n\frac{1}{F_s} \\ f_{\mathrm{Hz}} &= \frac{k}{N\Delta_T} = k\Delta_F \end{aligned} \tag{3.5}$$

DFT is usually implemented as a Fast Fourier Transform (FFT). In this study the terms DFT and FFT will be used interchangeably.

The conventional scaling of the time/range axis is either in physical units (seconds or metres) or in units of sampling intervals, Δ_T or Δ_R. The conventional indexing of the frequency axis is expressed in units of sampling intervals Δ_F, cycles per sampling interval, radians per sampling interval (natural frequency in radians), cycles per second (analogue frequency in Hz) or radians per second. To remove the confusion related to proper axis scaling, a simple algorithm is provided in App. B.4 to generate the required axis based on the number of points in the sequence and the required scaling parameters. Due to the inherent periodicity of the transformation, either positive indices $n = 0 : N-1$ or circular indexing $n = [0 : N/2, -N/2 : -1]$ can be used.

Autocorrelation and autocovariance The autocorrelation $r(k)$ of a deterministic discrete signal $y(n)$ is defined as

$$r(k) = \sum_{n=-\infty}^{\infty} y(n)y^*(n-k) \tag{3.6}$$

If the mean of the signal is first removed then (3.6) provides the autocovariance of the signal. For random signals of infinite duration and energy the autocovariance is the expected value of the product $y(t)y^*(t-k)$ of any two values at lag k:

$$r(k) = E\{y(n)y^*(n-k)\} \tag{3.7}$$

$$\hat{r}(k) = \frac{1}{N}\sum_{n=k+1}^{N} y(n)y^*(n-k), \qquad 0 \le k \le N-1 \tag{3.8}$$

where $\hat{r}(k)$ is an estimate of the covariance $r(k)$.

Power spectral density The energy spectral density of a deterministic energy signal is calculated directly from its Fourier transformation by squaring.

$$E_Y(k) = |Y(k)|^2 \tag{3.9}$$

An analogue procedure can be applied to a section of a power signal of length N:

$$P_Y(k) = \frac{1}{N}|Y(k)|^2 \tag{3.10}$$

The power spectral density (PSD) is defined more rigorously for random signals where it represents the distribution of the average signal power over frequencies [79]:

$$\begin{aligned} P_Y(f) &= \sum_{n=-\infty}^{\infty} r(k)\mathrm{e}^{-j2\pi fk} \\ P_Y(f) &= \lim_{N\to\infty} E\left\{\frac{1}{N}\left|\sum_{n=1}^{N} y(n)\mathrm{e}^{-j2\pi fn}\right|^2\right\} \end{aligned} \tag{3.11}$$

A variety of spectral estimation methods have been developed which transform a finite sequence on N samples of a stationary random process into a discrete or continuous function of frequency. Equation (3.10) provides an estimate of the PSD called a periodogram. It has a reasonable bias which goes to zero as the number of samples N go to infinity but the variance is poor and does not decrease when $N \to \infty$. The standard deviation is equal to the corresponding true PSD value [79]. Modified periodograms are introduced to reduce the variance at the expense of a small increase in the bias. The periodogram is smoothed by locally weighting and averaging. Some techniques apply windowing in the time domain with averaging the subsample periodograms (Bartlett 1948, Welch 1967), others apply windowing over the autocorrelation function (Blackman-Tukey 1959) and others directly average the power spectrum over small intervals B (Daniell 1946), e.g.

$$\hat{P}_D(f) = \frac{1}{B}\int_{f-B/2}^{f+B/2} \hat{P}_Y(g)\mathrm{d}g \tag{3.12}$$

There are also "parametric" methods that can provide an ability to resolve spectral lines in frequency by less than $1/N$ cycles.

3.1.2 Signal and noise power metrics

The energy E of the signal is the area under the signal squared curve. It can be calculated in either the time $s(t)$ or the frequency domain $S(f)$, assuming that the integral converge (e.g. when the signal has a finite duration).

$$E = \int_{-\infty}^{\infty} |s(t)|^2 \, \mathrm{d}t = \int_{-\infty}^{\infty} |S(f)|^2 \, \mathrm{d}f \tag{3.13}$$

Signals with infinite spread in time (periodic deterministic or stationary random) are characterised by the signal power P_S, which is the energy per unit of time.

$$P_S = \lim_{T \to \infty} \frac{1}{2T} \int_{-T}^{T} |s(t)|^2 \, \mathrm{d}t \tag{3.14}$$

A white noise is a random signal with constant power spectral density $N_0/2$. In practice the noise is band-limited and therefore has finite average power $N = WN_0$, where $2W$ is the bandwidth of the noise. Equation (3.14) shows that N is also the variance of the noise waveform.

Signal-to-noise ratio (SNR) is the ratio of the instantaneous signal power $P(t) = |s(t)|^2$ at its maximum and the average noise power N (mean squared noise). An alternative definition is common for radar as the signal is compressed in the receiver. The SNR is the signal energy E over the two sided power spectral density of the noise $N_0/2$.

$$\eta = \frac{P}{N} \tag{3.15}$$

$$\rho = \frac{E}{N_0/2} \tag{3.16}$$

3.1.3 Bandwidth

The bandwidth of a signal provides a measure of “the extent of significant spectral content of the signal” [78, pp. 29–31]. For real signals it is measured for the positive frequencies. Different definitions of the bandwidth are available based on how the “significant” frequencies are determined. If the signal is strictly band limited than the bandwidth is just the difference between the highest and the lowest frequencies. Otherwise, the definition of bandwidth accounts for the distribution of the spectral energy. Of practical importance for radar are the 3-dB bandwidth B_{3dB} and the root mean square (rms) bandwidth β (also called effective bandwidth).

The rms bandwidth is defined as the square root of the second moment of the PSD of the signal about a suitably chosen point and expressed in radians per unit time

$$\beta^2 = (2\pi)^2 \cdot \frac{\int_{-\infty}^{\infty} f^2 |S(f)|^2 \mathrm{d}f}{\int_{-\infty}^{\infty} |S(f)|^2 \mathrm{d}f} \tag{3.17}$$

Special attention should be paid not only to the definition but also to the dimension of the bandwidth. As with any frequency it can be expressed in Hz, rad/s, cycles per sampling interval, or radians per sampling interval. In addition, neither B_{3dB} nor β are appropriate for sampling rates as there is a significant spectral energy beyond them.

For rectangular shapes the rms value is $1/(2\sqrt{3})$. Therefore for a spectrum with a width B Hz,

$$\beta = \frac{2\pi B}{2\sqrt{3}} = 1.8B \tag{3.18}$$

3.1.4 Pulse duration

The duration of a rectangular pulse in the time domain is trivial to define. After the ideal pulse convolves with the environment and is further filtered by the receiver its shape smears and metrics similar to the ones used for bandwidth measurement are more appropriate. A 3 dB pulse duration and a the root mean square width T_{rms} can be used.

$$T_{rms}^2 = \frac{\int_{-\infty}^{\infty} t^2 |s(t)|^2 \mathrm{d}t}{\int_{-\infty}^{\infty} |s(t)|^2 \mathrm{d}t} \tag{3.19}$$

3.2 Downconversion to intermediate frequency and complex baseband representation

Both radar and bats need to encode the received signals at a much lower rate then the Nyquist sampling rate. Radar systems operate in the microwave band and use carrier frequencies of the order of a few GHz and typical bandwidths of a few MHz. Analogue to Digital converters (ADC) historically have been limited to much lower rates. And even modern ADCs are limited to the S-band sampling [80]. Bats echo-locate using ultrasound frequencies from tens to more than a hundred kHz, but neurons can produce spikes at intervals from a few hundreds of microseconds to several milliseconds (0.5–4 kHz).

The solution is found in the frequency domain representation of the signals. Radars rely on the so called *downconversion* to shift the signal to a lower carrier frequency known as intermediate frequency (IF) without changing the modulation bandwidth [3]. Bats use filter banks to sample the signal directly in the frequency domain at a relatively slow time rate. The bats approach will be summarized in Sec. 3.6.

Downconversion to IF is performed in an analogue device called a mixer (Fig. 3.3). The RF signal is multiplied with a reference signal $\cos(2\pi f_{\mathrm{LO}} t)$ called a local oscillator (LO). Multiplication in the time domain corresponds to convolution in the frequency domain. This way the signal spectra is translated to the line spectra of the LO. The unwanted frequencies are removed through analogue bandpass filtering. The resultant IF signal is real valued with carrier frequency $f_{\mathrm{IF}} = f_{\mathrm{RF}} - f_{\mathrm{LO}}$.

The IF signal is further converted to baseband. The positive band of the spectrum is centred at zero frequency. In order to prevent aliasing the negative part of the spectrum is discarded. The signal become complex and represents the so called complex envelope. The ”quadrature“ downconversion to I and Q components is performed in an analogue

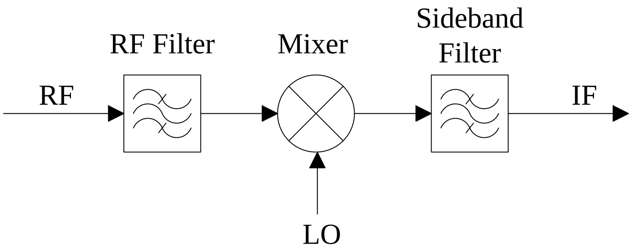

Figure 3.3: RF mixer

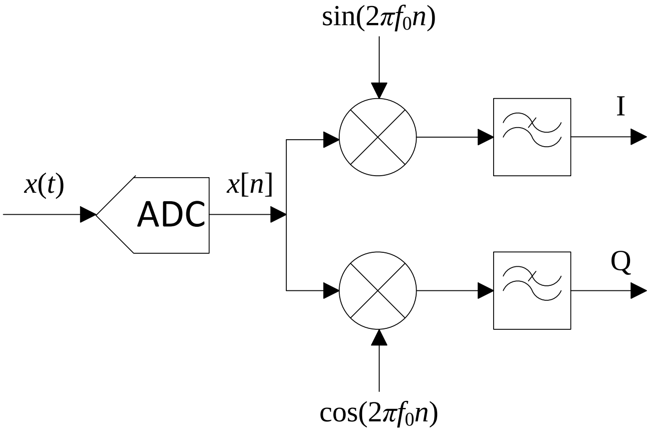

Figure 3.4: I/Q demodulation

device or entirely digitally. The device is called an I/Q demodulator, quadrature detector, synchronous detector, or coherent detector. An example of a digital downconversion architecture is shown in Fig. 3.4. The output signal is $u[n] = I[n] + jQ[n]$. It can be further downsampled. An alternative implementation is with a Hilbert transformation followed by frequency shifting.

3.3 Frequency modulated waveforms

A broad class of band-pass signals can be written as

$$\begin{aligned} x(t) &= a(t)\cos[2\pi f_0 t + \varphi(t)] \\ &= \Re\{a(t)\exp[j(2\pi f_0 t + \varphi(t))]\} \\ &= \Re\{a(t)\exp[j\varphi(t)]\exp[j2\pi f_0 t]\} \\ &= \Re\{u(t)\exp[j2\pi f_0 t]\} \end{aligned} \tag{3.20}$$

where $a(t)$ is the natural envelope function, $\varphi(t)$ is the instantaneous phase and $u(t)$ is the complex envelope [12, 10]. If $a(t)$ is constant the signal is frequency-only modulated. If the phase $\varphi(t)$ is constant the signal is amplitude-only modulated.

3.3.1 Linear chirp

A linear chirp $x(t)$ is a signal with linearly changing instantaneous frequency $f_{inst}(t)$:

$$f_{inst} = \gamma t, \qquad \gamma = \frac{f_{inst}(t_2) - f_{inst}(t_1)}{t_2 - t_1} \tag{3.21}$$

where γ is the frequency sweep rate. A complex chirp unrestricted in time will be:

$$\begin{aligned} u(t) &= \exp j\varphi(t) \\ &= \exp\left(j\int_0^t 2\pi f_{inst}\mathrm{d}t\right) \\ &= \exp\left(j\pi\gamma t^2\right) \end{aligned} \tag{3.22}$$

In practice the chirp has to be limited in time duration T and in frequency bandwidth B_C. The chirp rate is $\gamma = \pm\frac{B}{T}$. If the chirp is defined in the time domain then its magnitude is constant over an interval $(-T/2, T/2]$ and zero outside the interval. Additional delay

$T/2$ is needed to make the signal physically possible.

$$u(t) = \mathrm{rect}\left(\frac{t - T/2}{T}\right)\exp(j\pi\gamma t^2) \tag{3.23}$$

The corresponding real chirp is

$$\begin{aligned} x(t) &= \Re\{u(t)\exp(j2\pi f_0 t)\} \\ &= \Re\left\{\mathrm{rect}\left(\frac{t - T/2}{T}\right)\exp(j\pi\gamma t^2)\exp(j2\pi f_0 t)\right\} \\ &= \mathrm{rect}\left(\frac{t - T/2}{T}\right)\cos\left(2\pi f_0 t + \pi\gamma t^2\right) \end{aligned} \tag{3.24}$$

If the chirp is defined in the frequency domain then its frequency magnitude is constant over an interval $(-B/2, B/2] + f_0$ and zero outside. The phase is manipulated to become a non-linear function of the frequency. In the time domain this results in a chirp-like waveform of limited duration:

$$\begin{aligned} V(f) &= \mathrm{rect}\left(\frac{f - f_0}{B_C}\right)\exp[-j\theta(f - f_0)] \\ &= \mathrm{rect}\left(\frac{f - f_0}{B_C}\right)\exp\left(-j\pi\frac{1}{\gamma}(f - f_0)^2\right) \\ v(t) &= \mathcal{F}^{-1}(V(f)) \end{aligned} \tag{3.25}$$

3.3.2 Hyperbolic chirp

The hyperbolic chirp is characterized by linear instantaneous period change. It can be shown that the corresponding instantaneous frequency $f_{inst}(t)$ is:

$$f_{inst} = \frac{ak}{kt - 1} \tag{3.26}$$

where $k = \frac{f_2 - f_1}{f_2 T}$, $a = -\frac{f_1}{k}$, and $f_1 = f_{inst}(0)$ and $f_2 = f_{inst}(T)$ are the initial and the final instantaneous frequencies of the chirp and T is the time duration. The bandwidth is $B = f_1 - f_2$.

The final equation for hyperbolic frequency modulated signal is

$$\begin{aligned} x(t) &= \Re\left\{\operatorname{rect}\left(\frac{t - T/2}{T}\right)\exp(j2\pi a \ln(1 - kt))\right\} \\ &= \operatorname{rect}\left(\frac{t - T/2}{T}\right)\cos\left(2\pi a \ln(1 - kt)\right) \end{aligned} \tag{3.27}$$

The time waveform, the frequency spectral power and the time-frequency spectrogram are shown in Fig. 3.5 for linear and hyperbolic chirps spanning form 30 kHz to 5 kHz for 4 ms. It is interesting to note that the spectrum of the hyperbolic chirp is not flat.

3.3.3 Step frequency

A stepped frequency train of unmodulated pulses is a sequence of narrow bandwidth pulses at different carrier frequencies [10, 81]. If the number of pulses is N and the frequency step is Δ_F, a very short pulse with bandwidth $B = N\Delta_F$ can be synthesized. If all pulses have the same amplitude the synthesized waveform approximates a band-limited impulse [10, Sec. 9.9.2]. If the amplitudes are appropriately weighted the approximation is of a rectangular pulse [82, pp. 113-123].

The return of each pulse is characterised by its magnitude and phase. The returns of all pulses provides a sequence of frequency domain samples. The time domain data is synthesized by inverse Fourier transform of the frequency domain data. As the measurements are discrete, a range ambiguities are introduced with period $\frac{c}{2\Delta_F}$.

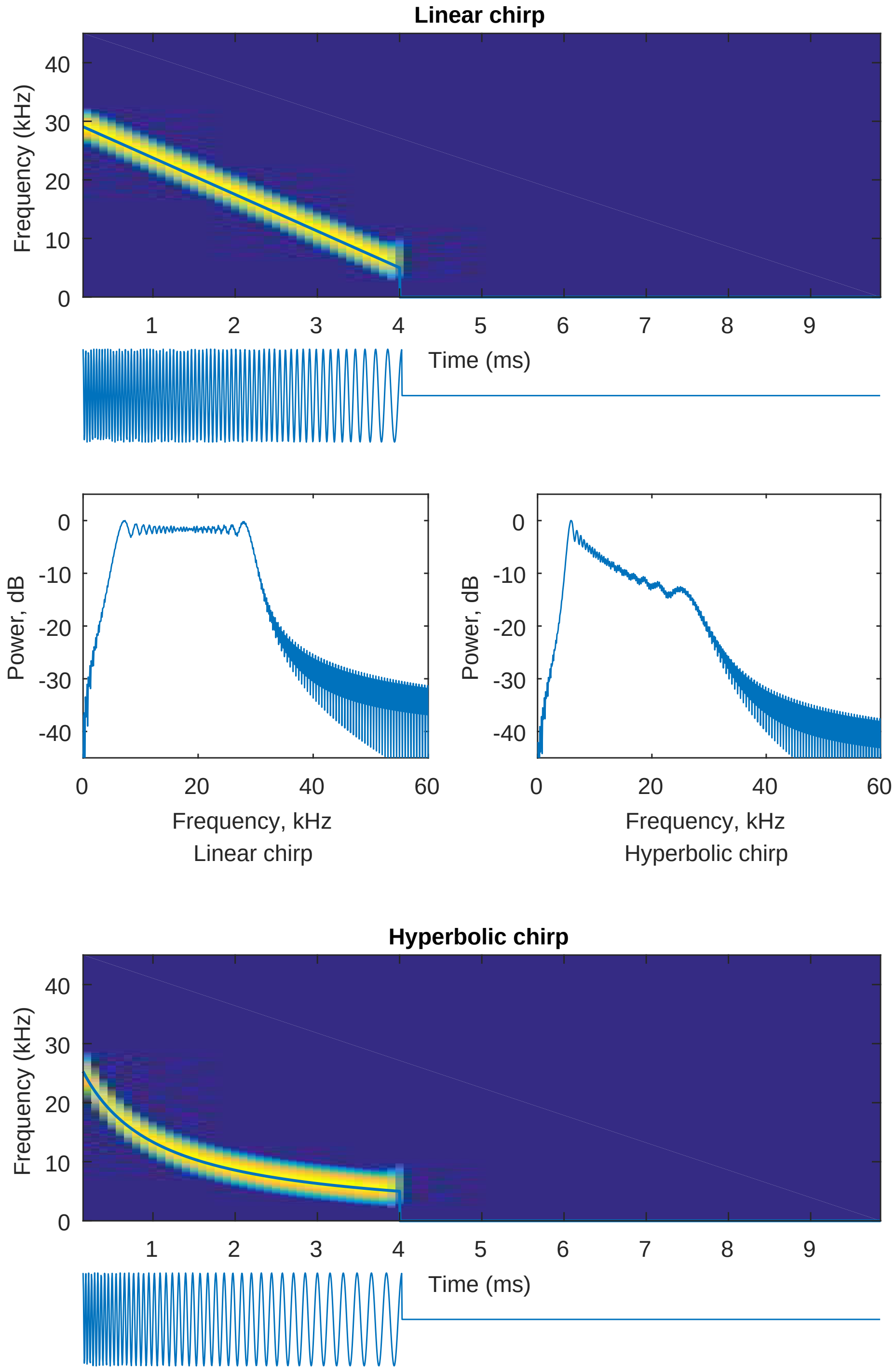

Figure 3.5: Linear and hyperbolic chirp representations. Waveform, spectrogram and spectrum. The instantaneous frequency is overlaid on the spectrogram

3.4 Pulse compression and matched filter

The objective of the pulse compression is to reduce the width of the receiver output pulse and ideally provide the impulse response of the targets. Any nonlinear phase function $\varphi(t)$ “must always” increase the rms bandwidth β [1, pp. 51–56]. The same applies for the rms duration T_{rms}: having a nonlinear phase $\theta(f)$ in the frequency domain will increase the signal duration.

$$\beta^2 = \int_{-\infty}^{\infty} |u(t)|'^2 \, \mathrm{d}t + \int_{-\infty}^{\infty} [\varphi'(t)]^2 |u(t)|^2 \, \mathrm{d}t \tag{3.28}$$

$$(2\pi T_{rms})^2 = \int_{-\infty}^{\infty} |V(f)|'^2 \, \mathrm{d}f + \int_{-\infty}^{\infty} [\theta'(f)]^2 |V(f)|^2 \, \mathrm{d}f \tag{3.29}$$

The receiver needs to perform a reverse operation, i.e. to demodulate the phase. The time-bandwidth (TB) product has a lower limit [1, 83]. It depends on the definitions for signal duration and bandwidth but is of the order of one. An optimal waveform will have big TB. An optimal receiver will output a signal with the minimal TB of about one thus providing a compression ratio of about the time-bandwidth product.

The complex envelope modulation can also be considered. Appropriately weighting the frequency spectrum will reduce the effective duration by changing the distribution of the energy around the mainlobe. Unfortunately it will also reduce the effective bandwidth and the compression ratio as a whole if the frequency band is limited. The optimal waveform will depend on the definition of pulse duration. For example using the rms spread of the signal will account for the sidelobes and using the half-power width will consider only the main lobe width.

3.4.1 Matched filter

Arguably the most popular algorithm for signal compression is the matched filter, also called the correlation processor. It was developed as a linear solution for the problem of detecting a known signal in white Gaussian noise. The optimisation criterion was maximization of the SNR at the receiver output [84, 85].

The matched filter impulse response $h(t)$ and the corresponding frequency response $H(f)$ are determined by the signal $s(t)$ or $S(f)$ to which the filter is matched [10].

$$\begin{aligned} h(t) &= Ks^*(t_0 - t) \\ H(f) &= KS^*(f)\exp(-j2\pi f t_0) \end{aligned} \tag{3.30}$$

The impulse response is a time-reverse of the signal conjugate. It can be scaled by an arbitrary constant K. A delay t_0 is introduced to make the filter causal ($h(t) = 0$ for $t < 0$ or $t_0 \geq T$). The frequency response is the complex conjugate of the spectra of the transmitted signal. Therefore the phase of the received waveform is compensated based on the transmitted signal phase. This is consistent with the interpretation of the signal compression as a phase demodulation technique. The spectral magnitude is weighted by the transmitted waveform magnitude and in this way emphasizes the expected frequencies and suppresses the other, as can be expected from a filter optimised for SNR.

The output of the matched filter $s_o(t)$ is shaped as the autocorrelation function of the signal (Fig. 3.6), e.g. for $K = 1$ and $t_0 = 0$

$$s_o(t) = s(t) * h(t) = \int_{-\infty}^{\infty} s(\tau)s^*(\tau - t)\mathrm{d}\tau \tag{3.31}$$

It has a peak proportional to the energy E of the signal

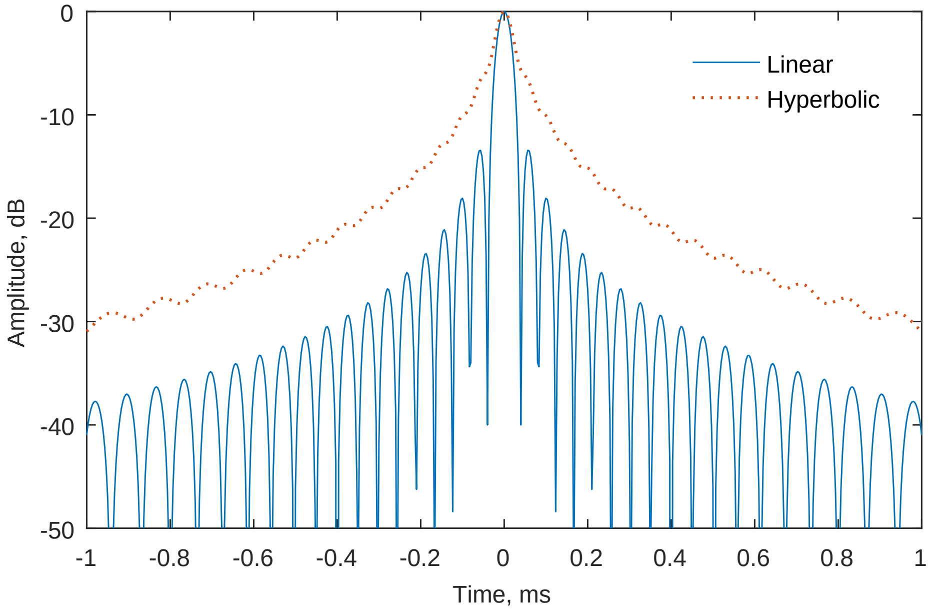

Figure 3.6: The autocorrelation output for the linear and hyperbolic chirp described in Fig. 3.5. Wideband signal, 30 kHz to 5 kHz

$$s_o(t_0) = KE \tag{3.32}$$

The SNR at the peak in the case of white noise is

$$\mathrm{SNR}_{\mathrm{MF}} = \frac{E}{N_0/2} \tag{3.33}$$

where $N_0/2$ is the two sided power spectral density.

Woodward gave probabilistic and "informational" derivation of the correlation receiver [86, 11] as a "sufficient receiver". A sufficient receiver was defined to have an output equivalent to the probability distribution $p_y(x)$, which contains all available information about the target parameter x that can be extracted from the radar return y. All extraneous information is destroyed. The shape of the sufficient receiver output and the probability $p_y(x)$ are not necessarily the same as far as they are related deterministically.

Matched filter output is used to support likelihood based statistical decisions [12]. A detection threshold and probability of detection are calculated assuming white Gaussian noise and preselected constant false alarm rate. Different noise distribution can be used but the results are not necessarily of practical significance.

Matched filter output $q(t)$ is used for measurement of target delay (parameter estimation tasks) from the received waveform $y(t)$. In the case of single point target $x_T(t) = \delta(t-t_1)$ and white Gaussian noise, the MF peak position gives the "best" target delay t_1 and is equivalent to the maximum likelihood estimate [86, 12] for large SNR.

$$\begin{aligned} y(t) &= s(t) * x_T(t) + w(t) \\ &= s(t) * \delta(t-t_1) + w(t) \\ &= s(t-t_1) + w(t) \\ q(t) &= y(t) * h(t) \\ t_1 &= \arg\max_t q(t) \end{aligned} \tag{3.34}$$

For the problem of single target delay estimation, the relationship between ideal and sufficient receiver is given in [86, pp. 81–85]

$$p_y(\tau) = kp(\tau)p_\tau(y) = kp(\tau)\exp\left(-\frac{E}{N_0}\right)\exp\left(-\frac{2}{N_0}q(\tau)\right) \tag{3.35}$$

The prior knowledge is given by the prior probability $p(\tau)$. The value of τ where the likelihood function $p_\tau(y)$ has a maximum is the maximum likelihood estimate for τ.

Matched filter can be applied in more complex scenarios:

- when the noise is white but not Gaussian, MF still maximise the SNR and the peak gives "best" parameter in least-squares sense;
- when the noise is white Gaussian, MF gives the best SNR among all nonlinear

filters that are time invariant [1, p. 30];

- when the noise is Gaussian but not white, a whitening filter can be applied and then a modified matched filter.
- in a multiple-target environment, if the scatterers are randomly located, independent and so dense that they are unresolvable – the problem becomes signal detection in coloured, Gaussian noise [1];
- in a multiple-target environment, when the targets are sufficiently separated to prevent overlap;

The applicability of matched-filter concept becomes questionable when

- the targets are not sufficiently separated to prevent overlap of their returns;
- when there are large nearby targets that can mask the small targets with their sidelobes.

3.4.2 Other filters

Inverse filter Inverse filter is a filter that shapes a finite sequence into a unit pulse. It is used to remove undesired components in a time series [87, pp. 75-77].

$$H(z) = \frac{1}{G(z)} \tag{3.36}$$

Equation (3.36) shows that the same frequency demodulation as in MF is performed. The magnitude is also demodulated by setting the filter magnitude response as the reciprocal of the signal magnitude response. Therefore the frequencies with low magnitudes will be boosted. Unfortunately the noise components are also boosted and such filters are appropriate for signals with very high SNR. Even though trivial, it is worth pointing out that frequencies not present in the transmitted waveform should not be processed as only noise and no useful information can be expected. An approach that combines linearly matched filter and inverse filter is proposed in [88, 89] and can be useful for compressing waveforms with non-flat frequency response like the hyperbolic chirp.

Least squares processing The problem with the practical implementation of the inverse filter is that its non-recursive form is of infinite length. Just trimming the theoretical sequence to a finite number of taps is not necessarily the best approach. A better approximation is to minimise the error energy between the output of the filter and the ideal unit impulse (for a given length of the filter). This leads to the least squares methods.

Adaptive pulse compression Pulse compression that adapts to the received signal is proposed by Blunt in [90]. It was designed to handle the case of multiple targets with significant differences in size.

Minimum phase filter The minimum phase filter has the minimum group delay for all causal and stable filters that have the same magnitude response. The energy spread beyond the start is minimal. Such filtering can provide advantages when having minimal group delay is more critical than the compression ratio.

A system is minimum phase if the system and its inverse are causal and stable. This means for a discrete time system that all zeroes and poles are inside the unit circle. For such a system the phase and the logarithm of the magnitude response are connected through Hilbert transform.

$$\phi(\omega) = -\mathcal{H}\{\ln(|H(\omega)|)\}$$

3.5 Measuring range and resolving in range

3.5.1 Range accuracy

Range measurements of a single target are characterised by their accuracy. Range accuracy is defined as the standard deviation σ_r or the variance σ_r^2 of the range measurements. It is determined by the statistics used to calculate the range from the return signal.

Matched filter pre-processing is used for range estimation of single target following (3.34). The accuracy with which the range can be determined is measured by the width of the peak in $P_y(\tau)$ (3.35) as shown in Woodward [11, p. 105]. The accuracy in delay estimation is [11, p. 105], [1, Sec. 3.1.]

$$\sigma_t = \frac{1}{\beta\sqrt{\rho}} \tag{3.37}$$

where β is the rms bandwidth (3.17) and ρ is the signal-to-noise ratio (3.16). This is the theoretical limit given by the Cramer-Rao bound (CRLB) for range estimation in white Gaussian noise [91, pp. 53–56]. As noted by Woodward [11, p. 105], equation (3.37) only applies for relatively large signal-to-noise ratios.

3.5.2 The concept of resolution

Range measurements of multiple targets require first the individual targets to be discriminated or “resolved”. Resolving the target can involve different tasks ([1, 90]) – distinguishing two similar scatterers that are located at short distance (range “superresolution”), distinguishing scatterers that differ significantly in strength (sidelobe supression), and discrimination of the target in various forms of clutter. Under the term “resolution” I will discuss only the ability to discriminate two close scatterers.

The standard definition of resolution is based on the autocorrelation function and is given by the half-power width of the point target matched filter response of the waveform [32][11]. It is the minimum separation of two equally strong scatterers that produces on average two response peaks. Following the approach in [1, pp 92], the term **nominal resolution** δ_T (or δ_R when transformed into distance) is defined as the reciprocal of the signal bandwidth:

$$\delta_T = \frac{1}{B_C} \qquad \delta_R = \frac{c}{2}\delta_T \tag{3.38}$$

A different definition of resolution is provided by the Rayleigh criterion, according to which adjacent lines or rings of equal intensity in a diffraction pattern are regarded as resolved when the central maximum of one coincides with the first minimum of the next [92, 93]. For a sinc function shaped response this corresponds to a resolution limit of $1.43\delta_R$.

The above definitions of resolution do not take account of whether the peaks represent the scatterer positions accurately. Rihaczek redefines the notion of resolution in a way to permit an accurate measurement, e.g. of the range [32]. This corresponds to the minimum spacing of $2\delta_R$ when only the intensity output of the receiver is used. This spacing was called **functional resolution** [32]. The functional resolution can be improved to δ_R if the phase output of the receiver is also used and there are only two close scatterers.

The actual ability to resolve two targets can be quantified in different ways. An example metric is the probability of resolution. Two criteria for resolution are summarized in [94] – two targets are resolved if the two peaks can be discriminated even by the presence of an inflection point or if the measurement error of each is less than half the separation between them. The accuracy of the separation estimate can be considered also. In practice, it is often assumed that two echoes are distinguishable when their mainlobes at −3 dB do not overlap [95, p. 56]. Therefore the resolution metric to be used in this thesis is the closest separation of two similar scatterers that yield two distinguishable at −3 dB peaks.

3.6 Description of the SCAT Model

The Spectrogram Correlation And Transformation (SCAT) receiver is a model of the auditory system that was proposed by Saillant *et al.* in [13] for the bat *Eptesicus fuscus*. The SCAT model uses only range information, a single receiver, and does not account for directional sensitivity [13, 14, 15]. In the SCAT, the emitted call and received echoes are frequency modulated signals which are passed through a filter bank which is a model for the bat cochlea. This is followed by a temporal processing block, which is a model for the delay tuned neurons in the brain responsible for target ranging, and by a spectral processing block whose function is to resolve close targets by exploiting echo interferences [13, 15].

A short summary of the SCAT model building blocks (Fig. 3.7) based on [13] follows. Different aspects of the way bats process echoes from stationary targets and the surrounding environment have been studied in the literature and variations of the SCAT have been presented [47], [48], [14]. These will be also discussed where appropriate.

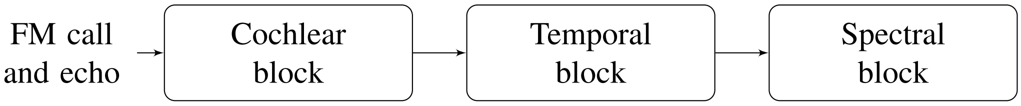

Figure 3.7: The SCAT model main building blocks

3.6.1 Cochlear block

The cochlear block is modelled with a bank of 81 Butterworth band-pass filters of order 10 and bandwidth $B = 4$ kHz. Each filter is followed by a signal rectifier and a 3 kHz bandwidth low-pass filter (Fig. 3.8) in order to extract the envelope of the signal.

The central frequencies f_i of the band-pass filters span the bandwidth between 20 kHz and 100 kHz and are arranged in a hyperbolic scale as $f_i = 1/p_i$, where the central period

p_i changes linearly from 10 μs to 50 μs with increments δp of 0.5 μs. With a 4 kHz bandwidth at the lower-frequency end of the spectrum the filters overlap (channel spacing about 2.5 kHz) but at the upper end the spectrum is slightly undersampled (channel spacing about 5 kHz).

Two levels of smoothing of the envelope have been proposed with the SCAT, namely a high smoothing and a low smoothing. The high smoothing consisting of a full wave rectifier followed by a second order Butterworth low-pass filter, whilst the low smoothing consists of a half wave rectifier followed by a first order low-pass filter. In both cases the low-pass filter has a bandwidth of 3 kHz. The output of the cochlea is called the auditory spectrogram or cochleogram (Fig. 3.9). Signal rectification and low-pass filtering provide an envelope detector which is an analogue technique for narrow-band signal demodulation. A variety of additional digital envelope detection methods are summarized in [96].

In the literature, some modified versions of the original SCAT have been proposed, which differ in how the initial splitting of the signal into frequency channels is carried out. For example, the bank of constant bandwidth Butterworth filters may be replaced by gammatone filters [15] with frequency dependent bandwidths after [44, 45] or Gaussian chirplets with carrier frequencies compatible with the emission sweep rate [14]. More thorough review of the history and the future of the auditory system models is done in [97].

Additional non-linear transformations are proposed to account for the non-linear interactions within the organ of corti [15]. The amplitude of the detected signal is raised to a power of 0.4.

Once the high frequency, wide bandwidth signal has been converted to multiple parallel low frequency signals, further processing by the neural system is possible. The output of the cochlear block is converted into neural spikes. In the original SCAT receiver the

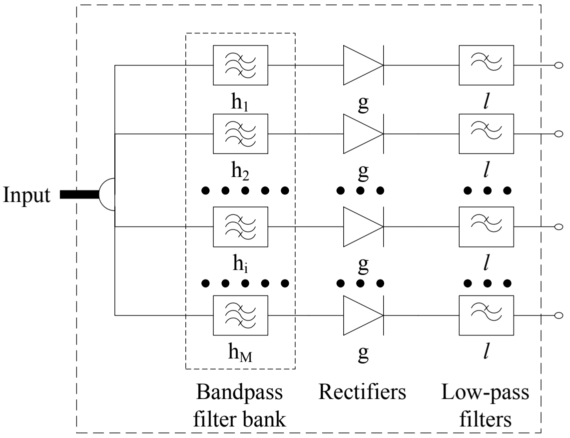

Figure 3.8: Cochlear block of the SCAT receiver. The filter bank consists of $M = 81$ bandpass filters h_i with central frequencies from 20 kHz to 100 kHz. A rectifier and a Butterworth low-pass filter follow after each bandpass filter

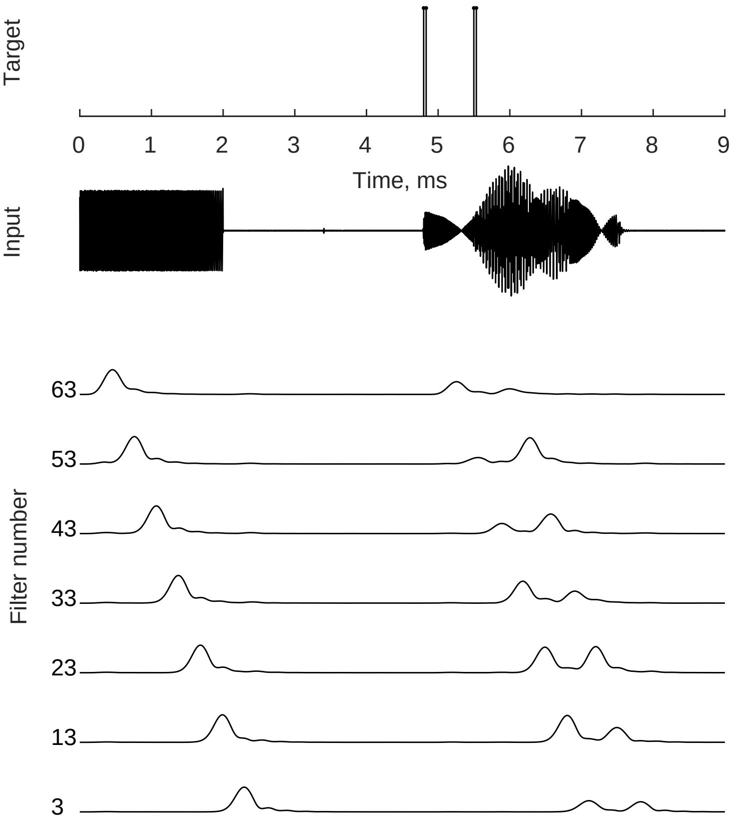

Figure 3.9: Cochlear block output. Two groups of close scatterers at $[4798,\ 4798+18]$ μs and $[5493, 5493+35]$ μs

spike generation algorithm can be implemented in two different ways. One is based on a threshold crossing criteria and the other is based on peak detection. The spike decay period is about 2–4 μs [13, 47]. A spike rise results in an increase of the threshold and inhibits the same neuron in producing another spike. The spike activation threshold decays to its initial value over a period of 1 ms. More recent studies argue that only one to three spikes can be generated per channel [53, 51]. The response latency of the neuron encodes the intensity of the signal (first spike latency coding). The neural coding mechanisms will not be further elaborates as conventional fixed rate sampling will be used.

3.6.2 Temporal block

The purpose of the temporal block is to estimate the time delay between the call and the echo based on the output of the cochlear block. It consists of a set of tapped delay lines that implement a cross-correlation function between the call and the echo. These are triggered by the call signal.

The temporal block carries out a “dechirping” of the signal by adding appropriate delays to each frequency channel (Fig. 3.10). Figure 3.11 shows an example of the output from the temporal block when two groups of scatterers are present. Delays are calculated using the emitted signal shape and rate [13, 24] or each channel is triggered by the emitted signal to make the receiver self-calibrating [47]. A different approach is proposed in [15]. It “dechirps” the signal without explicitly calculating delays by channel-wise autocorrelation.

Simultaneous activity in multiple channels is detected by a set of coincidence detection neurons and is a sign of the target presence. Target detection is implemented by summing the output over all channels and the target is declared with a peak-detection (or threshold crossing) algorithm.

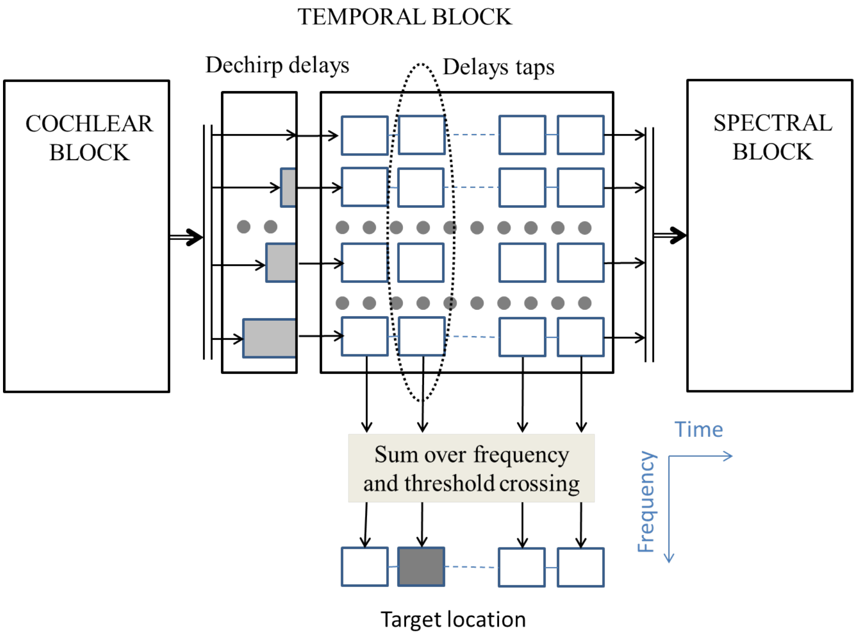

Figure 3.10: Temporal block of the SCAT receiver. Dechirp delays are introduced by triggering/opening each channel by the a transmission call

The mechanism described does not require coherence between the transmitted and received waveform and does not manipulate the phase information. It provides compression of the input chirp from several milliseconds (0.5-15 ms) to several hundreds microseconds (200-300 μs) as the impulse response of the 4 kHz filters is relatively wide (Fig. 3.11). Therefore it can give the location of the targets with relatively low resolution, compared to the matched filter nominal resolution of 15 μs for 65 kHz bandwidth.

3.6.3 Spectral block

The spectral block is responsible for extracting the fine structure of the target. It is used to detect and measure the delay between highly overlapping echoes, which cannot be resolved by the temporal block. It is important because it provides the fine range resolution needed to resolve targets [13].

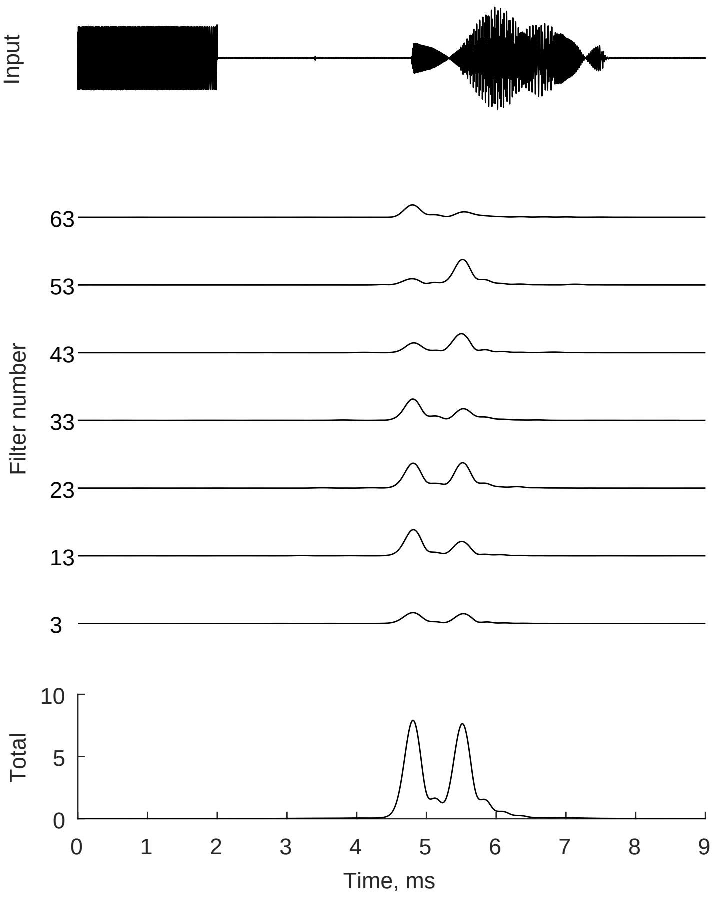

Figure 3.11: Temporal block output

The spectral block exploits the interference pattern between overlapping echoes, which results in the suppression or amplification of the power of the output of some of the filters of the cochlear block. It integrates the output signal of each frequency channel for a specific time interval (about 350 μs [13]) (Fig. 3.12). Each target detected by the temporal block is processed by the spectral block separately. For example, the two peaks in Fig. 3.11 produce two interference patterns as shown in Fig. 3.13.

The output of the integration represents the frequency spectrum of the return signal from the target. It is next normalised by the interference pattern of the emitted call to get a target signature in the frequency domain. This is needed to compensate for the hyperbolic distribution of the energy when hyperbolic FM waveform is used. An example

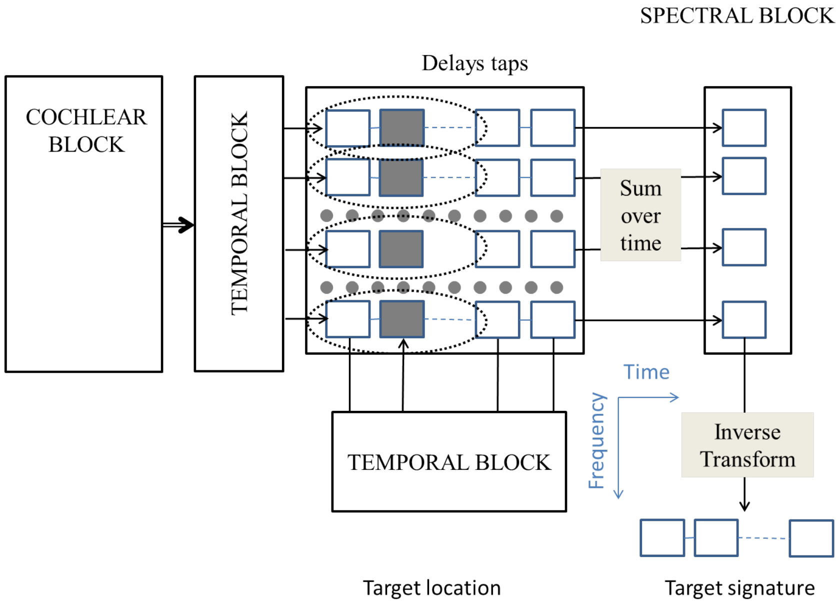

Figure 3.12: Spectral block of the SCAT receiver. Target signature could be presented in the frequency or in the time domain

with hyperbolic waveform and hyperbolic filter distribution is provided in Fig. 3.14. Some studies emphasize the spectral based perception of the target [15, 33, 30] but others argue that time domain reconstruction of the target image is also needed [13, 14, 47].

Original SCAT propose the so called "voting mechanism" to transform the echo spectrum back onto the time axis. It is a modified inverse cosine transform suitable for the hyperbolic waveform and hyperbolic frequency sampling. A "pattern-matching" interpretation of the transformation of spectral interference patterns into fine delays is proposed in [48]. More recent developments of SCAT propose a mechanism to extract the spectral zeroes locations and then feed them to a neural network to reconstruct the target shape on the range axis [63].

The inverse cosine transformation of the frequency spectrum $E(f)$ is defined by

$$x(\tau) = \int E(f)\cos(2\pi f\tau)\mathrm{d}f, \tag{3.39}$$

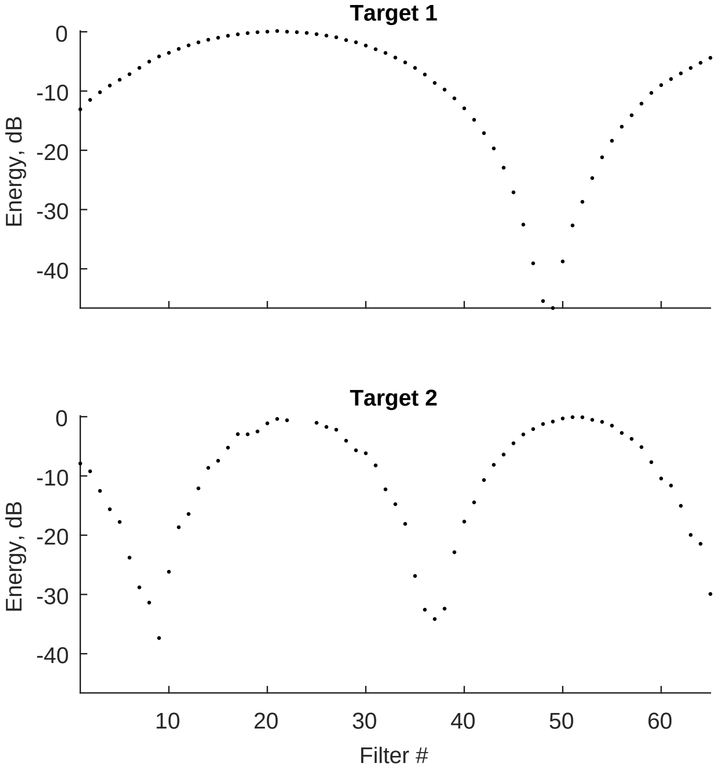

Figure 3.13: Spectral output, linear distribution of the filter central frequencies

where $x(\tau)$ is the fine delay profile and τ is the fine delay axis. For discrete frequencies the integral is replaced by summation. For hyperbolic sampling rate on the frequency axis the step in frequency $\mathrm{d}f$ is replaced by step in period $\frac{\delta p}{p^2-(\delta p/2)^2}$ [13, 48]

$$x(\tau) = \sum_{i=1}^{M} E[f_i] \cdot \frac{\delta p}{p_i^2 - (\delta p/2)^2} \cdot \cos(2\pi f_i \tau), \tag{3.40}$$

The above equation always produces a strong peak at zero location [13]. Modification of the basis functions $\frac{\delta p}{p_i^2-(\delta p/2)^2} \cdot \cos(2\pi f_i \tau)$ by subtracting its mean value over frequency was proposed in [13]. This approach was further explained in [48] where an equivalent but simpler implementation was given. The energies $E[f_i]$ in (3.40) are replaced by

$$\hat{E}[f_i] = E[f_i] - \frac{1}{M} \sum_{i=1}^{M} E[f_i] \tag{3.41}$$

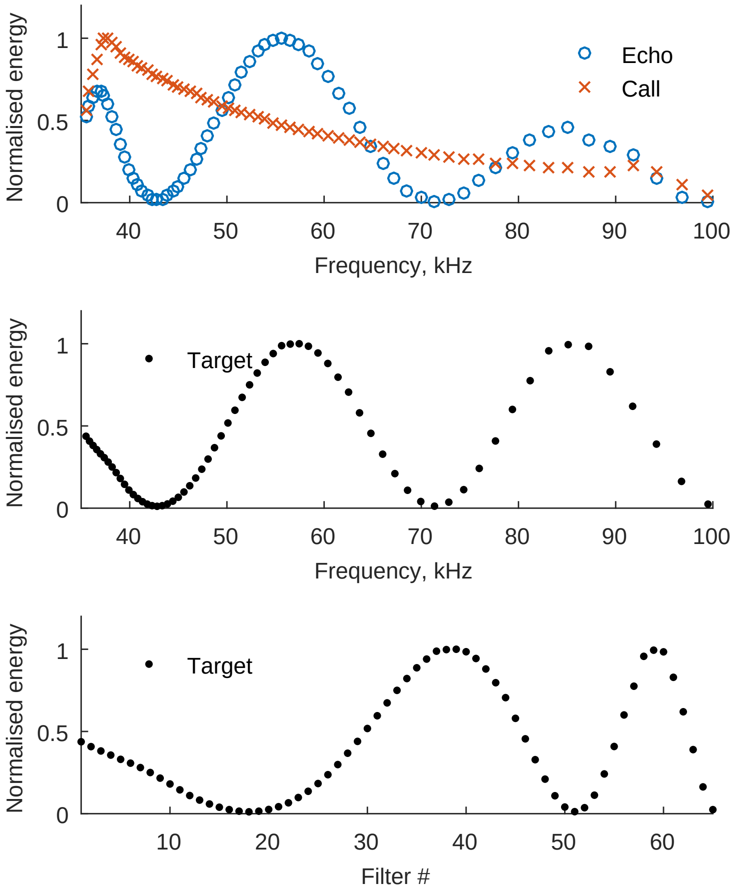

Figure 3.14: Spectral output, hyperbolic distribution of the filter central frequencies. The echo response has to be divided by the call response in order to compensate for the hyperbolic distribution of the energy

The frequency profiles shown in Fig. 3.13 are shown as fine delay profiles in Fig. 3.15. Only the intensity of the receiver (in dB) is presented in the time domain. The phase information is ignored.

3.6.4 Model output

The outputs of temporal and spectral blocks could be considered separately. For a group of closely positioned targets the former gives information about location on the time (range) axis for the group as a whole, and the latter describes the intra-group behaviour either as

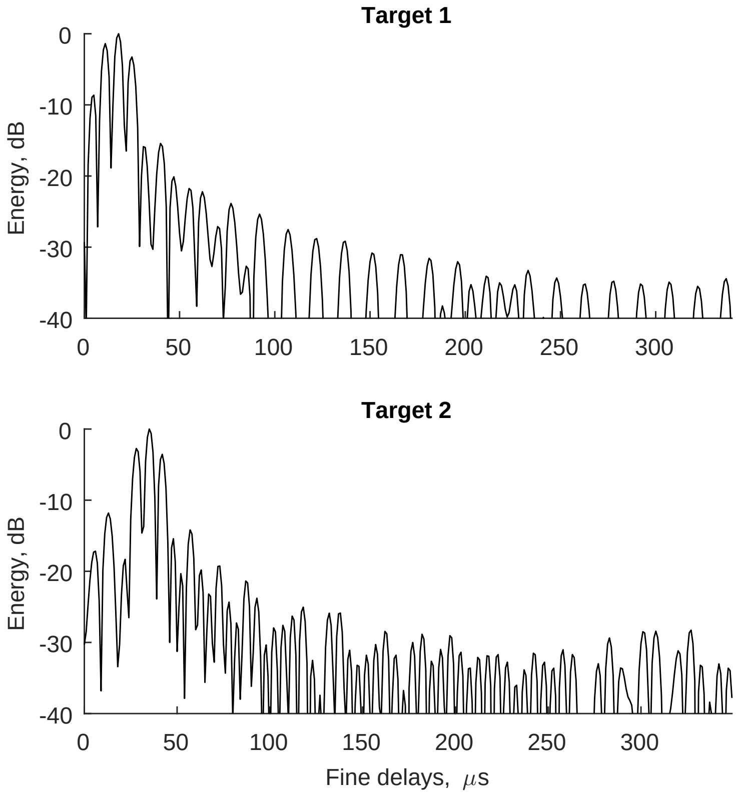

Figure 3.15: Fine delay profiles

spectrum reflecting the interferences or as fine delays (relative distances).

3.7 Summary

The main principles and building blocks of a radar receiver and the bat auditory system processing (SCAT receiver in particular) were discussed. Downconversion to complex baseband, representation and parameters of a modulated signal, filter banks, spectral power and matched filtering are concepts that will be used in the next chapter to study the SCAT from a radar applications perspective.

Chapter 4

Bioinspired resolution of closely spaced targets

In this chapter, a baseband receiver equivalent to the SCAT is developed that allows an analytical treatment of the bat-like processing output and that can be applied to RF signals with carrier frequencies and bandwidths much larger than those of sonar. The output of the Baseband SCAT (BSCT) is compared analytically with the output of the conventional matched filter for two closely spaced scatterers. It is shown that the BSCT can provide improved range resolution performance with respect to the matched filter.

4.1 The Baseband Spectrogram Transformation receiver

In this section, a baseband equivalent of the spectrogram transformation receiver is developed that can treat analytical input signals at baseband (Fig. 4.1). It is also applicable to RF signals at very high frequencies (bandpass signals) which are treated as low frequency complex signals (baseband signals). Down-conversion to baseband is essential to digitise bandpass signals meeting the Nyquist criterion and, it also provides analytical advantages as signals can be represented in a much simpler complex form. For implementational simplicity, the baseband SCAT (BSCT) is based on filters with a linear distribution in frequency. Whilst this is probably a slightly worse approximation than the hyperbolic distribution discussed in Chapter 3, Sec. 3.6, this difference in approach is not significant since both distributions are only approximations and, if it is robust, the behaviour of the model will not be very sensitive to such details.

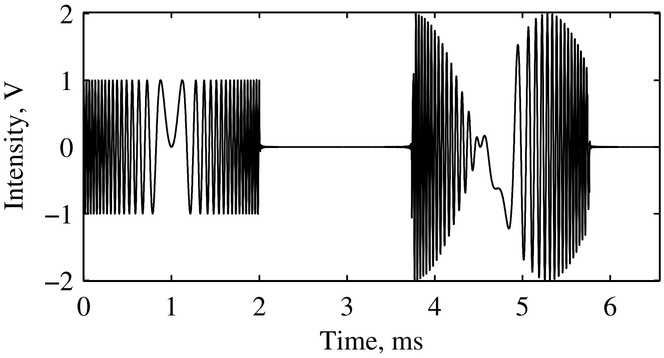

Figure 4.1: In-phase component of the baseband model input. The signal frequency is shifted to baseband. The emitted call has duration of 2 ms and spans linearly the frequencies from -32.5 kHz to +32.5 kHz. The received echo comes from two scatterers with a relative delay of 20 μs and equal amplitude.

Let us consider a filter bank of M filters with central frequencies f_i, $i = 0 \ldots M-1$ and bandwidth B (Fig. 4.2). If the filters have all the same design, the Fourier transform $H_i(f)$ of the impulse response $h_i(t)$ for the i-th filter can be obtained by shifting in frequency a baseband (low-pass) filter response $h(t)$ as

$$h_i(t) = h(t)e^{j2\pi f_i t} \tag{4.1}$$

$$H_i(f) = H(f - f_i) \tag{4.2}$$

where $H(f)$ is the Fourier transform of $h(t)$. The output of the i-th filter is the convolution between the filter impulse response and the input signal $x(t)$

$$y_i(t) = x(t) * h_i(t) \tag{4.3}$$

The rectifiers and the low-pass filters that follow each bandpass filter of the original cochlear block (Fig. 3.8) are replaced with an ideal amplitude extractor, so that the envelope of the bandpass filtered signal can be modelled with the amplitude of the signal $y_i(t)$ (Fig. 4.3). This alternative to the rectifier and low-pass filter discards completely the phase information of the signal $y_i(t)$. Then the envelopes are converted to an auditory spectrogram by squaring the amplitude of $y_i(t)$ (Fig. 4.4).

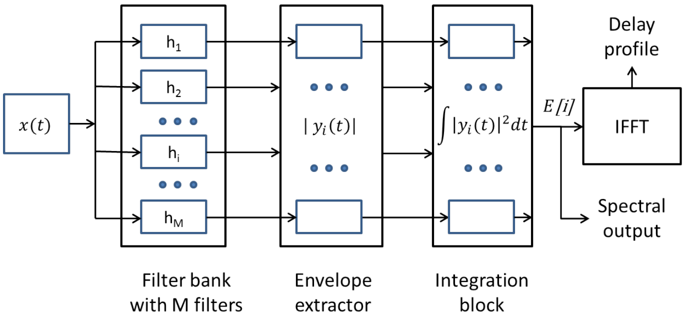

Figure 4.2: BSCT spectral processing diagram. The model input $x(t)$ is an analytical signal. It is passed through a filter bank of M complex bandpass filters h_i. The absolute value of each filter output y_i is squared and integrated over time to get the energy $E[i]$ at the corresponding frequency.

In the spectral block, the total energy of the output of each filter is computed by integration (Fig. 4.2). In order to separate the spectral signature of multiple groups of scatterers, the integration is limited to an interval around the location of the group of echoes under consideration (Fig. 4.4) so that each group can be analysed separately. The group locations for each frequency are extracted by the temporal block.

When only a single group of scatterers is present, the temporal block can be ignored

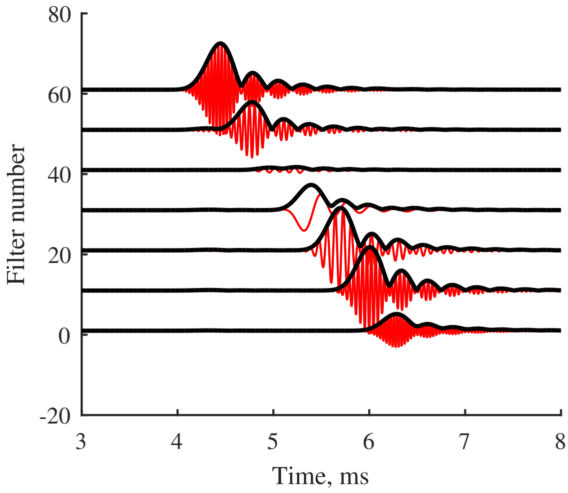

Figure 4.3: Bandpass filter bank output, in-phase (real) component and envelope

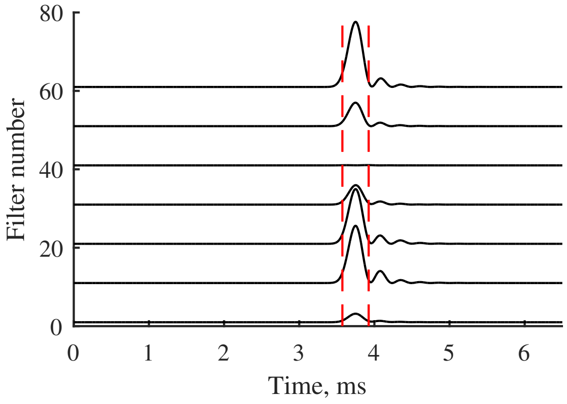

Figure 4.4: Example of de-chirped squared envelopes for seven filters and integration interval (red dashed lines) over which the total energy for each filter is calculated

and the output of the spectral block can be obtained by integrating the whole filter output following equation (4.4), below:

$$E[i] = \int_{-\infty}^{\infty} |y_i(t)|^2 \, dt = \int_{-\infty}^{\infty} |Y_i(f)|^2 \, df \tag{4.4}$$

$$E[i] = \int_{-\infty}^{\infty} |X(f)|^2 \, |H(f - f_i)|^2 \, df \tag{4.5}$$

When all narrow-band filters in the filter bank have a perfectly flat frequency response over a bandwidth B,

$$H_i(f) = \text{rect}\left(\frac{f - f_i}{B}\right) \tag{4.6}$$

where f_i is the center frequency of the i'th filter and

$$\text{rect}\left(\frac{f}{B}\right) = \begin{cases} 1, & |f| \leq \frac{B}{2} \\ 0, & \text{otherwise} \end{cases}$$

The filter bank spectral output is

$$\begin{aligned} E[i] &= \int_{-\infty}^{\infty} |X(f)|^2 |H(f - f_i)|^2 df \\ &= \int_{f_i - B/2}^{f_i + B/2} |X(f)|^2 df \\ &= \int_{f_i - B/2}^{f_i + B/2} P(f) df \end{aligned} \tag{4.7}$$

$P(f)$ is the spectral energy density of $x(t)$. Equation (4.7) shows the spectrogram transformation provides the signal spectral energy of the input signal integrated over a bandwidth B around the central frequencies f_i. In other words, it is equivalent to digitising the energy spectral density by averaging across the filter bandwidth.

Finally, the sequence $E[i]$ is transformed into the time domain to obtain the output signal of the spectral block. Assuming the central frequencies f_i are linearly spaced this transformation can be obtained with an Inverse Fast Fourier Transform (IFFT).

4.2 Response of the BSCT to two closely spaced ideal reflectors

The response of the BSCT to the echo from two closely spaced ideal point reflectors is studied in order to investigate the range resolution properties of the model and to allow a comparison with the matched-filter. An ideal point reflector (target, scatterer) is defined as an object that reflects the signal without changing its magnitude and phase for all frequencies. When two ideal targets are present, the complex envelope of the input signal $x(t)$ is the sum of two delayed replicas of the complex envelope of the transmitted signal $x_C(t)$

$$x(t) = x_C(t-t_1)e^{-j2\pi f_0 t_1} + x_C(t-t_2)e^{-j2\pi f_0 t_2} \tag{4.8}$$

where t_1 and t_2 are the time-delays of the echo from the first and second target, respectively and f_0 is the carrier frequency. For simplicity of notation, the difference between the two delays will be denoted as $\tau = t_2 - t_1$.

The Fourier transform of $x(t)$ can be written as a function of the Fourier transform $X_C(f)$ of the signal $x_C(t)$ as

$$\begin{aligned}
X(f) &= X_C(f)e^{-j2\pi(f+f_0)t_1} + X_C(f)e^{-j2\pi(f+f_0)t_2} \\
&= X_C(f)e^{-j2\pi f^I t_1}\left(1 + e^{-j2\pi f^I (t_2-t_1)}\right) \\
&= X_C(f)e^{-j2\pi f^I t_1}e^{-j\pi f^I \tau}\left(e^{j\pi f^I \tau} + e^{-j\pi f^I \tau}\right) \\
&= X_C(f)e^{-j2\pi f^I t_1}e^{-j\pi f^I \tau}2\cos(\pi f^I \tau) \\
&= X_C(f)e^{-j2\pi f^I t_1}e^{-j\pi f^I \tau}2\cos(\pi f \tau + \frac{\psi_\tau}{2})
\end{aligned} \tag{4.9}$$

and its energy spectral density $P(f) = |X(f)|^2$ is

$$
\begin{aligned}
P(f) &= |X_C(f)|^2 4\cos^2(\pi f \tau + \frac{\psi_\tau}{2}) \\
&= 2P_C(f)\left[\cos(2\pi f \tau + \psi_\tau) + 1\right]
\end{aligned}
\tag{4.10}
$$

where $P_C(f)$ is the energy spectrum of the transmitted call, $f^I = f + f_0$ is the frequency before down-conversion and $\psi_\tau = 2\pi\tau f_0$ is the phase due to frequency down-conversion.

Let us assume that the transmitted signal $x_C(t)$ is a Linearly Frequency Modulated chirp (LFM) $s(t)$ with a bandwidth B_C and duration T of the form

$$
s(t) = e^{j\pi\gamma t^2}\mathrm{rect}\left(\frac{t}{T}\right) \tag{4.11}
$$

where $\gamma = B_C/T$ is the chirp rate. The Fourier transform of the linear chirp $S(f)$ is given by

$$
\begin{aligned}
S(f) &= \int_{-\infty}^{\infty} s(t)e^{-j2\pi f t}dt \\
&= \int_{-\infty}^{\infty} \mathrm{rect}\left(\frac{t}{T}\right)e^{-j2\pi\left(ft - \frac{\gamma t^2}{2}\right)}dt \\
&= \int_{-T/2}^{T/2} e^{-j2\pi\left(ft - \frac{\gamma t^2}{2}\right)}dt
\end{aligned}
\tag{4.12}
$$

The analytical equations derived from (4.12) are available [98, 12] and these account for the magnitude of the ripples and for the phase of the spectrum that consists of a square law term and a residual term. However, as the above equations are not in a closed form, a simplified representation can be derived by using the stationary phase approximation of oscillatory integrals [12, 99] for high time-bandwidth products $B_C T$:

$$\int_{-\infty}^{\infty} f(t)e^{jk\mu(t)}\mathrm{d}t \approx \mathrm{e}^{jk\mu(t^*)} f(t^*)\sqrt{\frac{2\pi}{k|\mu''(t^*)|}} \cdot \exp\left[\frac{\mu''(t^*)}{|\mu''(t^*)|}\frac{j\pi}{4}\right] \tag{4.13}$$

where t^* is the time at which the phase stationarity is obtained, i.e. $\mu'(t^*) = 0$ and $k \gg 1$. The result of the approximation is a simple expression for the chirp spectrum

$$S(f) = \mathrm{rect}\left(\frac{f}{B_C}\right)\sqrt{\frac{1}{\gamma}} \cdot \mathrm{e}^{-j\pi\frac{1}{\gamma}f^2}\mathrm{e}^{j\frac{\pi}{4}} \tag{4.14}$$

that consists of a constant magnitude, a square law phase modulation and a constant phase residual of $\pi/4$.

When the input signal is a single chirp, the output of the spectrogram transformation block (4.7) becomes

$$E_S[i] = \int_{f_i-\frac{B}{2}}^{f_i+\frac{B}{2}} |S(f)|^2 df = \int_{f_i-\frac{B}{2}}^{f_i+\frac{B}{2}} \frac{1}{\gamma} df = \frac{B}{\gamma} = \frac{B}{B_C}T \tag{4.15}$$

for $-B_C/2 < f_i < B_C/2$ and zero otherwise.

The energy spectral density $P(f)$ of the return $x(t)$ from two scatterers can be written as

$$P(f) = 2\frac{1}{\gamma} \cdot [\cos(2\pi f\tau + \psi_\tau) + 1] \cdot \mathrm{rect}\left(\frac{f}{B_C}\right) \tag{4.16}$$

and the output of each filter

$$
\begin{aligned}
E_E[i] &= \frac{2}{\gamma}\int_{f_i-B/2}^{f_i+B/2}\left[\cos(2\pi f\tau+\psi_\tau)+1\right]df \\
&= \frac{2B}{\gamma}\left[\frac{1}{\pi\tau B}\sin(\pi\tau B)\cos(2\pi\tau f_i+\psi_\tau)+1\right] \\
&= 2E_S\left[\operatorname{sinc}(\tau B)\cos(2\pi\tau f_i+\psi_\tau)+1\right] \qquad (4.17)
\end{aligned}
$$

for $-B_C/2 \le f_i \le B_C/2$ and $E_E[i]=0$ otherwise, where $\operatorname{sinc}(x)=\sin(\pi x)/(\pi x)$ and $E_S = B/\gamma = E_S[i]$.

Equation (4.17) shows that the spectral output of the SCAT is the sum of a weighted sinusoid and a constant multiplied by a rectangular window. The frequency of the sinusoid is actually the time spacing of the targets τ. The lowest energy outputs, $\min(E_E[i])$ are determined by both B and τ.

Figure 4.5 shows an example of the energy output for a filter bank of 65 filters with central frequencies distributed linearly between -32 kHz and 32 kHz and with 4 kHz bandwidth. The results are for an input signal consisting of the sum of two LFM chirps with a bandwidth of 65 kHz, center frequency of 67.5 kHz, a duration of 2 ms and a relative time delay of 36 μs. Setting $\tau = 36$ μs, $B = 4$ kHz and $\psi_\tau = 2\pi\tau f_0$ in (4.17) gives the theoretical curve. Applying the FFT on a simulated chirp sequence with the above parameters and integrating as in (4.7) gives the simulated discrete points on the graph. The simulated curve is a good approximation of the theoretical output of the BSCT. The deviations near the boundaries appear because of those filters at the two ends of the spectrum that cover frequencies with no signal and because the chirp magnitude is not a perfect rectangular function in the frequency domain.

Considering the discrete output of the filter bank in (4.17), an inverse Fourier Series will produce a periodic continuous signal in the time domain. The $E_E(i)$ can be viewed as

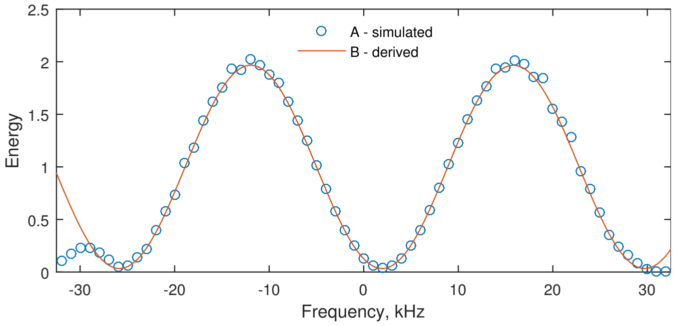

Figure 4.5: Model output, energy E_E by filter i, $i = 1 \dots 65$, $B = 4$ kHz, for two overlapping chirps with duration 2 ms, f_1 = 35 kHz, f_n = 100 kHz and a relative delay τ = 36 μm. Based on (A), simulated input and (B), the derived theoretical solution in (4.17).

the Discrete Fourier Transform of a sequence with a limited bandwidth, B_C, and digitized with a sampling rate $f_s > 2B_C$. The resulting sequence in the time domain is

$$\begin{aligned}
&\mathcal{F}_f^{-1}[E_E[i]](t) = \\
&= 2\frac{B}{\gamma}\mathcal{F}_f^{-1}[\operatorname{sinc}(B\tau)\cos(2\pi f_i\tau + \psi_\tau) + 1](t) * MD_{B_C,M}(t) \\
&= 2\frac{BM}{\gamma}\left[\frac{b\cdot e^{j\psi_\tau}}{2}D_{B_C,M}(t-\tau) + \frac{b\cdot e^{-j\psi_\tau}}{2}D_{B_C,M}(t+\tau) + D_{B_C,M}(t)\right] \qquad (4.18)
\end{aligned}$$

where $b = \operatorname{sinc}(B\tau)$ and

$$\begin{aligned}
D_{B_C,M}(t) &= \frac{1}{M}\mathcal{F}_f^{-1}[\operatorname{rect}\left(\frac{f_i}{B_C}\right)](t) \\
&= \frac{1}{M}\frac{\sin\pi B_C t}{\sin\pi\frac{B_C}{M}t} = \frac{\operatorname{sinc} B_C t}{\operatorname{sinc}\frac{B_C}{M}t}
\end{aligned}$$

The inverse Fourier transform of (4.17) is the sum of three sinc functions one of which does not depend on the relative delay between the two targets. The two sinc functions centred at $\pm\tau$, instead, allow an estimation of the delay between the two echoes. It is important to highlight that the two peaks centred at $\pm\tau$ are scaled by constant $b = \mathrm{sinc}(B\tau)$, which depends on the filter bandwidth B and the delay τ between the scatterers, and this indicates that distant scatterers are attenuated (or 'low-pass filtered').

In the theoretical developments above it was assumed that the targets are ideal reflectors and the potential phase shifts from the reflectors were not taken into account. Such shift will introduce an unknown or random element in the phase ψ_τ e.g. in (4.10), (4.16), (4.17) and (4.18).

4.3 Analysis of the Spectrogram Transformation

4.3.1 Central lobe suppression

Without further processing the time resolution of two closely located scatterers of the bio-inspired spectrogram transformation is the same as the resolution achieved by the matched filter. The distance between the sinc functions is τ as for the matched filter and the width of the lobes in the time domain at -3 dB is the reciprocal of the bandwidth of the signal (or that of the filter bank if it is less):

$$\Delta\tau = \frac{1}{B_C}$$

However, the central lobe does not depend on the position of the targets and can be suppressed to double the distance between the two lobes at $\pm\tau$. If the suppression of the central lobe is achieved then the distance between the two sinc functions is increased from τ to 2τ and the functional range resolution is improved so that two targets at half the range separation can be resolved (Fig. 4.6). Furthermore, because of the resulting representation is symmetrical, it can be folded back on itself so there is then essentially only a single peak. This means that measuring the relative distance between two targets has been made as simple as measuring the range to a single target, which can reliably be done to very high accuracy given an adequate signal to noise ratio [1, Sec. 3.1]. There are a few approaches that can be considered to remove the central lobe. One is to use the knowledge of the transmitted signal energy and take a suitably scaled difference and another is to remove the average value of the spectral energy over the bandwidth before taking the inverse Fourier transform [48].

Removing the mean of (4.17) leads to

$$\begin{aligned} E_{E'}(f) &= E_E(f) - \frac{1}{B_C}\int_{-\frac{B_C}{2}}^{\frac{B_C}{2}} E_E(f)df \cdot \mathrm{rect}\left(\frac{f}{B_C}\right) \\ &= 2\frac{1}{\gamma}\cdot\Big[\mathrm{sinc}(\tau B)\cos(2\pi f\tau + \psi_\tau) - \\ &\quad - \mathrm{sinc}(\tau B)\,\mathrm{sinc}\,(\tau B_C)\cos\psi_\tau\Big] \end{aligned} \tag{4.19}$$

Results show that, with this method, the inverse Fourier transform of (4.19) will still have a residual zero lobe component but it will be reduced from one to less than $\mathrm{sinc}(\tau B)\,\mathrm{sinc}\,(\tau B_C)$. The zero lobe suppression mechanism can be interpreted in the time domain also. Simulations show that subtracting the normalized time domain representation of the BSCT for a single scatterer from the corresponding representation for two scatterers have the same effect.

The resolution of two closely located targets is illustrated in Fig. 4.7 where the lobe interference is presented for different spacings between the targets and different types of processing. It shows the output of the matched filter, the inverse of the spectrogram transformation (4.17) and the effect of the zero lobe removal correspondingly. The magnitudes for both spectrogram related approaches are normalized by the magnitude of the central lobe before the suppression.

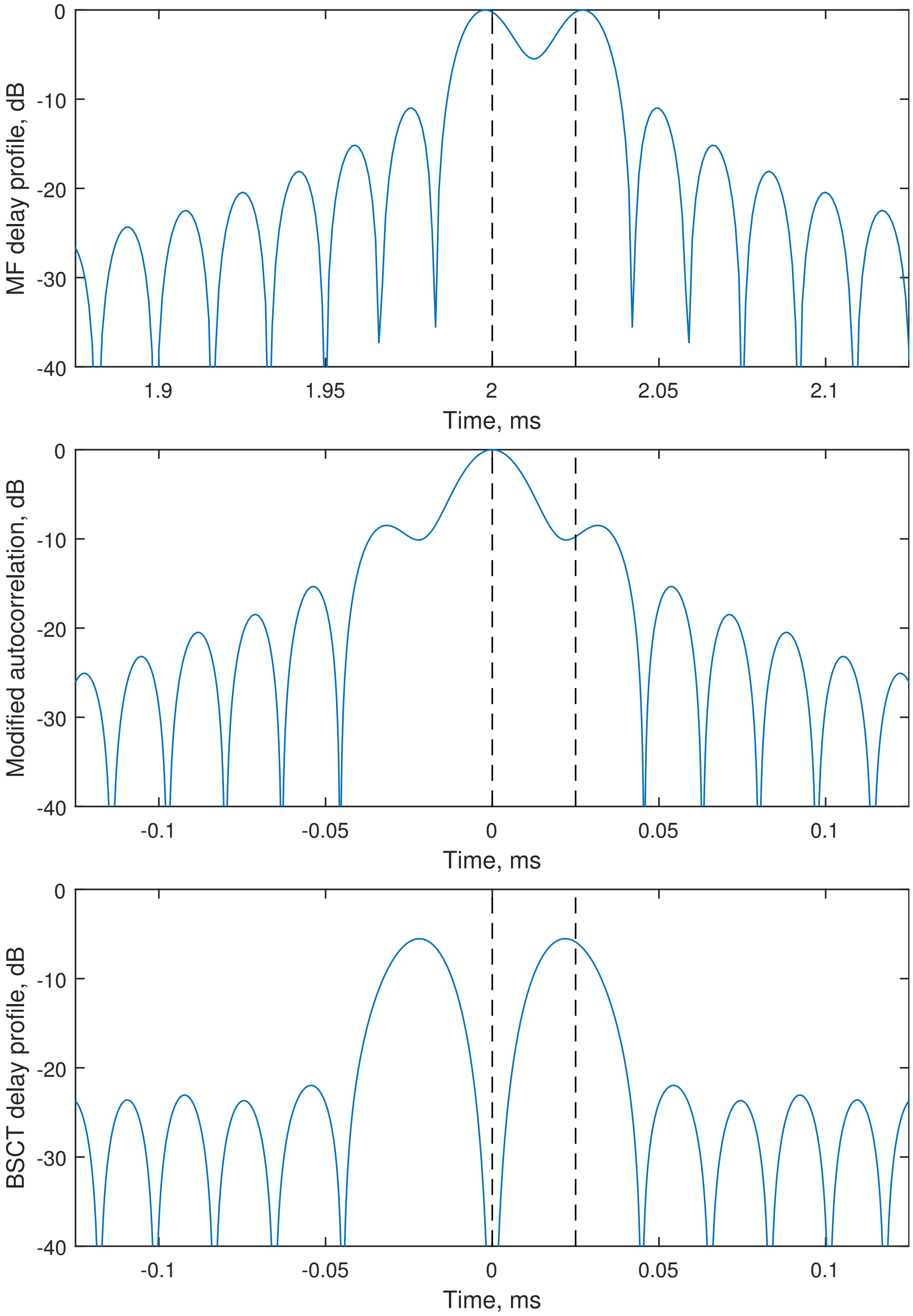

Figure 4.6: Matched filter compared to BSCT and the effect of the zero lobe suppression , $B_C = 65$ kHz, $t_1 = 2$ ms, $\tau = 1.6\frac{1}{B_C} = 25\,\mu s$. While the lobe width is the same the functional resolution is improved by doubling the spacing between the lobes.

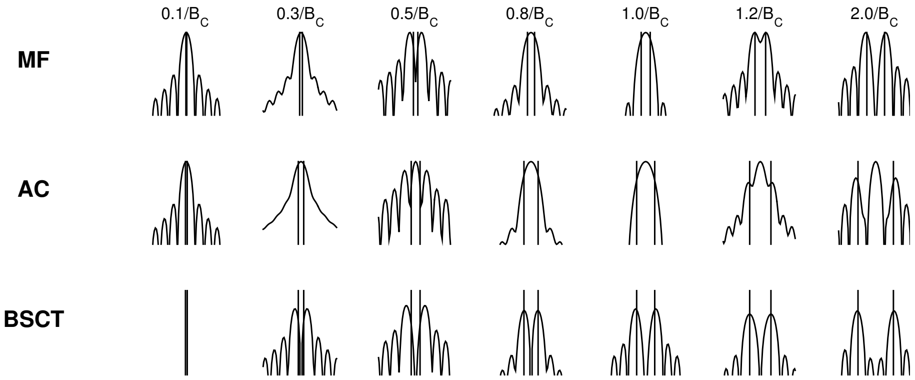

Figure 4.7: Fine delay profiles for different delays between two close targets near the resolution limit $1/B_C$. Two sinc interference typical for matched filtering [32] is presented in the top row. The simple inverse transform of the spectrogram transformation is denoted as “AC” as a form of autocorrelation. The bottom row shows the zero lobe removal effect. The true locations are indicated by the vertical bars.

4.3.2 Phase shift or zero location hints

Even though the analysis are in baseband the initial frequency range of the signal is still preserved in the equations in the phase of the sinusoid. To exploit this information the frequencies f_z where the energy is minimal (the zeroes of the spectrum) are calculated as

$$\begin{aligned} f_z = \{f_i \mid \min_{f_i} E_E[i]\} &= \underset{f_i}{\operatorname{argmin}}[\cos(2\pi\tau f_i + \psi_\tau)] \\ f_z &= \frac{0.5+n}{\tau} - f_0, \quad n = 0, 1, \ldots \end{aligned} \tag{4.20}$$

The locations of the peaks and notches are discussed in [13, 47, 53] as possible mechanism for relative delay estimation. Single and dual frequency tuned neurons are mapped in the auditory cortex by measuring the electrical activity recorded from microelectrodes in response to pure tone and paired frequency modulated signals [13, 53, 100, 101].

If $f_0 = B_C$, which corresponds to bat sonar, then a single zero located in the bandwidth $-B_C/2 < f_z < +B_C/2$ corresponds to only two possible delays τ

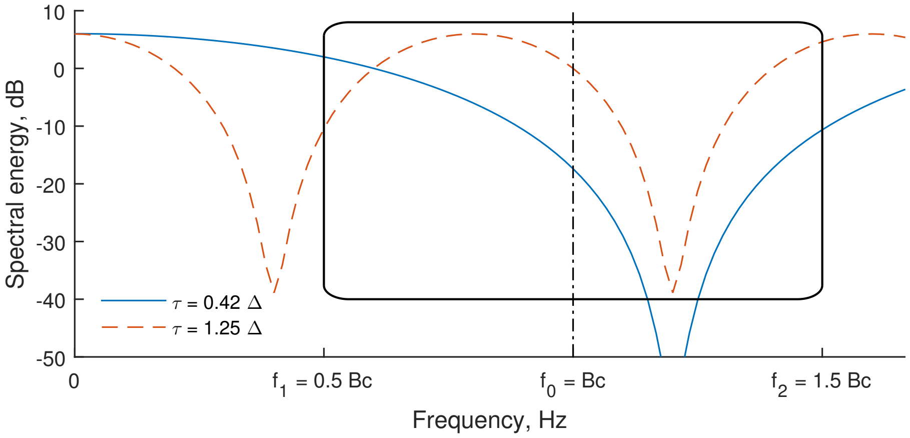

Figure 4.8: Frequency profile (energy in dB). For close targets there is a single zero in the receiver bandwidth. The zero location can be translated to delay following (4.21). The depth of the zero can be used to resolve the ambiguity if two delays are possible. The bandwidth of the receiver is B_C and the nominal resolution is $\Delta = \frac{1}{B_C}$. The signal is not down-converted to baseband in order to show the order of the zero

$$\begin{aligned} &\text{if} \quad n=0 \quad \text{then} \quad \tau = \frac{0.5}{f_z+f_0}, \quad \frac{1}{3}\frac{1}{B_C} < \tau < \frac{1}{B_C} \\ &\text{if} \quad n=1 \quad \text{then} \quad \tau = \frac{1.5}{f_z+f_0}, \quad \frac{1}{B_C} < \tau < \frac{5}{3}\frac{1}{B_C} \end{aligned} \tag{4.21}$$

Therefore resolution down to one third of the nominal resolution can be expected. The ambiguity can be resolved based on the different value of the energy in the zeroes (lower delays correspond to minimal energy closer to the zero) (Fig. 4.8).

For f_0 much higher than B_C the effect of the zero shift for measurements from different locations still can be exploited by considering the derivative of (4.20)

$$\frac{df_z}{d\tau} = -\frac{f_z+f_0}{\tau} \approx -\frac{f_0}{\tau} \tag{4.22}$$

From the equation above, it follows that for closer targets minor changes in the spacing will result in faster zero shifting. This method of using the carrier phase to measure relative range does not suffer from ambiguities to the same extent as is usually the case in radar because the relative bandwidths of the signals is so much higher in this case.

It is worth remembering again at this point that although the mathematical operations described above might seem somewhat intricate, the data rates at the filter outputs are modest and a bat could be plausibly expected to be able perform quite sophisticated pattern recognition, on the basis of the widespread appreciation that animal brains are actually very good at such techniques.

4.3.3 Relationship between the BSCT receiver and the matched filter

Matched filtering of $x(t)$ with $x_C(t)$ will have an output $x_M(t)$ as follows:

$$\begin{aligned}
x_M(t) &= x(t) \star x_C(t) \\
X_M(f) &= X(f) X_C^*(f) \\
&= X_C(f) e^{-j2\pi f^I t_1} e^{-j\pi f^I \tau} 2\cos(\pi f^I \tau) X_C^*(f) \\
&= 2|X_C(f)|^2 \cos(\pi f^I \tau) \cdot e^{-j2\pi f^I t_1} e^{-j\pi f^I \tau}
\end{aligned} \tag{4.23}$$

Above equation can be compared with (4.9) to show that the only difference is that the waveform $X_C(f)$ is replaced by its magnitude squared $|X_C(f)|^2$ – the phase stretching of the signal in time is removed and the energy is increased. Assuming flat signal spectrum (4.14) means that $|X_M(f)|^2$ is just a scaled version of $|X(f)|^2$. Matched filter compressed signal can be processed through (4.7) to receive the same BSCT spectral output pattern:

$$\begin{aligned}
E_M[i] &= \int_{f_i - B/2}^{f_i + B/2} |X_M(f)|^2 df \\
&= \frac{2B}{\gamma^2} \cdot [\text{sinc}(B\tau) cos(2\pi f_i \tau + \psi_\tau) + 1]
\end{aligned} \tag{4.24}$$

This is scaled by constant version of (4.17). Therefore the temporal processing (dechirping) in SCAT can be replaced by conventional matched filtering. The time compression is important in real environment to split the range into cells, which can be processed independently.

Using the same simplifications about the signal (4.14) it can be written for the output of the matched filter in the time domain, starting from (4.23)

$$\begin{aligned} \mathcal{F}_f^{-1}[X_M(f)] = &= \left[e^{j\frac{\psi\tau}{2}}\delta(t-t_1) + e^{-j\frac{\psi\tau}{2}}\delta(t-t_1-\tau)\right] * \mathcal{F}_f^{-1}[|X_C(f)|^2] \\ &= \frac{|B_C|}{\gamma}\left[e^{j\frac{\psi\tau}{2}}\operatorname{sinc} B_C(t-t_1-\tau) + e^{-j\frac{\psi\tau}{2}}\operatorname{sinc} B_C(t-t_1)\right] \end{aligned} \tag{4.25}$$

Two sinc functions delayed with t_1 and $t_2 = t_1 + \tau$ can be noticed. In contrast BSCT gives two sinc functions delayed with $-\tau$ and $+\tau$ (assuming ideal removal of the the central lobe in (4.18)).

Unlike the matched filter response, the output of the BSCT encodes directly the spacing between the scatterers and not the absolute range of the targets. The problem of measuring the relative distance is converted to a problem of measuring the range to a single target. As the representation is symmetrical, there is a second peak at negative delays but the peaks interfere less than the peaks produced by a matched filter because the separation is double. Therefore, nearly double improvement in the resolution should be expected.

The fine delay profile will be further referred to as the spacing profile to emphasise the nature of the information conveyed, i.e. not the absolute location of the scatterers but the spacing between them.

4.4 Summary

An approach for analytical treatment of the SCAT model was proposed. A sequence of simplifications were applied in order to explain the output of the model. The spectral output of the resulting BSCT receiver for two targets is a sinusoid whose frequency and phase are related to the spacing between the targets. The BSCT is complimentary to the MF and provides improved range resolution for two close targets. The theoretical results will be validated experimentally in the following chapters.

Chapter 5

Validation of the BSCT model for ultrasound

In this chapter the equivalence of BSCT to the SCAT is demonstrated by comparing the spectral output of the original and baseband model using both simulated signals and laboratory measurements. The scope of the investigation was limited to the spectral part of the model because that is the component of the SCAT that can potentially provide the fine range resolution needed for target detection and discrimination.

With another set of laboratory experiments at ultrasound, using phantom echoes and real targets, the expected improvement in range resolution relative to the conventional matched filter is confirmed.

5.1 Experimental set up and data collection

This section describes experiments employing real and phantom targets at ultrasound. Simulated data that mirror the experiments is generated to allow a comparison between experiments and simulations. Phantom target experiments are useful to test the robustness of the algorithm with respect to the hardware imperfections, such as non-linearities and a non-flat frequency response, and propagation effects. Real target experiments, in addition, test the robustness of the algorithm for non-ideal reflectors.

5.1.1 General settings and equipment

For both the simulations and the experiments, 10 ms long recordings were sampled at a rate of 10 MHz to collect 100 000 samples per realisation. The signal was decimated by 10 before further processing. Echoes were recorded with an ultrasound microphone (type CM16, Avisoft Bioacoustics, Berlin, Germany) and waveforms were transmitted with an ultrasound loudspeaker (type S55/6, Ultra Sound Advice, London, UK). Digital to analogue and analogue to digital conversions were achieved with a TiePie Handyscope dual channel oscilloscope carrying an arbitrary signal generator (type HS5-540, TiePie Engineering, Sneek, the Netherlands). The transmitted signal was a linear down-chirp spanning the frequencies between 100 kHz to 35 kHz with a duration of 2 ms. The target under test consisted of two discrete point scatterers delayed of $\tau = 2d/c$, with d being the spacing between the two scatterers and c the speed of propagation.

Equipment control and data processing were performed in Matlab (release 2015a, MathWorks, Natick Mass., USA).

5.1.2 Simulations

The received signal (or "echo"), $x_E(t)$ was generated by summing two time delayed versions of the call waveform $x_C(t)$:

$$x_E(t) = x_C(t - t_1) + x_C(t - t_1 - \tau) \tag{5.1}$$

5.1.3 Phantom targets

Echoes of phantom targets were generated with the loudspeaker located at 1.886 m from the microphone. Two scatterers were reproduced by emitting the call and a replica of the call delayed of τ:

$$x_{Phantom}(t) = x_C(t) + x_C(t-\tau) \tag{5.2}$$

The relative position of the reflecting points was varied by using different values for the delay $\tau = [0, 2, 4, ..., 50]$ μs, corresponding to a separation $d = [0, 0.34, 0.68, ..., 8.5]$ mm. Another set of measurements was done with the speaker located at 1.272 m from the microphone and with delays $\tau = [5, 10, 15, 20, 25, 50, 100]$ μs, corresponding to separations of [0.85, 1.7, 2.55, 3.4, 4.25, 8.5, 17] mm.

Phantom targets were used to study ideal point targets in a real environment, accounting for the effect of air attenuation, noise and transmitter/receiver imperfections.

5.1.4 Physical targets

The target representing two closely spaced reflectors was physically realized using two vertical rods fixed on a turntable (LT360EX, LinearX Systems, Battle Ground, WA, USA, Fig. 5.1, 5.2). Each rod had diameter 6 mm and length 0.75 m. The relative position of reflecting surfaces was varied by changing the turntable angle with a predefined step of 0.5 degrees. One of the rods was fixed in the center of the turntable. The other was at $r = 0.025$ m from the center.

The speaker and the microphone were arranged vertically at a height of approximately 0.3 m above the level of the turntable surface. The precise distance between the targets and the sensors was estimated by curve fitting over multiple measurements at each turntable

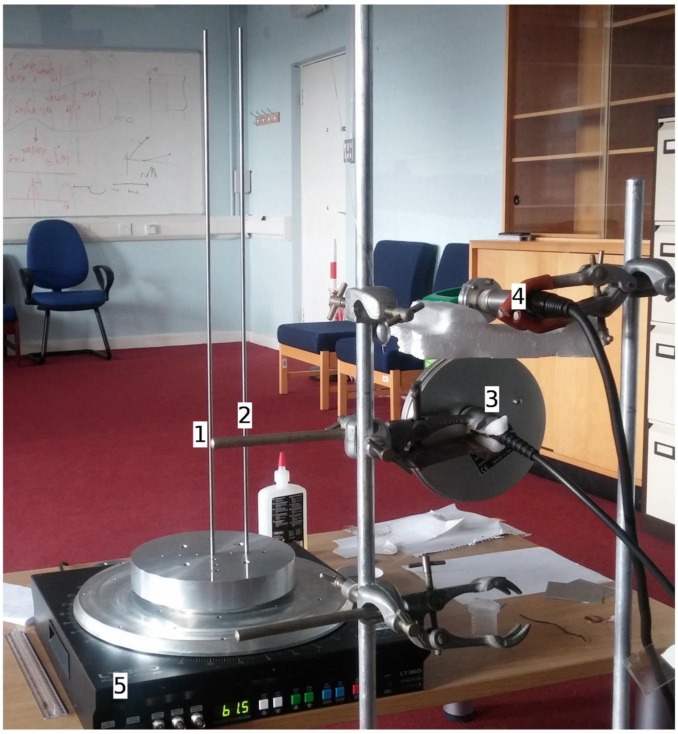

Figure 5.1: Ultrasound experimental set up – two vertical rods on a turntable: 1 – central rod; 2 – peripheral rod; 3 – ultrasound speaker; 4 – ultrasound microphne; 5 – turntable

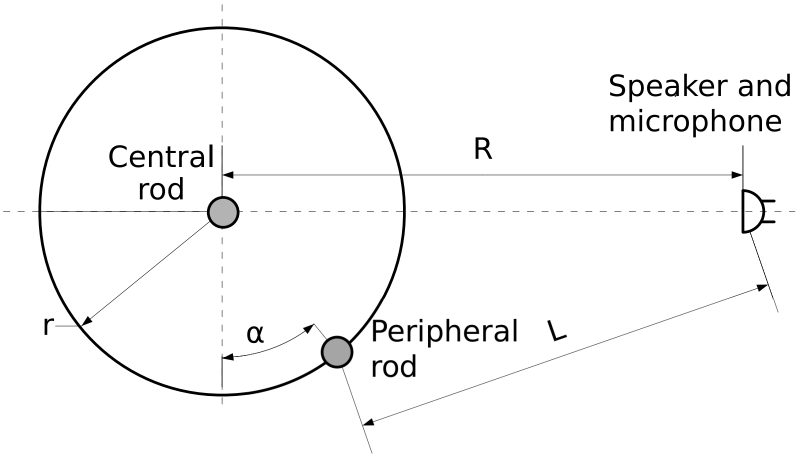

Figure 5.2: Ultrasound experimental set up diagram

position (see Appendix A where the accuracy of the ground truth is also assessed). For the central rod it was $R = 0.943$ m.

5.2 Equivalence demonstration between SCAT and its baseband version

Computer simulations and phantom target measurements have both been performed using a set of targets with the same parameters. All experimental measurements were preprocessed by removing the mean value. The inputs to BSCT were first convolved with a Hilbert filter to create complex values from the real data values and then converted to baseband by multiplying with the carrier. Figure 4.1 shows the real component of the resulting baseband signal.

Both SCAT and BSCT were implemented in Matlab (release 2015a, MathWorks, Natick Mass., USA) as banks of filters. A linear frequency spacing of the filters in the bandpass filter bank was used to allow processing of a linear chirp. The filter bank contained 65 bandpass filters with linear frequency spacing from -32 to 32 kHz for BSCT and from 35.5 to 99.5 kHz for SCAT (1 kHz increments). All other parameters followed the ones described in Sec. 3.6 after [13]. Two versions of the SCAT differing in the level of smoothing were considered labelled SCAT-L for low smoothing and SCAT-H for high smoothing (Sec. 3.6). The smoothing in the BSCT is inherent as the magnitude of the complex envelope of the signal was used (Sec. 4.1). Finally the output of the spectral block for each model was calculated by passing the call and echo signals through the model and normalising by dividing by the maximum value of each output.

The spectral output of the proposed BSCT is compared with the output of both versions of the original SCAT (with low and high smoothing) for different delays between the scatterers. The difference is measured by using the root mean square (RMS) error:

$$\text{error} = \sqrt{\frac{1}{M}\sum_{i=1}^{M}(E_{SCAT}[f_i] - E_{BSCT}[f_i])^2} \tag{5.3}$$

where E_{SCAT} and E_{BSCT} are the normalised outputs of the models compared and $M = 65$ is the number of filters.

The results of the comparison expressed as RMS error in % of maximal value are presented in Table 5.1 for all datasets. Results show the error is less than 1% for delays below 50 μs and less than 5% up to 100 μs. There is no trend in the error with the delay for small fine delays (Fig. 5.3). Fig. 5.4 displays the full outputs of BSCT and SCAT expressed as a function of the frequency for the case of two simulated targets delayed by 20 μs. It can be seen that the level of smoothing in the original SCAT does not influence the spectral output. The same is valid for the baseband model which gives practically the same results.

In the real measurements, the influence of the air and non-perfect microphone and speaker characteristics modify the target response. The outputs of BSCT for simulated

Table 5.1: Difference between proposed BSCT and original SCAT with high (SCAT-H) and low (SCAT-L) smoothing, expessed as RMS, %

Delay	Simulations, %		Experiments, %	
μs	SCAT-H	SCAT-L	SCAT-H	SCAT-L
5	0.20	0.19	0.78	0.81
10	0.54	0.68	0.39	0.42
15	0.34	0.34	0.38	0.39
20	0.67	0.52	0.60	0.59
25	0.41	0.39	0.57	0.55
50	0.94	0.98	0.85	0.90
100	4.4	4.6	2.1	2.1

Table 5.2: Root mean squared difference between simulations and experiments processed with BSCT

Delay	μs	5	10	15	20	25	50	100
Error	%	12.3	13.9	16.4	15.1	15.0	20.8	17.4

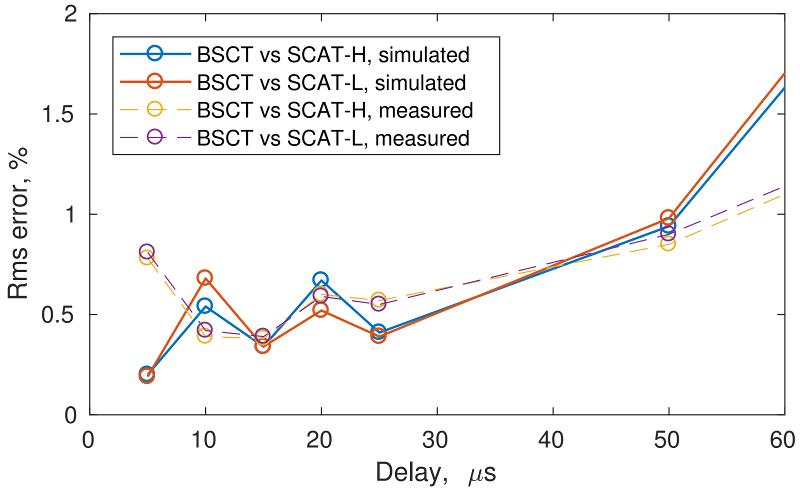

Figure 5.3: RMS difference between BSCT and SCAT spectral output

and phantom targets are compared in Table 5.2 and shown in Fig. 5.5. The real experiments introduce significant deformation of the target spectrum relative to the simulations – difference above 10%. This shows that although the real data behaves in a way which is not identical to the simulated data – as would be expected, the two algorithms are stable to the imperfections in the data and both still behave in a similar manner.

Looking more closely to the interference patterns for different relative positions between the scatterers (Fig. 5.6) it can be seen that the general shape and, in particular, the locations of the zeroes, are preserved between the experiments and the simulations. These features are likely to be significant for any scheme for resolving the close-spaced targets and this result indicates that the new algorithm, like the SCAT algorithm, retains the information which will later be needed to resolve the targets.

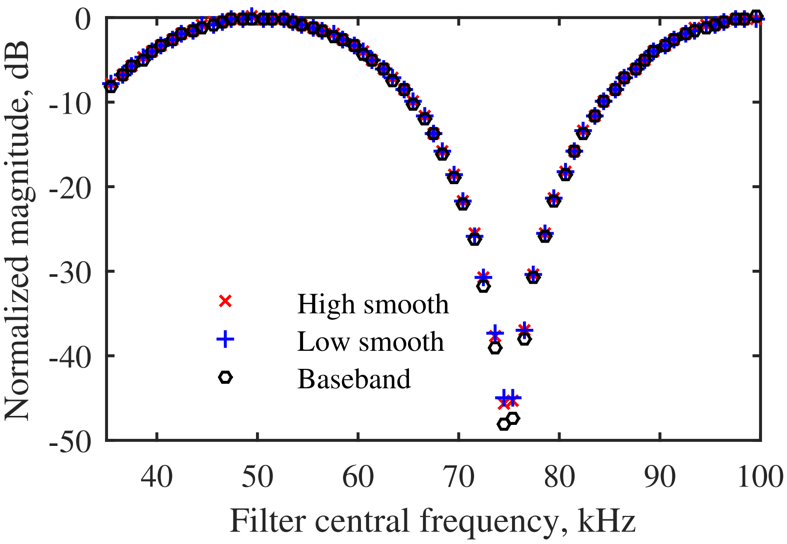

Figure 5.4: Spectral output of BSCT (baseband) and SCAT (high and low smoothing), simulated two targets with separation 3.4 mm (delay 20 μs)

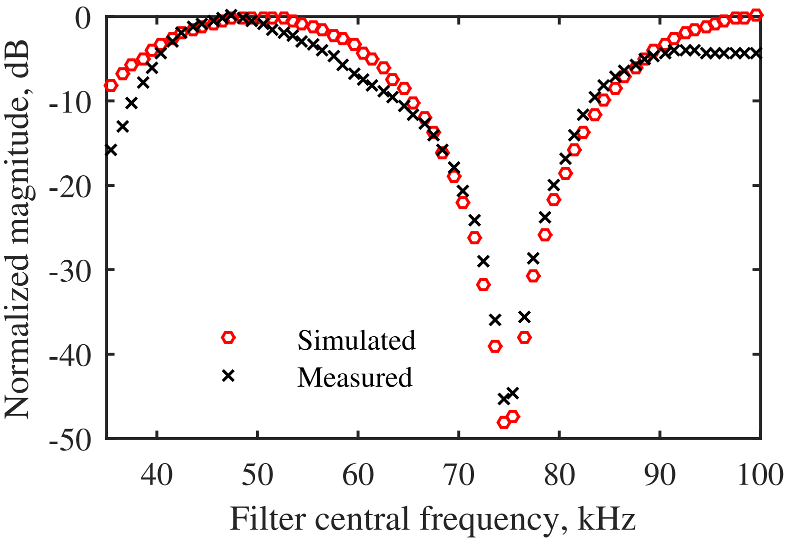

Figure 5.5: Spectral output of BSCT model, simulated vs measured two targets separated by 3.4 mm (delay 20 μs)

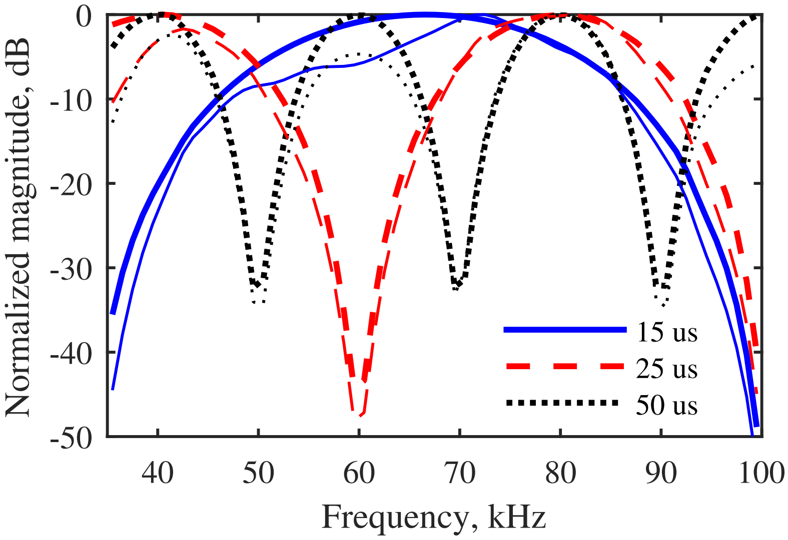

Figure 5.6: Spectral output of BSCT model for two targets for delays 15 μs, 25 μs and 50 μs. Simulated (thick lines) and measured (thin lines) input signals

Results show that proposed baseband spectrogram transformation model gives an output comparable with the output of the original spectrogram correlation and transformation receiver. This implies that

- processing of target echoes with a receiver based on the bat auditory system can be applied to signals that are centred on very high carrier frequencies, such as radar signals.

- the output of the spectral block does not depend on the phase information of the carrier signal and is a form of non-coherent signal processing; the spectral block will be more robust to loss of signal coherence than the matched filter.

- advanced signal analysis techniques based on complex signal representation could be used for further understanding of the model.

5.3 Evaluation of BSCT resolution capabilities

In this section, the outputs of the BSCT and of the matched filter are compared in order to assess their relative range resolution performance. All experimental measurements were preprocessed by removing the mean value and converted to baseband

The BSCT frequency profile, describing the energy of the output of each filter of the BSCT, was calculated as follows:

1. matched filter the echo $x_E(t)$ with the emitted signal $x_C(t)$ to obtain the matched filter output profile $x_M(t)$ (4.23);
2. calculate the energy spectrum by fast Fourier transform (FFT) of $x_M(t)$ and multiplying by its complex conjugate
3. average the spectrum over a bandwidth $B = 4$ kHz for $K = 65$ central frequencies linearly spaced between −32 and 32 kHz (step of 1 kHz) – obtain the result for $E_M[i]$ numerically (4.24)
4. equalize the spectrum based on the spectrum of the emitted chirp or other predefined spectrum E_{ref}, e.g. the spectrum of a return from single scatterer

$$E_M[i] = \frac{E_M[i]}{E_{ref}[i]} \tag{5.4}$$

An example of the BSCT frequency profiles as a function of the time delay τ is shown in Fig. 5.7 for simulated and real targets.

The output of the BSCT representing the delay profile was calculated as follows:

1. remove the average of the spectrum – implement (4.19)

$$E_{M'}[i] = E_M[i] - \frac{1}{K}\sum_{i=1}^{K} E_M[i] \tag{5.5}$$

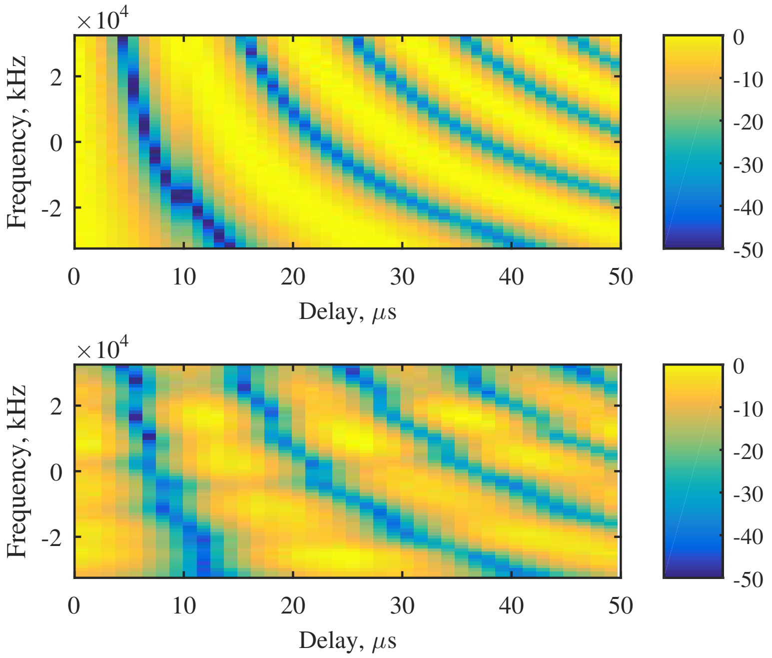

Figure 5.7: BSCT frequency profiles for simulated data (top) and real measurements (bottom) equalized by the emitted call frequency profile. The colour encodes the energy in dB

2. inverse transform $E_{M'}[i]$ using inverse FFT to get the fine delay profile – implement (4.18) numerically; zero-padding can be applied before the IFFT by adding a sequence of N zeros to achieve a suitable sampling rate:

$$f_s = \frac{NB_C}{K} \tag{5.6}$$

The output was finally normalised by the total energy of the signal and displayed in a dB scale.

Figure 5.8a displays the fine delay profiles generated by the model for different spacings between the simulated scatterers. Unlike the matched filter output, these profiles encode directly the spacing between the scatterers and not the absolute range of the target. As the representation is symmetrical, there is a second peak at negative delays but this peak interferes less than the second peak produced by the matched filter because the separation is double. Because the bandwidth of the chirp was 65 kHz the nominal resolution was 15 μs. It can be seen that the second scatterer can be resolved at delays below 10 μs. The delay profiles based on the matched filter output are shown in Fig. 5.8b. The lobes of the scatterers merge for spacings below 20 μs demonstrating that, for ideal reflectors and an ideal environment, the range resolution is improved by a factor of two.

The BSCT point estimate of the relative time spacing was calculated from the BSCT delay profile as the position of the maximal profile peak (denoted further as BST). The MF estimate was the distance between the two highest peaks in the matched filter output. In addition, a sinusoidal curve was fitted to the BSCT frequency profile using a Non-linear Least Square method (NLS) with the "Thrust-Region" algorithm and optimized starting point [102, pp.4-46–4-56].

The results are summarized in Table 5.3 and Fig. 5.9a where the estimates of the delay between the scatterers based on the BSCT peaks (BST), matched filter (MF) and non-linear curve fitting (NLS) approaches are presented together with the true delays. The resolution capability of the matched filter for the bandwidth available is 20 μs as already observed. The spectrogram transformation delay profile based approach gives a range resolution down to 10 μs and can indicate the presence of the second scatterer down to 4 μs delay separation. The NLS results are comparable to those of the BSCT.

If the frequency response of a single scatterer is known (e.g can be measured or calculated from the transmitter and receiver frequency responses and the air attenuation at the frequencies and the range of interest) then the spectrum can be equalized. This compensation of the expected chirp spectrum improves the resolution accuracy. The improvements is significant for the NLS estimation down to 2 μs, e.g. from Table 5.3 it can be read that for true delay 4 μs the estimate without equalization is 8.8 μs (column NLS) and with equalization is 4.4 μs (column NLSb). The changes in the BST performance are minor

Table 5.3: Fine delay estimates on simulated targets

Delay	Delay estimation approach				
μs	MF	BST	NLS	BSTb	NLSb
0.0	0.0	—	93.7	—	7.8
2.0	0.0	—	0.0	10.3	3.0
4.0	0.0	10.6	8.8	10.3	4.4
6.0	0.0	11.2	10.1	10.9	6.3
8.0	20.0	16.0	13.3	15.2	8.6
10.0	0.0	11.2	11.5	11.0	9.9
12.0	0.0	11.7	12.4	11.4	11.8
14.0	0.0	16.5	13.7	16.6	14.0
16.0	0.0	16.7	15.6	16.8	15.9
18.0	0.0	15.7	17.4	16.5	17.8
20.0	22.0	20.3	20.3	19.7	19.8
22.0	22.0	21.0	22.7	19.8	21.6
26.0	26.0	26.9	27.1	26.2	25.9
30.0	34.0	32.5	31.3	31.2	29.9

b – denotes equalized spectrum

— the algorithm failed to work

(compare columns BST and BSTb from Table 5.3 or Fig. 5.9a and Fig. 5.10a). The results relative to the phantom echoes in Fig. 5.9b and Fig. 5.10b show that the range resolution are compatible with the simulations.

The results relative to the experiments with the two vertical rods on the turntable are shown in Fig. 5.11. These confirm that the BSCT provides reliable range resolution down to 10 μs, that is two times better than the matched filter resolution of 20 μs (Fig. 5.9c and Fig. 5.10c). For the real data, the NLS approach does not perform much better and although it improves with equalization, the improvements are minor. The BSCT is capable of handling two non-perfect point scatterers as well as the more computationally expensive non-linear least-square parameter estimation approach.

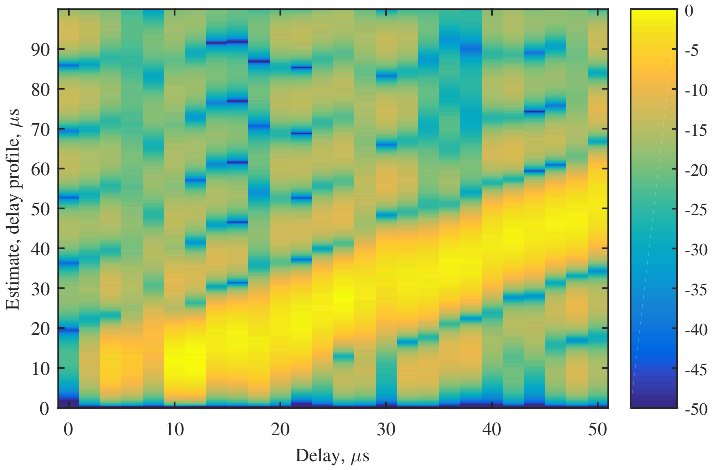

(a) Baseband spectrogram transformation output, dB

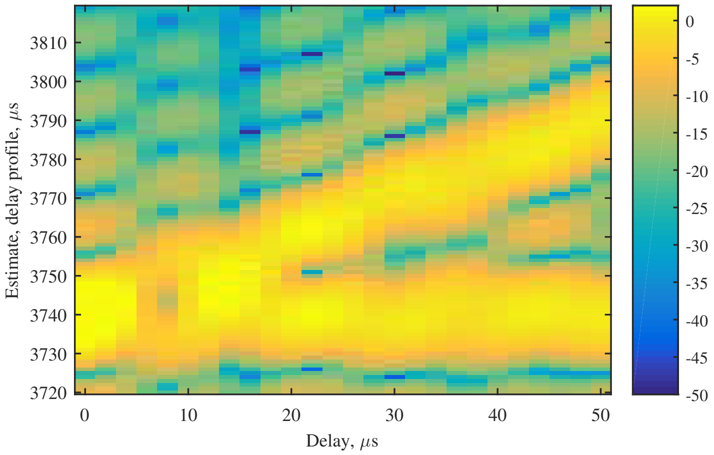

(b) Matched filter output, dB

Figure 5.8: Fine delay profiles as a function of the delay between the scatterers, simulated data. Signal bandwidth is 65 kHz. In the spectrogram transformation based approach the profile encodes the spacing between the scatterers. The matched filter gives the absolute position of the scatteres.

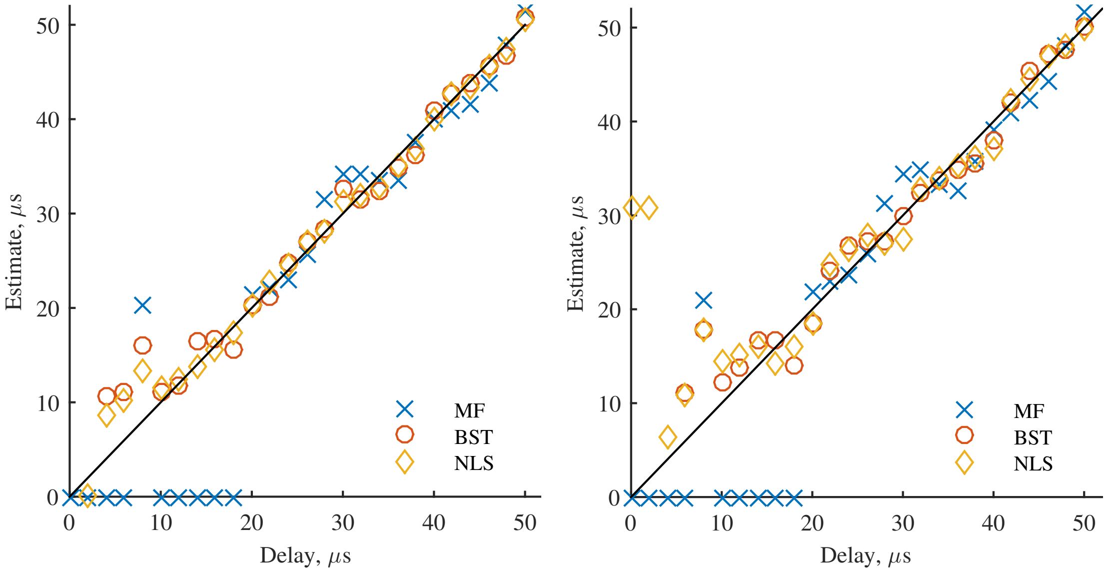

(a) Simulated target (b) Phantom target

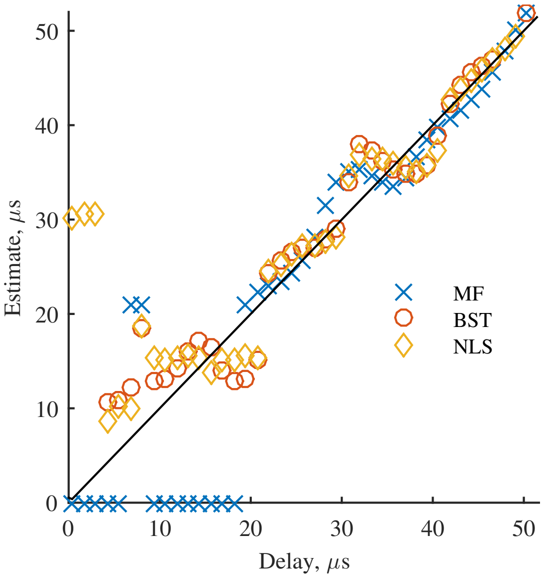

(c) Physical target

Figure 5.9: Estimated delay as a function of the delay between the scatterers. The signal is linear chirp with bandwidth 65 kHz and duration 2 ms. The delay between the scatterers is estimated using matched filter (MF), baseband spectrogram transformation (BST) or non-linear least square fitting (NLS). The phantom target is created by a speaker emitting two delayed chirps towards a microphone located at 1.886 m. The physical target consists of two vertical rods on a turntable

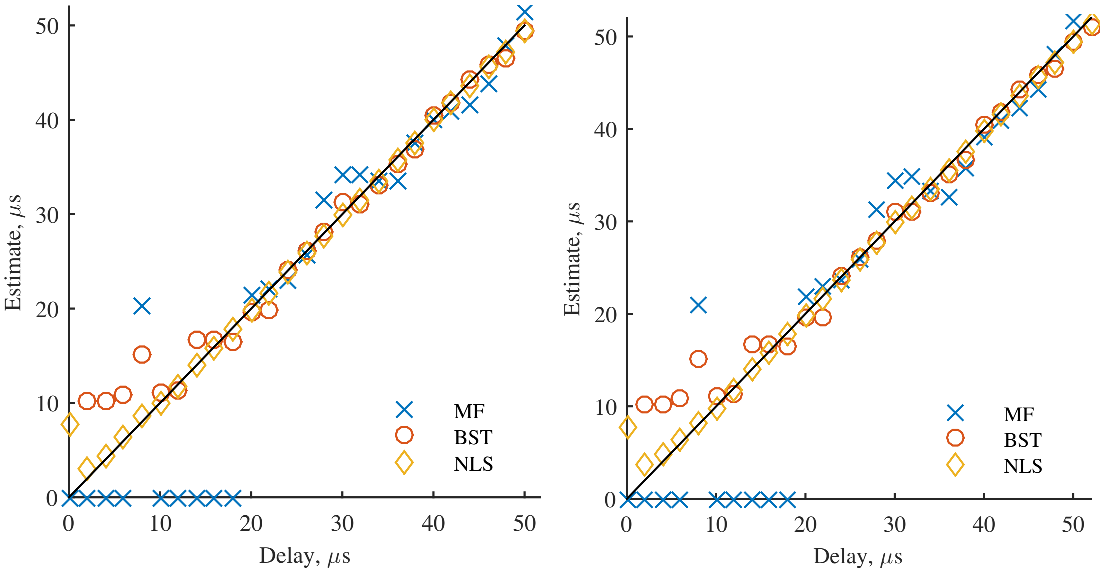

(a) Simulated target (b) Phantom target

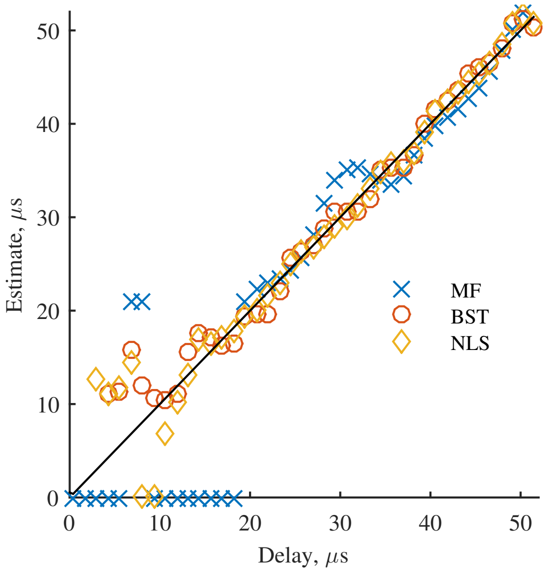

(c) Physical target

Figure 5.10: The same as Fig. 5.9 but the signal spectrum is equalized by the single scatterer spectrum

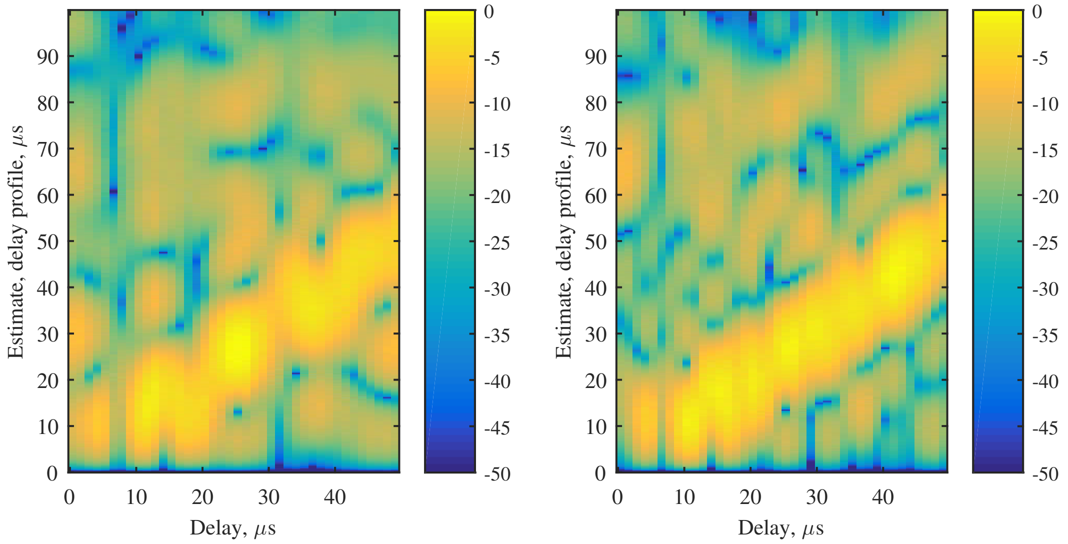

(a) baseband spectrogram transformation output

(b) baseband spectrogram transformation equalized output

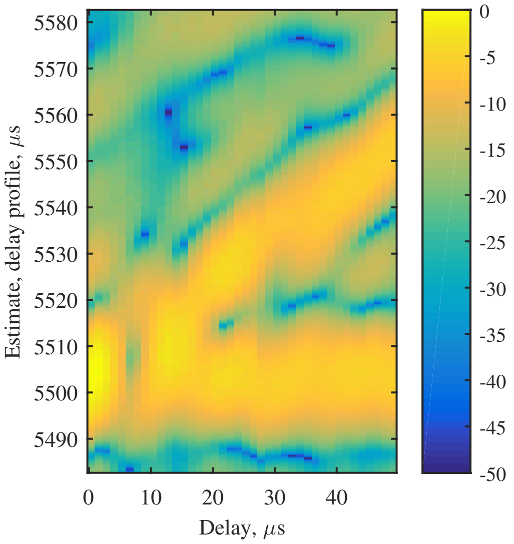

(c) Matched filter output

Figure 5.11: Fine delay profiles as a function of the delay between the scatterers. Data for real target. Signal bandwidth is 65 kHz

5.4 Summary

Ultrasound echoes from two close targets were collected artificially through simulations and experimentally using phantom end real target measurements. The spectral outputs of the SCAT and the BSCT receivers were examined qualitatively and compared quantitatively to show their equivalence. Simulated and experimental results were also compared to show that the zero locations in the spectral interference patterns are robust to real measurements and are likely to provide features important for resolving close spaced targets. The delay profiles and delay estimates based on BSCT and MF were calculated, visualised and compared. It was confirmed that BSCT provides 1.5–2 times better resolution than MF.

Chapter 6

Application of the BSCT model at radio frequencies

The goal of this chapter is to demonstrate how biologically inspired signal processing can be applied to radar frequency signals and to validate the expected performance with different experiment arrangements, physical targets and noise. Real target measurements are processed and analysed in order to better understand the BSCT model output at RF. The main goal of the experiment set-up was to get a realistic picture and better interpretation of model capabilities for practical applications.

6.1 Experimental set up and data collection

Measurements were performed at radio frequency from 13 GHz to 17 GHz using a Vector Network Analyzer (VNA) (MS46322A, Anritsu) and two 5x4 cm horn antennas (12.6-18.0 GHz). The VNA provides a measurement of the frequency response of a target sampled at constant frequency intervals Δ_F by implementing a stepped frequency waveform. High Range Resolution Profiles (HRRPs) were obtained by taking an Inverse Fast

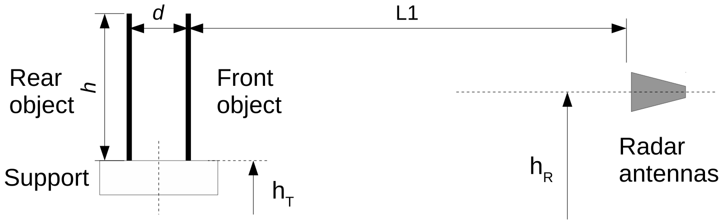

Figure 6.1: RF measurements diagram

Fourier Transform (IFFT) of the output data. The use of the VNA allowed us to vary the range resolution of the data, as desired, by processing different sub-bands within the available 4 GHz bandwidth.

Two point scatterer targets were physically realised using pairs of flat plates, vertical rods and spheres. A simplified diagram for the experiment arrangement is shown in Fig. 6.1. The radial distance d between the flat plates was kept constant. The rods and the spheres were placed on a turntable which allowed the spacing between the scatterers to be varied between 0 and 0.150 m. The distance between the antennas and the targets $L1$ was about 3 m. The measurement noise was manipulated through the Intermediate Frequency Band-Width (IFBW) parameter of the VNA.

Photos of the plates arrangement are shown in Fig. 6.2. The front plate was $0.12 \times 0.12 \times 0.0015$ m and the rear plate was $0.22 \times 0.22 \times 0.0008$ m. The plates were facing the transmitting and receiving antennas with an aspect angle that provided approximately equal Radar Cross Sections (RCS). Both the targets and the antennas were placed 1.1 m above the floor level ($h_R = h_T + h/2 = 1.1$). Two different support structures were tried, separate detached RF transparent columns (Fig. 6.2a) and a shared table (Fig. 6.2b). Most of the experiments were performed with a separations between the plates $d = 0.12$ m and a few with $d = 0.29$ m. Very good signal to noise and signal to clutter was expected considering the big radar cross section (RCS) of a plate with dimensions $w = h = 0.12$ m, $\sigma = 4\pi w^2 h^2/\lambda^2 \approx +8$ dBm^2.

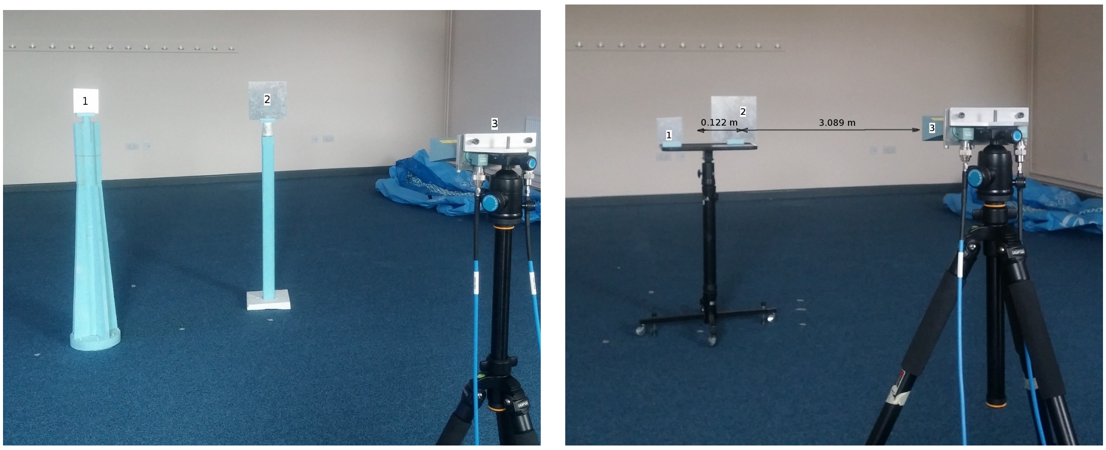

(a) (b)

Figure 6.2: Two flat plates as a target: front plate – 1; rear plate – 2; radar antennas – 3

The two vertical rods used in the experiments were with a diameter of 0.006 m and length h of 0.75 m. These were placed on the two sides of a turntable (LT360EX, LinearX Systems, Battle Ground, WA, USA) at a distance of 0.075 m from the centre of rotation (Fig. 6.3). Therefore the relative distance between the rods with respect to the antennas was $d = 2 \cdot 0.075 \cdot \cos\alpha$, where α is the angular position. It was changed by rotating the turntable with a step of 1 degree. Three different positions of the antennas relative to the rod height were tried in order to achieve simple scattering behaviour (one scatterer per rod). Initially the transmitting and receiving antennas were positioned at a level just below and just above the tip of the rod (Fig. 6.3a and Fig. A.13a) and at a distance of 2 m and 3 m respectively. Then they were moved to a level approximately 0.04 m above the turntable surface (Fig. 6.3b and Fig. A.13b) at 3 m. A close photos of the rods is shown in Fig.6.3c. An estimate of the RCS for cylinder is given by $\sigma = \pi d h^2/\lambda = -3$ dBm^2 for aspect angle 90° but assuming minor deviation from this elevation angle gives a more realistic -15 dBm^2 at 90.1 deg aspect angle [103, Sec. 14.4].

The spheres diameters were 0.018 m and 0.020 m. The experiment arrangements were analogue to the rods experiment with antennas at 0.04 m above the turntable support

(a) Initial arrangement, Ex. 0 and 6

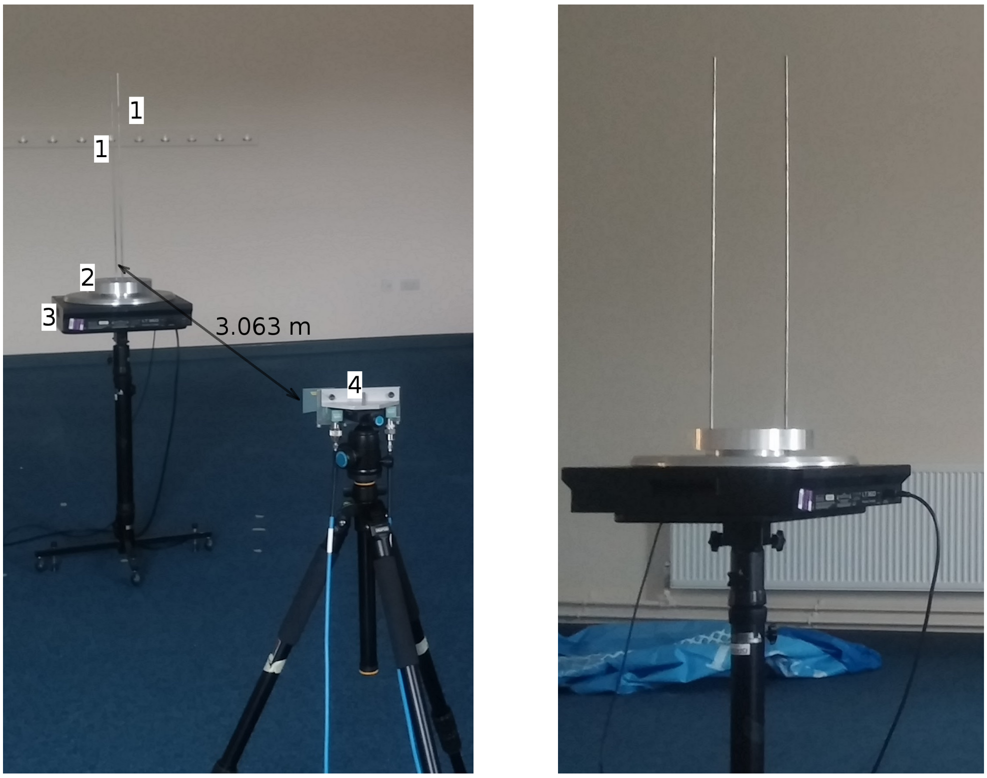

(b) Final arrangement, Ex. 8

(c) Close view

Figure 6.3: Two rods on a turntable: 1 – vertical rod; 2 – support plate; 3 – turntable; 4 – radar antennas

(a) (b)

Figure 6.4: Two spheres on a turntable

level (Fig. 6.4). Four sets of measurements were performed at different noise level. It was varied by setting the IFBW parameter of the VNA to 2, 10, 100 and 300 kHz. This corresponds to change of the noise floor with −17, −10, 0 and 4.8 dB respectively. The spheres were the targets with the smallest radar cross section, $\sigma \approx \pi r^2 = -36$ dBm^2. As the clutter suppression processing was not changed, the smallest signal to clutter ratio could be expected. It should be noted also that no attempt was made to separate the spheres from the support surface – they were just fixed into a grooves directly on the support plate.

Each experiment involved multiple measurements of the background, a single object and two objects. Single reflector measurements were used to evaluate the frequency response of the "point" scatterer realised with the corresponding object. The background measurements were used to enable background (clutter) removal and to evaluate the location of the strongest background scatterers. Multiple measurements with the same setup allowed accurate noise level calculation and noise reduction through averaging. Determining the true range to each target was not always trivial as the phase centre of a real object and the antennas phase centres are not known exactly. For the two targets on a turntable cases the position of the centre of the turntable was measured using single target and RF target detection and ranging and then the true target positions for each angle was calculated. For the flat plates RF target detection and ranging was used for each plate separately. This way the interference between the targets does not affect the measurement of the ground true.

During the mounting/dismounting of the vertical rods a disturbance of the whole turntable was introduced leading to limitations of the background removal. Some of the measurements were discarded, e.g. the background removal for a single vertical rod was not possible.

The complete dataset organisation and file formats are documented in Appendix C.2. All parameters of the instruments and the targets for each experiment were saved together with the measurement results. They are summarized in Table C.3. Such dataset can be used for independent verification of our algorithm performance, for studying the performance of different algorithms or as a starting point for more extensive data collection.

Simulated data that mirror the experiments were also generated. The response of the target was generated directly in the frequency domain by calculating the theoretical response of two time-delayed impulses in the band of interest and adding white Gaussian noise. The simulation algorithm is provided in App. B, Listing B.10.

6.2 Algorithm for implementation of BSCT

The basic workflow to apply BSCT to RF measurements is summarized in Fig. 6.5. It is build over the conventional MF processing represented as a first block. Then the target response is separated and the BSCT transformation is applied. The specific calculations are described in more details in the following paragraphs. How more advanced algorithms

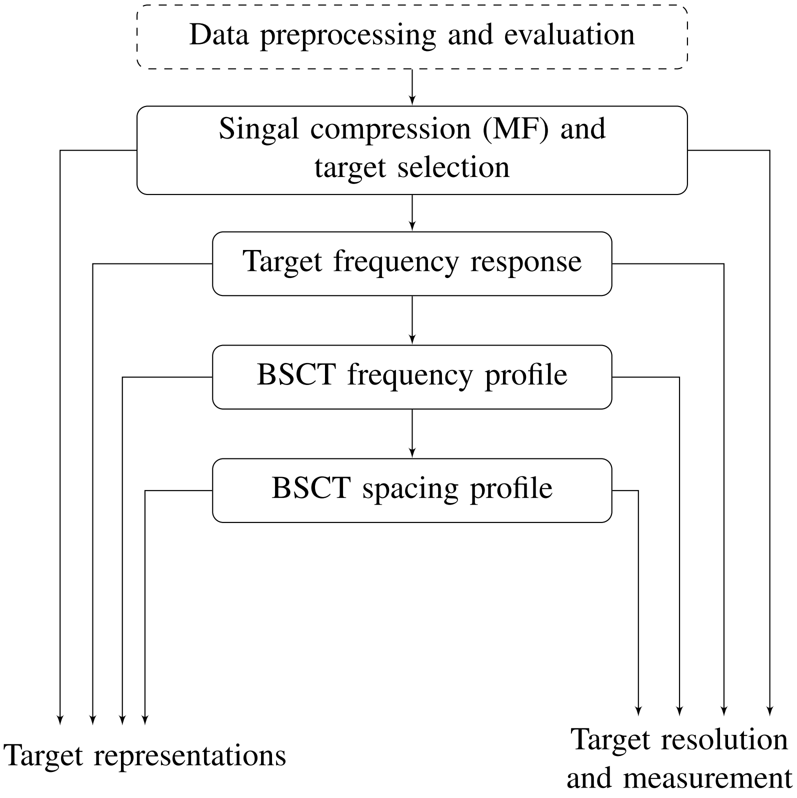

Figure 6.5: BSCT flow-chart

can be integrated is noted where applicable.

A. Data preprocessing and evaluation The application of BSCT is preceded by several steps necessary for noise evaluation, clutter removal, signal compression and target selection. These replace the temporal block of the SCAT.

1. Noise level calculation and noise reduction

   All measurements contain noise. To calculate the noise power P_N, a pure noise signal $W(f)$ was produced by subtracting two measurements of the same scene. The power of $W(f)$ is 3 dB higher than the power of the noise in the raw measurement. Therefore the noise per unit bandwidth is $P_{N0} = 0.5\,\mathrm{var}(W)$, assuming zero mean. The corresponding noise power in the time domain is $P_N = 0.5\,\mathrm{var}(w(t)) = 0.5B_C^2\,\mathrm{var}(\mathcal{F}^{-1}(W))$, where $w(t)$ is the IFFT of $W(f)$, normalised appropriately so the Parseval theorem holds.

The noise level can be reduced by averaging a number K independent measurements of the same scene, $P_{N0} \leftarrow P_{N0}/K$. The measurement noise is also determined by the Intermediate Frequency Band-Width (IFBW) parameter of the VNA. The reduction of the noise power is proportional to the reduction of IFBW, e.g. two times decrease of IFBW leads to 3 dB decrease of P_N.

2. Background characterisation and clutter reduction

   The raw measurement preprocessing involves background removal in order to eliminate the clutter. The background is measured separately. The background signal also contains noise which can be reduced by averaging multiple independent background measurements.

   The background is removed by subtracting the background signal from the target measurements. This operation introduces additional noise in the waveform as the noise powers from the measurement and the background are added together. It also assumes that the background is fixed and can be measured separately from the target.

3. High range resolution profile calculation

   The phase modulation of the transmitted spectrum is removed in a correlation processor [104, pp. 92–93]. This is done automatically by the VNA instrument. The range profile is generated simply by inverse Fourier transform of the VNA acquired frequency domain data after zero padding. In order to reduce the interference between the various scatterers responses Rihaczek recommends the spectrum to be weighted [105]. Sidelobe suppression can be achieved with other techniques, e.g. see Blunt [90]. This has not been used in this work.

4. Target detection and measurement

   For single target the peak power $P_S = s(t_1)^2$ of the range profile represents the energy of the signal. The peak position t_1 is the maximum likelihood estimate of the target delay. Therefore the signal-to-noise-ratio ρ can be calculated as

$$\rho_{dB} = 10\log_{10}\left(\frac{P_S}{P_N}\right) = 20\log_{10}[s(t_1)] - 10\log_{10}[\mathrm{var}(w)] \tag{6.1}$$

Our peak detection algorithm used a threshold equal to the mean signal power plus two standard deviations in order to reduce the false alarm rate due to noise (see the implementation in App. B.2, Listing B.3). Another threshold at −10 dB from the peak value was used to suppress the sidelobes. The location of each peak was calculated either directly from the index of the sample having higher value than its neighbours or by interpolation over three samples (Listing B.4).

For two or more close targets the range profile reflects also the interference of the signals. It can be constructive or destructive so the peaks no longer represent the RCS of the separate scatterers. The accuracy of the peak determined target position is no longer a function of the effective bandwidth and SNR only. Still, the objects of interest are identified in the time domain from the range profile by peak detection through threshold crossing. The minimal peak prominence to consider it as a separate peak was 3 dB. This is the criteria for target resolution that was selected for this work.

B. Estimation of target frequency response The spectrum of a single group of close scatterers need to be extracted from the cumulative spectrum of all reflections, e.g. antenna crosstalk, reflections from walls and support structures, other residuals of the background.

1. Application of transform window

   The reflection from the target is insulated by zeroing the range profile outside an interval $[x_1, x_2]$. Setting the boundaries of the transform window can be subject on careful evaluation on its own ([104, Sec. 9.1.3], [105, App. B]). It is critical if there are adjacent scatter responses that need to be excluded from the transformation. The process of selecting or deleting certain objects to study is also called gating in Anritsu publications [106]

2. Forward transform to get the frequency-domain of the target.

   The frequency response of the target is calculated by applying a FFT. If the HRRP profile has been calculated with weighting than the spectrum should be de-weighted at this step to recover the original amplitude patterns.

These steps can be performed directly in the frequency domain by filtering the measured frequency response $X_M(f)$ through band-pass filter with cut-off frequencies $f_c = [x_1, x_2] \cdot \Delta_F$. They can benefit from a superresolution technique as the iterative Papoulis-Gerchberg algorithm for spectrum extrapolation [107, 108]. An implementation and comparison of the frequency magnitudes calculated using different approaches are provided in App. B.3.

The window length corresponds to the limited “integration time” of the SCAT filters, which is fixed. In this work all values outside $x_1 = 2$ m and $x_2 = 4$ m window were truncated. Thus the ratio on the window around the target $(x_2 - x_1)$ and the nominal resolution δ_R was compatible to the integration time over the nominal resolution for the SCAT.

C. The BSCT frequency profile The BSCT frequency profile (4.7) approximates the energy of the output of each filter of the SCAT receiver. It was studied in its analogue form in Sec. 4.2. In order to allow processing of experimental data, BSCT was implemented numerically as follows:

1. calculate the spectral energy by taking the magnitude squared of the target frequency response $E(f_i) = X_M(f_i)X_M^*(f_i)$
2. average the spectrum over small intervals centred on the frequencies of interest. An averaging over $M = 100$ samples for $K = 160$ frequencies linearly spaced in the measurement band (from 13 GHz to 17 GHz) was done. This corresponds to bandpass filter bandwidth $B = M \times \Delta_F = 25$ MHz (in the equivalent filter bank). This step was implemented as a moving average over the spectral energy sequence followed by downsampling.

$$E[k] = \frac{1}{M} \sum_{i=kM-M/2}^{kM+M/2} E(f_{i+M/2}), \qquad k = 0, \ldots, K-1 \tag{6.2}$$

The number of central frequencies K was selected to be of the same order of magnitude as the number of filters in the SCAT. The averaging window (M or B) was selected in a way that the whole available frequency information is used without overlaps.

D. The BSCT spacing profile This part of the algorithm presents the main "discovery" of "radar" significance to have emerged from the work looking at bat's signal processing from a radar point of view. It was shown that by removing the signal power which is present in all the frequency bins, the variations can then give us the target separation.

1. modify the frequency profile $E[k]$ by subtracting its average E_{avg}

$$E[k] = E[k] - E_{\text{avg}} \qquad E_{\text{avg}} = \frac{1}{K}\sum_{i=0}^{K-1} E[i] \tag{6.3}$$

2. zero-pad to achieve an appropriate time (range) sampling intervals Δ_T ($\Delta_R = c\Delta_T/2$).

$$N_{\text{FFT}} = \frac{K}{B_C \Delta_T} \tag{6.4}$$

3. apply IFFT;

The average of the spectrum E_{avg} is an estimate of the energy of the signal. It can be replaced by an average from multiple measurements at slightly different target separations. Other standard time domain procedures as windowing or filtering can be applied on the frequency profile before the inverse transform. Windowing of the frequency domain sequence can help to reduce the interference between the target peaks. The price is wider and lower lobes as useful information about the spectrum is discarded. Algorithms for estimation of the frequency of the sinusoid in the frequency domain can be applied instead of the IFFT, e.g. MUSIC, NLS.

Target resolution and measurement The spacing between the targets was determined as the location of the highest peak in the BSCT spacing profile. The same peak extraction algorithm as for single target detection and ranging was used (see the implementation in App. B.3).

The peak detection algorithm was applied directly over the compressed signal for comparison. The scatterers were considered resolved if two separate peaks were detected with minimal peak prominence of 3 dB. The spacing was calculated as the distance between the two highest peaks.

6.3 Data preprocessing and exploration analysis

The purpose of the initial data exploration was to check the characteristics of the measurements and select the ones suitable for our study of two close scattering points. All datasets were kept though as they can be useful for more broad studies.

6.3.1 Noise level evaluation

The return signal from the target is calculated by subtracting the background measurement from the target measurement. Therefore the noise power (P_{N0} and P_N in frequency and in time domain correspondingly) is the sum of the noise power from the background measurements and the noise power from the target measurements. The values shown in Tab. 6.1 are calculated without averaging multiple measurements of the background or the target. If multiple measurement averaging is used the noise level P_N from Tab. 6.1 shall be updated to

$$P_{N,avg} = \frac{P_N}{2}(\frac{1}{K_M} + \frac{1}{K_B}) \tag{6.5}$$

where K_M is the number of averaged measurements of the target and K_B is the number of averaged measurements of the background. For example, if $K_M = 1$ and $K_B = 10$, the noise power has to be reduced by 2.6 dB. If $K_M = K_B = 10$, the noise power is 10 dB lower. The number of available measurements for each experiment in the dataset is provided in Tab. C.3. All powers provided by the VNA are not absolute but relative to the transmitted signal.

6.3.2 Background, signal and residual clutter

The range resolution profiles were produced for all sets of measurements. Representative HRRPs for the background measurements, the raw target measurements and the targets

Table 6.1: Noise level, signal power, and SNR

Experiment	IF BW Hz	P_{N0}^{*} dB	$P_{N}^{*,\dagger}$ dB	$P_{B}^{\dagger}$ dB	$P_{S}^{\dagger}$ dB	SNR* dB	Note
Plates, Ex4	100k	-59.3	90.7	102.6	141.2	50.5	Fig. 6.2a
Plates, Ex11	2k	-76.1	73.9	123.8	143.9	70.0	Fig. 6.2b
Rods, Ex8	100k	-59.3	90.7	140.7	121.7	31.1	Fig. 6.3b
Spheres, Ex9D	2k	-76.1	73.9	141.2	110.7	36.8	Fig. 6.4
Spheres, Ex9C	10k	-69.2	80.8	141.2	110.7	29.9	–
Spheres, Ex9	100k	-59.6	90.4	141.2	110.0	19.5	–
Spheres, Ex9B	300k	-55.1	94.9	141.2	110.7	15.8	–

* Based on single background and target measurement

† Signal is scaled by the bandwidth

after background removal are shown in Fig. 6.6. The power levels and the SNR are summarized in Tab. 6.1 (or App. C, Tab. C.4 for all datasets). The power of the background P_B relative to the power of the target measurement gives indication of the importance of the background removal operation. If the background level is 20 dB lower then it can be ignored [109, p. 8]. This was the case with the flat plate measurements (see Fig. 6.6a and 6.6b). Otherwise the background need to be removed and the signal evaluated for residual clutter. This was the case with all turntable related measurements.

The scattering power of the turntable was 20 dB above the power of the rods and 30 dB above the spheres (when positioned 0.04 m below the antennas centreline). Therefore the clutter suppression for the turntable measurements has to be examined. The range profile of the background was compared to the range profile of the target. The HRRP of the rods shown in Fig. 6.6c is clean from background related peaks. In contrast, the HRRP of the rods shown in Fig. 6.6d has a clear peak corresponding to a peak in the background. The clutter in the small sphere measurements is about 15 dB below the target peak. More details about the turntable geometry and its scattering characteristics in the context of the targets used are presented in App. A.2

An example of the HRRPs for two rods on a turntable is shown on Fig. 6.7 as the an-

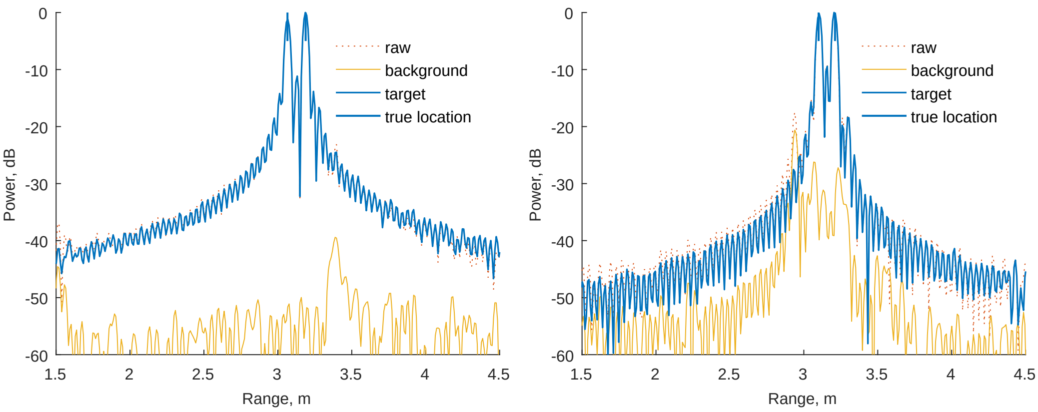

(a) Two flat plates on RF absorbing columns (b) Two flat plates on a support table

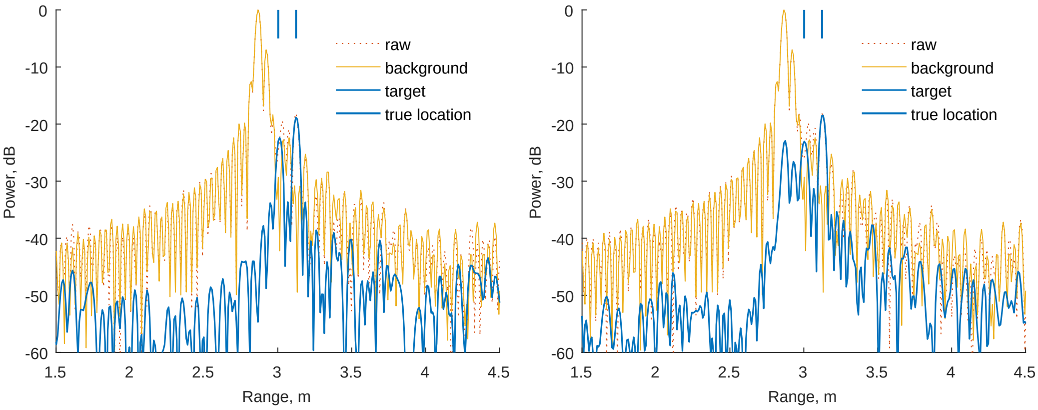

(c) Two vertical rods on a turntable at 36 deg (d) Two vertical rods on a turntable at −36 deg

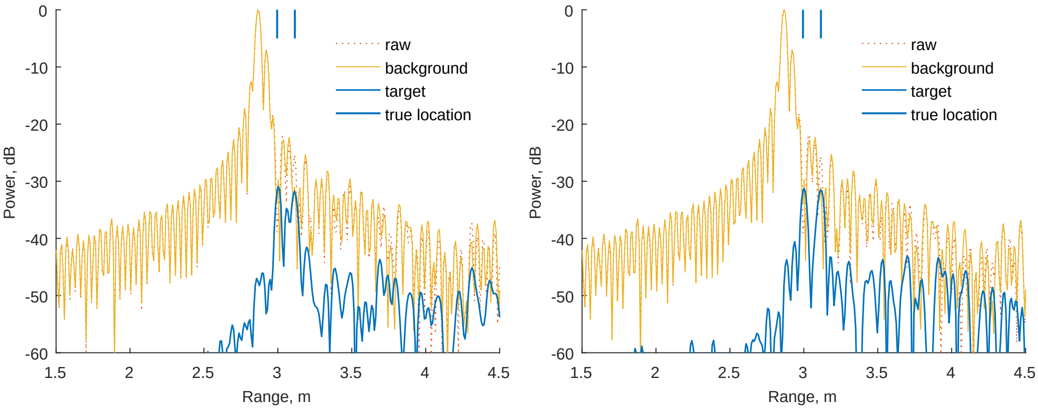

(e) Two small spheres on a turntable at 36 deg (f) Two small spheres on a turntable at −36 deg

Figure 6.6: Background removal evaluation. HRRP of representative measurements of two targets separated by 0.12 m. The background is shown as separate lines. Target HRRP is mixed with residual clutter in cases (d), (e) and (f)

gular position is increased with step 1 deg (experiment Ex8, vertical rods, support surface at the level of the antennas). The true positions of the rods are also shown, calculated for turntable centre at 3.063 m. A zero angular position shift of 0.5° was accounted for when the range and the spacing relative to the radar was calculated.

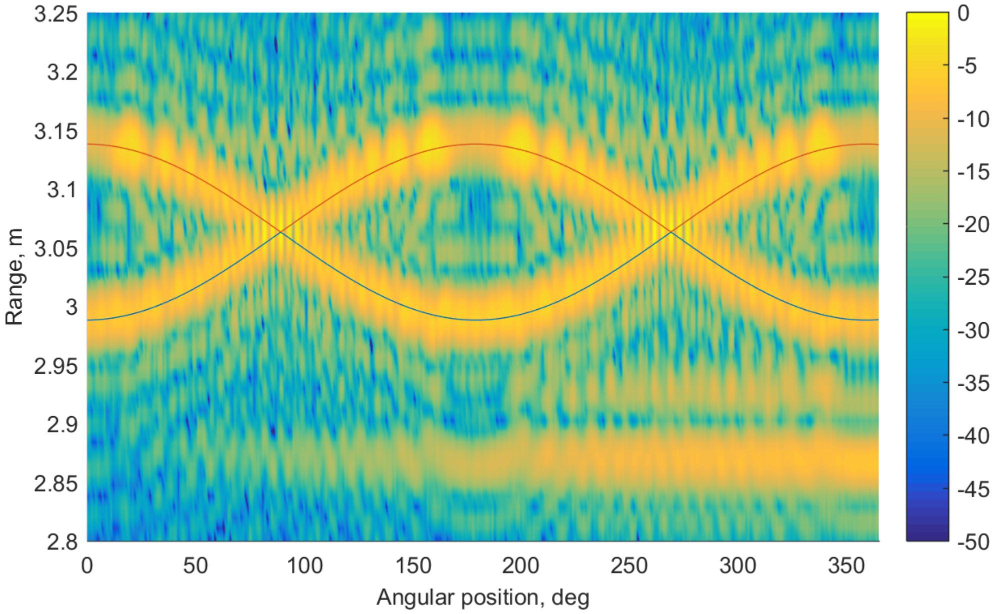

Figure 6.7: Target HRRPs as a function of turntable position for two vertical rods. A fitted curve for the true scatterer ranges is also shown

6.3.3 Backscattering characteristics of the "point targets"

Before trying to resolve two targets, the return of a wideband RF wave from the simple real targets that will be further used was considered. The frequency response of a single flat plate at slightly different positions is presented on Fig. 6.8a. It is not constant and has increasing energy with the frequency as the beam become narrower. The dashed line shows the response of the bigger plate where the concentration of the energy at higher frequencies is even higher. In contrast, reflecting the signal not directly towards the antenna leads to reduction of the return signal power and to attenuation of the higher frequencies.

More than 15 dB reduction of the average power and additional 10 dB reduction for the higher frequencies can be seen on Fig. 6.8b. The spectral energy distribution for a sphere placed on a flat surface is shown on Fig. 6.8c. It is also not flat with about 6 dB variation in power. Presence of residual clutter contamination is to be expected as the turntable scatterers are in the processing window for the target frequency response.

These observations are consistent with the discussion in the literature that real target returns are far from representing ideal point scatterers. The backscattering characteristics of various target features are discussed in [104, Chapter 2] and [110]. The main message is that producing a model of real target return intensities and phases is “at best extremely difficult” [104, pp. 28].

6.3.4 Discussion

Above observations should emphasise the importance of demonstrating model performance with real measurements as opposed to simulations with ideal point scatterers. Model validation can not be considered complete without such evaluation. This will be the subject of the next sections of this thesis.

In addition, a datasets with real measurements of relatively simple targets with known parameters should be of value on its own. It will allow benchmarking of different algorithm, either existing or in development. Detailed specification of our experiments at RF is provided as Appendix.

Comparing BSCT with different enhanced resolution algorithms will be considered a separate task out of the scope of the current research.

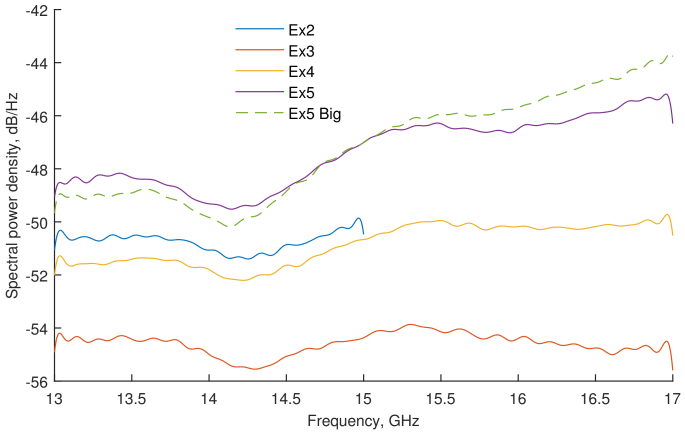

(a) Directed flat plate

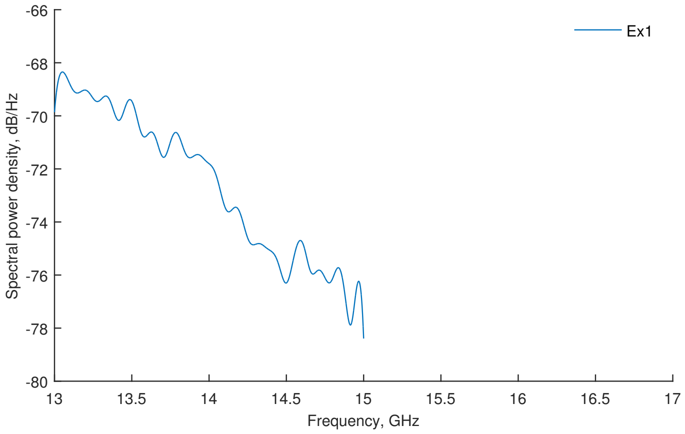

(b) Non-directed flat plate

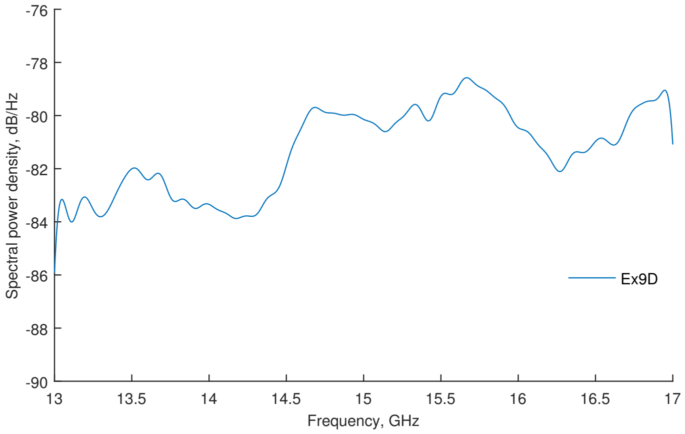

(c) Small sphere

Figure 6.8: Single target power spectral density

6.4 Evaluation of model resolution capabilities

6.4.1 Expressing the range axis in units of resolution gates

Following the approach in [1, pp 92], the term **nominal resolution**, δ_T was defined as the reciprocal of the signal bandwidth (or δ_R when transformed into distance):

$$\delta_T = \frac{1}{B_C} \qquad \delta_R = \frac{c}{2}\delta_T \tag{6.6}$$

The separation between the targets (either in range d or in time τ) can be expressed relative to the nominal resolution, thus measured in resolution gates, and denoted as **normalised spacing** d_g:

$$d_g = \frac{d}{\delta_R} = \frac{\tau}{\delta_T} = \frac{2}{c} \cdot B_C \cdot d \tag{6.7}$$

The normalised spacing is a scaled product of the spacing and the bandwidth. Therefore it is a parameter that embeds information about the bandwidth of the transmitted signal and hence allows to encode the resolution performance with a single parameter. It is convenient to express either the bandwidth or the spacing, e.g. when the other parameter is fixed.

The range or delay axes can also be expressed in resolution gates. This allows unified indexing of time delay, time separation, range and range separation axes in units of resolution gates. For critical sampling (at the Nyquist sampling rate) it is equivalent to the conventional sample index.

$$r_g = \frac{r}{\delta_R} = \frac{t}{\delta_T} = \frac{2}{c} \cdot B_C \cdot r \tag{6.8}$$

The nominal resolution does not guarantee that the matched filter intensity output will have two distinguishable peaks. This is achieved only on average as the minimum separation depends on the phase between the scatterers [105, p. 5].

In the following sections, the BSCT model capability to resolve closely spaced targets was evaluated experimentally by finding the smallest spacing for which the targets were discriminated. This spacing was expressed in nominal resolution gates for easy comparison of different experimental settings. The target range profiles were studied using both the MF and the BSCT for measurements of flat plates, spheres and rods at variable bandwidth or spacing.

6.4.2 Fixed spacing, variable bandwidth experiments

In the two fixed flat plates experiments (e.g. Ex11), the physical separation between the scatterers was fixed to 0.122 m and the bandwidth was gradually reduced. This corresponds to an increase of the size of the resolution gate (6.6) and decrease of the normalised spacing (6.7). The SNR was high (> 60 dB). The bandwidth of the transmitted signal B_C was varied at the processing stage by discarding data and thus reducing the available 4 GHz bandwidth. The spectral magnitudes were scaled appropriately to preserve the power of the signal. A diagram of the power spectrum of the measurement is shown on Fig. 6.9 for all available frequency samples in the (13–17) GHz range. On the same plot two sections of 1 GHz bandwidth each are also marked to show how bandwidth was reduced.

The shape of the BSCT spacing profiles is analysed in more details for three representative cases based on the ratio between the separation and the nominal resolution. The corresponding range profiles are considered also. Scatterers spacing well above the nominal resolution (6.6), e.g. $d_g \geq 2$, for good signal to noise ratio (SNR) leads to range and spacing profiles with strong peaks at the true target positions – see Fig. 6.10a and Fig. 6.10b. The MF range profiles encode the absolute range of the targets and the BSCT spacing profiles encode the spacing between the scatterers. The continuous vertical line marks the true scatterer spacing/range and the dashed line is at the nominal resolution limit. The red circle marks the estimate of the spacing based on the peak location. Another peak close to the resolution limit can be observed. It is not reproduced by simulations with ideal point scatterers at the same SNR (Fig. 6.11a). It reflects the real target and environment properties, i.e. the fine structure inherent in each single target and possibly the residual background clutter. A similar peak is reproduced by simulating targets spaced by 1 cm (Fig. 6.11b). This way fine structure with spacing much less than the nominal resolution is revealed. A similar effect can be observed if the noise level is increased significantly, e.g. Fig 6.11c shows the case when the SNR is reduced from 68 dB to 25 dB.

The interference pattern for scatterer spacing close to the nominal resolution (6.6), e.g. $0.8 < d_g < 1.4$, is shown on Figs. 6.10e, 6.10d. While the peak of the BSCT profile correctly represents the target spacing, the MF range profile have a single peak containing both targets merged together. When $d_g < 0.7$ the spacing profile also fails to give accurate measurement of the spacing (Fig. 6.10f).

To explore the range profiles representing the targets for the whole range of relative

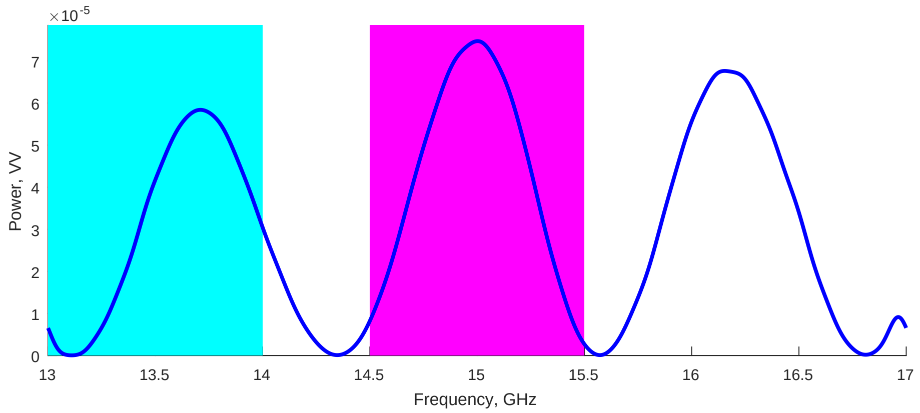

Figure 6.9: Power spectrum as measured for two flat plates separated by 12.2 cm. Lower resolution is achieved by discarding part of the data, e.g. to get 1 GHz bandwidth only the left or only the central part of the signal is used

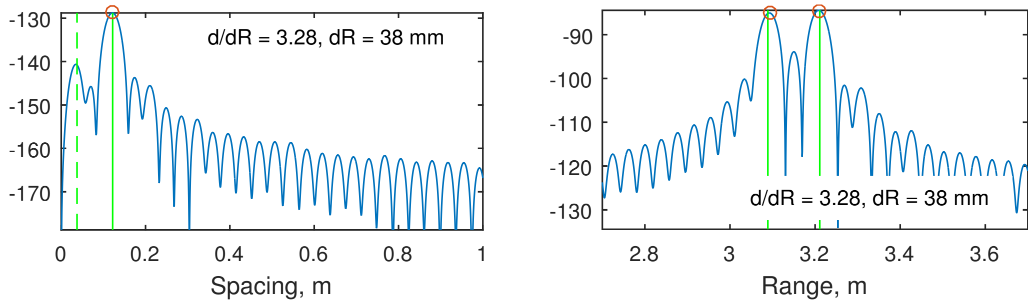

(a) Spacing profile, 4 GHz (b) Range profile, 4 GHz

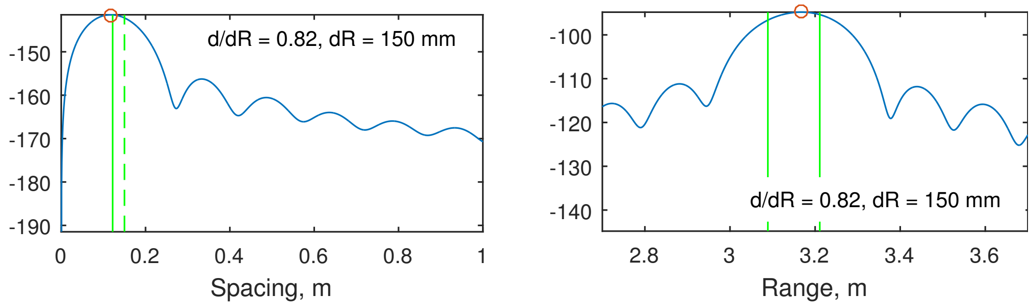

(c) Spacing profile, 1 GHz (d) Range profile, 1 GHz

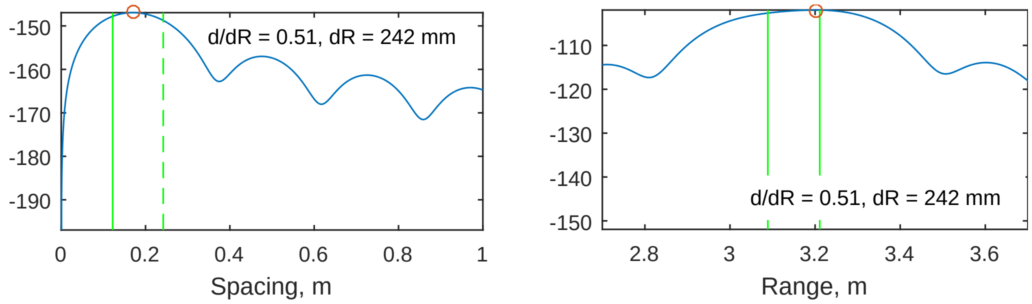

(e) Spacing profile, 0.6 GHz (f) Range profile, 0.6 GHz

Figure 6.10: Target BSCT spacing and MF range profiles for two flat plates separated by 12.2 mm at different signal bandwidths

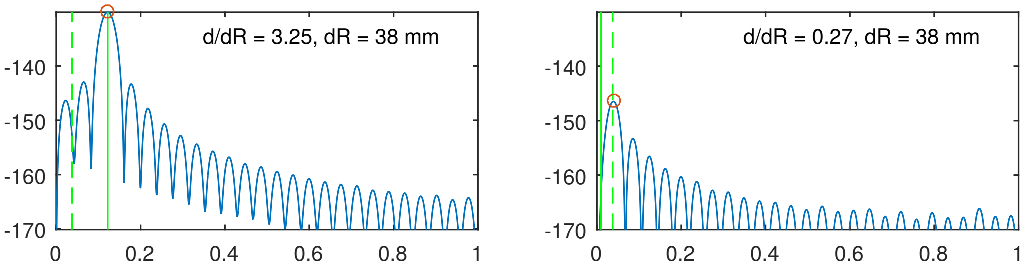

(a) Noise level, 68 dB, d_g = 3.25 (b) Target at 0.3 δ_R

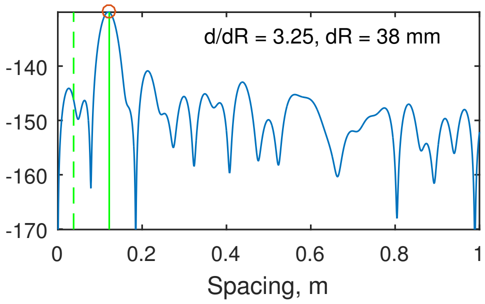

(c) Noise level, 25 dB

Figure 6.11: Spacing profiles from simulated data

spacings, the profile magnitudes were colour coded and the profiles calculated at different bandwidths were presented on the same plot (Fig. 6.12). The x-axis was scaled as normalised spacing instead of bandwidth so that the resolution performance can be observed directly from the graph. The peak locations of the BSCT spacing profiles were marked with circles and provide an estimate of the true separation between the scatterers. The peak locations of the MF range profiles were marked with crosses and provide an estimate of the true range to each scatterer. The minimal bandwidth and the corresponding normalised spacing in resolution gates above which the estimates were representative of the true values is marked with dashed line.

The MF range estimates were further converted to spacing estimates. Both target spacing estimates based on the BSCT and the conventional MF are presented as a function of the normalised spacing d_g in Fig. 6.13. The BSCT target estimates are presented as circles. The MF based estimates if available are marked as crosses. The dotted line is

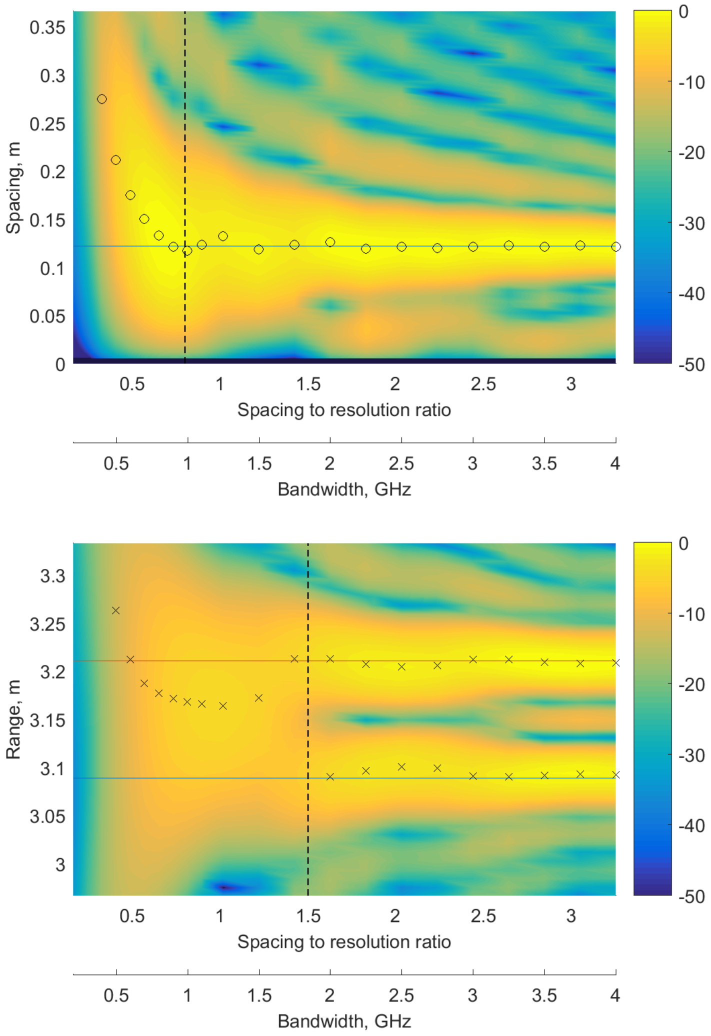

Figure 6.12: Target range resolution profiles as a function of the normalised spacing between the scatterers (spacing divided by the nominal resolution). Two flat plates separated by 12.2 cm experiment. The normalised spacing is varied by changing the bandwidth from 0.2 to 4 GHz. The corresponding nominal resolution also changes. In the spectrogram transformation based approach the profile encodes the spacing between the scatterers. From the matched filter the absolute position of the scatteres is extracted. Each profile main peaks are marked and provide an estimate of the spacing for BSCT and the range for MF. The normalised spacing above which the estimate looks unbiased is denoted by vertical line. It presents an estimate of the functional resolution of the method. The true target range/spacing is shown as continuous horizontal line. BSCT spacing profiles (top), MF range profiles (bottom)

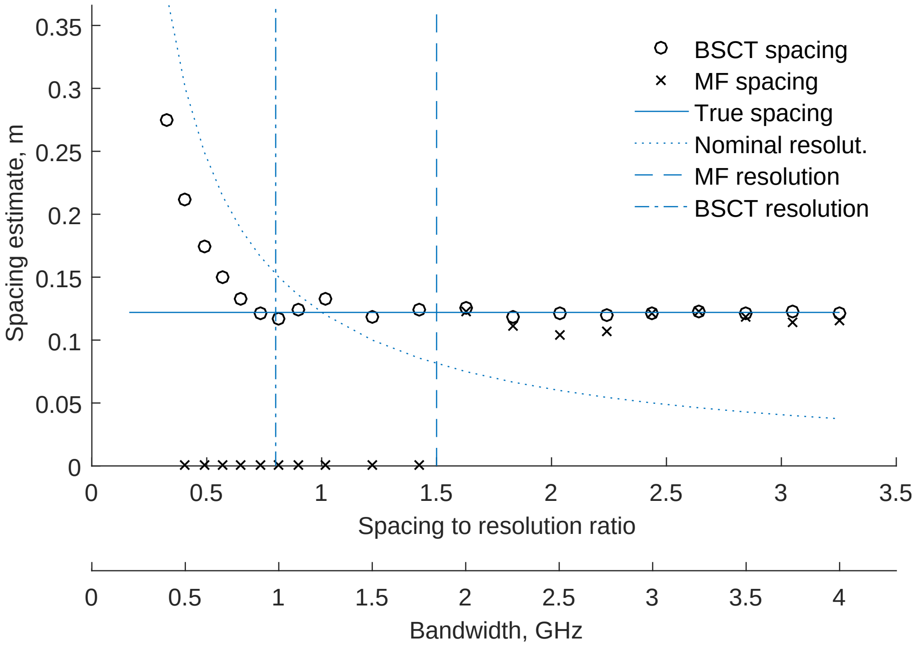

Figure 6.13: BSCT and MF spacing estimates. True target separation is 12.2 mm (shown as continuous horizontal line). The resolution limit is shown as dotted line. The dashed lines are positioned at normalised spacings 0.8 and 1.5. This plot summarize the peak location based estimates from Fig. 6.12

the nominal resolution δ_R (6.6). At low bandwidths the target interaction peak tends to converge to the nominal resolution for BSCT. For the MF case both scatterer peaks merge. It can be seen that targets can be resolved at less than $0.8\delta_R$ for the spacing model (BSCT) and at above $1.5\delta_R$ for the range model (MF) (Figs. 6.12 and 6.13).

6.4.3 Variable spacing, fixed bandwidth experiments

For two objects on a turntable experiments the bandwidth was fixed to 4 GHz and the spacing d was varied from 0 to 0.15 m. This corresponds to variation of the normalised spacing d_g from 0 to 4 resolution gates (6.6). An example measurement of the frequency response of two vertical rods separated by 0.12 m is shown in Fig. 6.14 as a squared magnitude response.

The range and spacing profiles were calculated for different angular positions of the turntable. The results are presented in Fig. 6.15 where the angular position is converted to spacing and normalised spacing. This way the representations for variable bandwidth and for variable spacing can be compared (Fig. 6.12 and Fig. 6.15). The spacing estimates based on both the BSCT and the MF are presented in Fig. 6.16, which is analogue to Fig. 6.13 previously discussed. It can be seen that the functional resolution of the BSCT is approximately 0.8 times the nominal resolution. The corresponding value for the MF is 1.5. Simulated data for ideal targets and similar SNR confirm the observation (Fig. 6.17). The range resolution is improved by nearly a factor of two. The results of the experiment with fixed scatterers is confirmed.

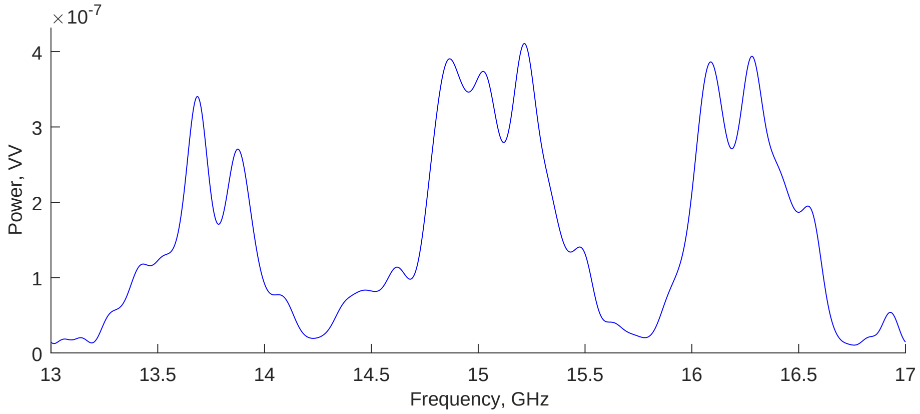

Figure 6.14: Power spectrum measured using VNA for two vertical rods on a turntable. Angular position: 36 deg, radius: 0.075 m, calculated spacing: 0.121 m

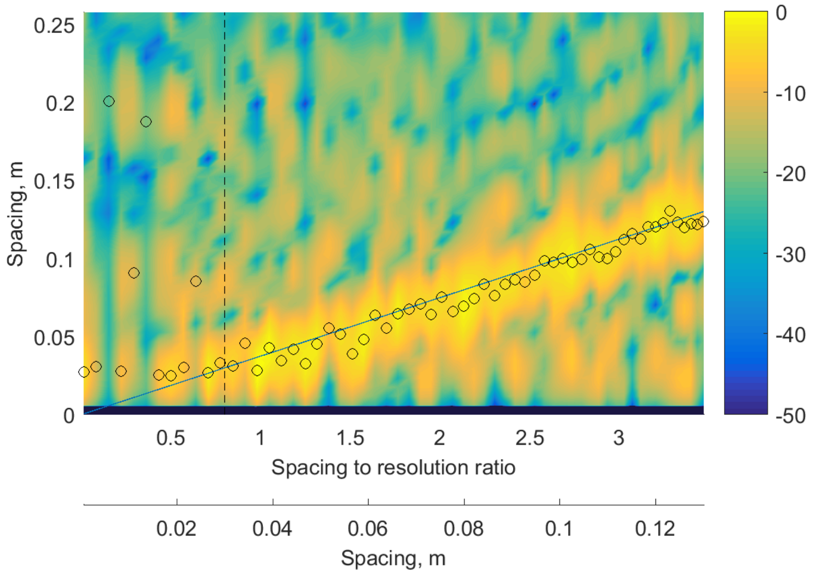

(a) BSCT spacing profiles

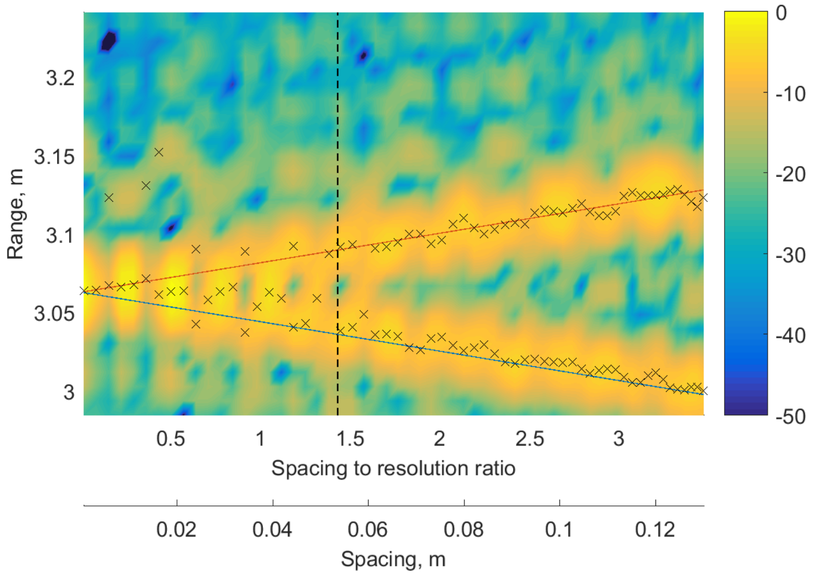

(b) MF range profiles

Figure 6.15: Target range resolution profiles as a function of the normalised spacing between the scatterers (spacing divided by the nominal resolution). Two vertical rods on a turntable experiment. Signal bandwidth is 4 GHz for all measurements. This corresponds to nominal resolution of 0.0375 m. In the spectrogram transformation based approach the profile encodes the spacing between the scatterers. From the matched filter the absolute positions of the scatteres are extracted. Each profile main peaks are marked and provide an estimate of the spacing for BSCT and the range for MF. The relative spacing above which the estimate looks unbiased is denoted by vertical line. It presents an estimate of the functional resolution of the method. The true target range/spacings are shown as continuous lines

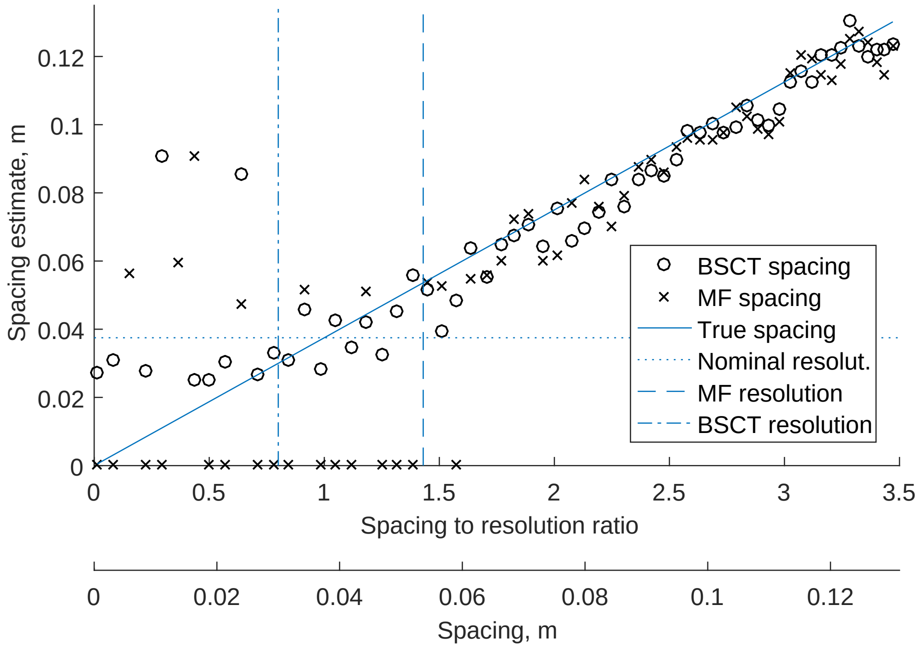

Figure 6.16: Target spacing estimates for the target profiles in Fig. 6.15. The resolution limit is shown as dotted line. The dashed lines are positioned at normalised spacings 0.8 and 1.43

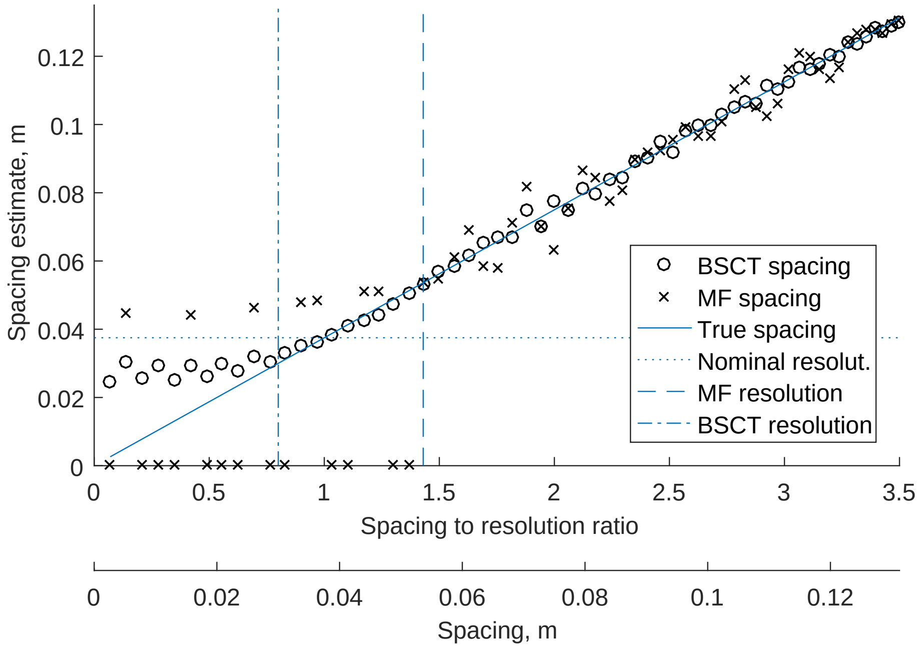

Figure 6.17: Target spacing estimates for simulated data. Two targets, SNR = 34 dB

6.4.4 Resolution, phase and signal central frequency

The resolution capabilities are influenced by the central frequency of the signal. The best resolution of 0.7 d_R is achieved when the mean value of the BSCT frequency profile is equal to the constant component of the theoretical curve (4.17) and the zero lobe is removed correctly in (4.19). The worse case is when the frequency profile covers a section close to the sinusoid extreme values and the spectrum is practically flat. In this case the resolution is equal to the nominal resolution. This effect is shown on Fig. 6.18 where the left plot is produced for f_c = 15 GHz and the right is for f_c = 15.3 GHz (in the context of the spectrum presented in Fig. 6.9). It should be emphasized that the central frequency has effect on the range profiles created using matched filter also. The functional resolution of BSCT even in the worse case is still better than MF resolution. Confirming these relationships and finding a better way to remove the zero lobe could be an area for future research.

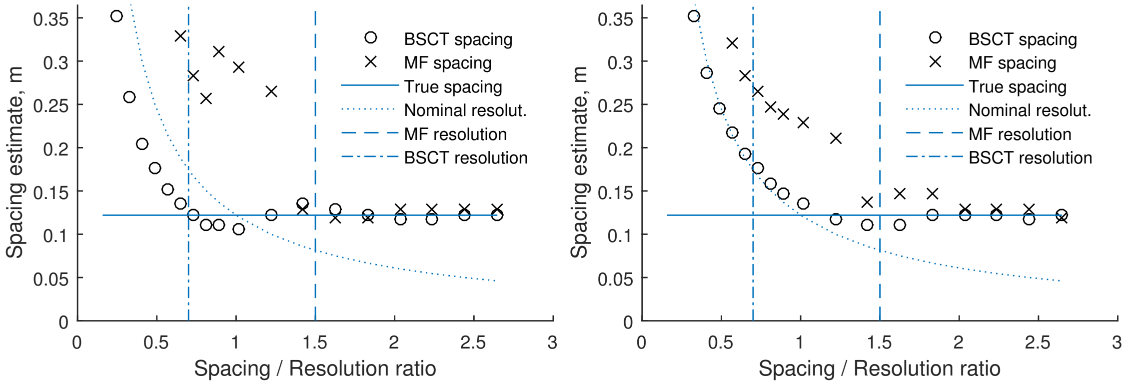

Figure 6.18: BSCT spacing estimates and the central frequency. Two flat plates (separation 12.2 mm) data. The best and and worst cases depending on the central frequency are shown. The vertical lines are at relative spacing 0.7 and 1.5

6.4.5 The BSCT frequency profiles at RF

The BSCT frequency profiles are shown on Fig. 6.19 for simulated and real targets. The SNR was similar, about 34 dB. The scatterers of the turntable distort to some extent the ideal frequency interference pattern expected from to objects. The distortion in the spheres experiment (Ex9) is stronger than the one with the rods (Ex8) as the RCS of the spheres is 10 dB lower and the turntable scatterers are the same. The transformation window can be reduced in an attempt to handle the clutter.

It worth noting the difference between the frequency profiles for RF and ultrasound bands. Both were simulated with high SNR. The profiles are shown in Fig. 6.20. Also, a third plot is provided where the bat waveform is simply scaled to RF. Even though the the normalised spacing in resolution gates is the same, the value of the phase information (or the zero location) is lower as the ambiguity in the lower RF bandwidth (relative to the central frequency) is much higher. Preliminary tests with NLS approach for fitting a sinusoid to the frequency profile were not successful as compared to the case with the ultrasound bandwidth measurements. The zero locations can't be used also due to the inherent ambiguity. Methods for direct estimation of the spacing from the frequency profile will not be studied further. An approach exploiting both magnitude and phase information after [104] can be considered.

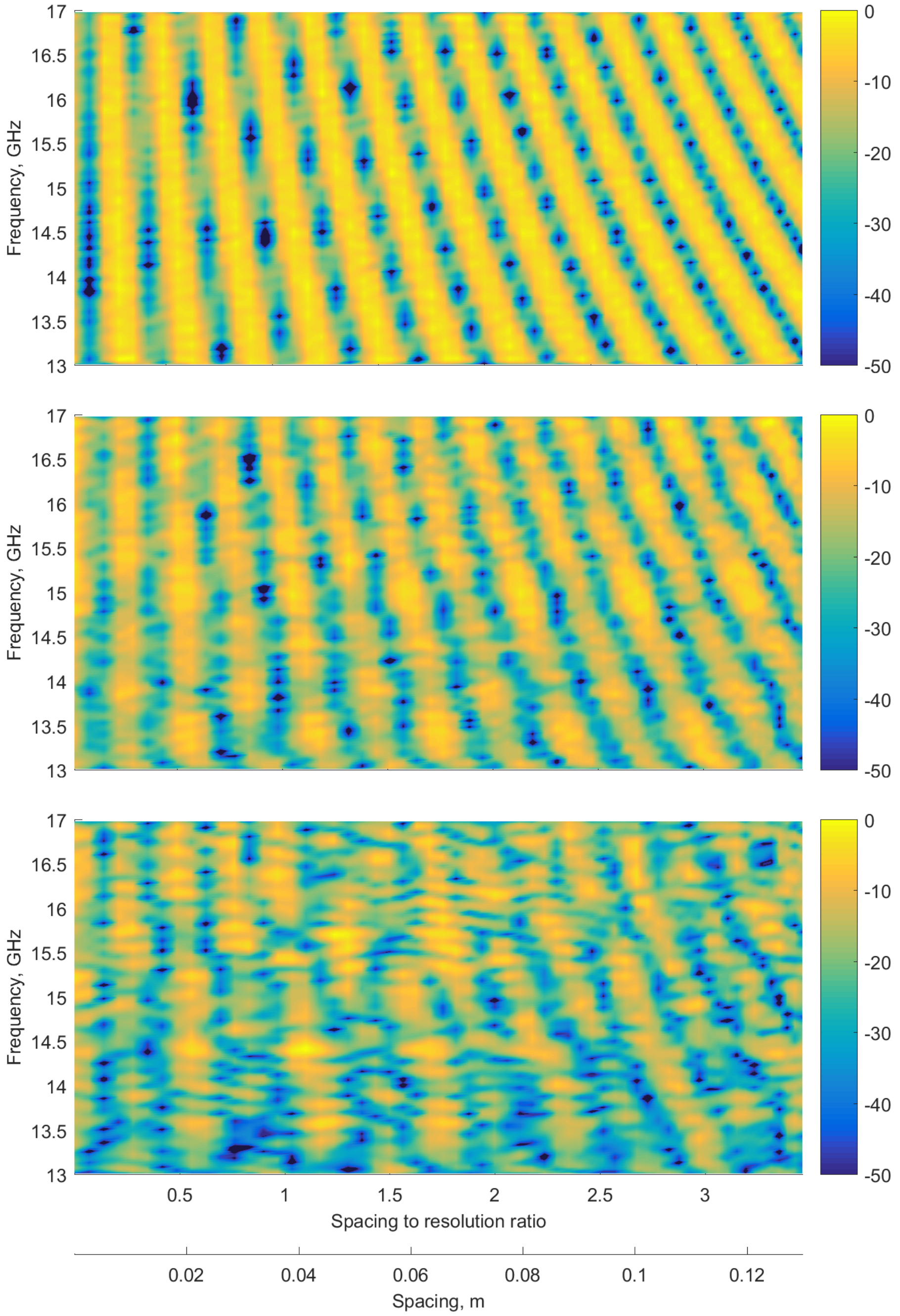

Figure 6.19: BSCT frequency profiles at RF for simulated data, vertical rods and small spheres measurements (from top to bottom). SNR is about 34 dB. The colour encodes the energy in dB

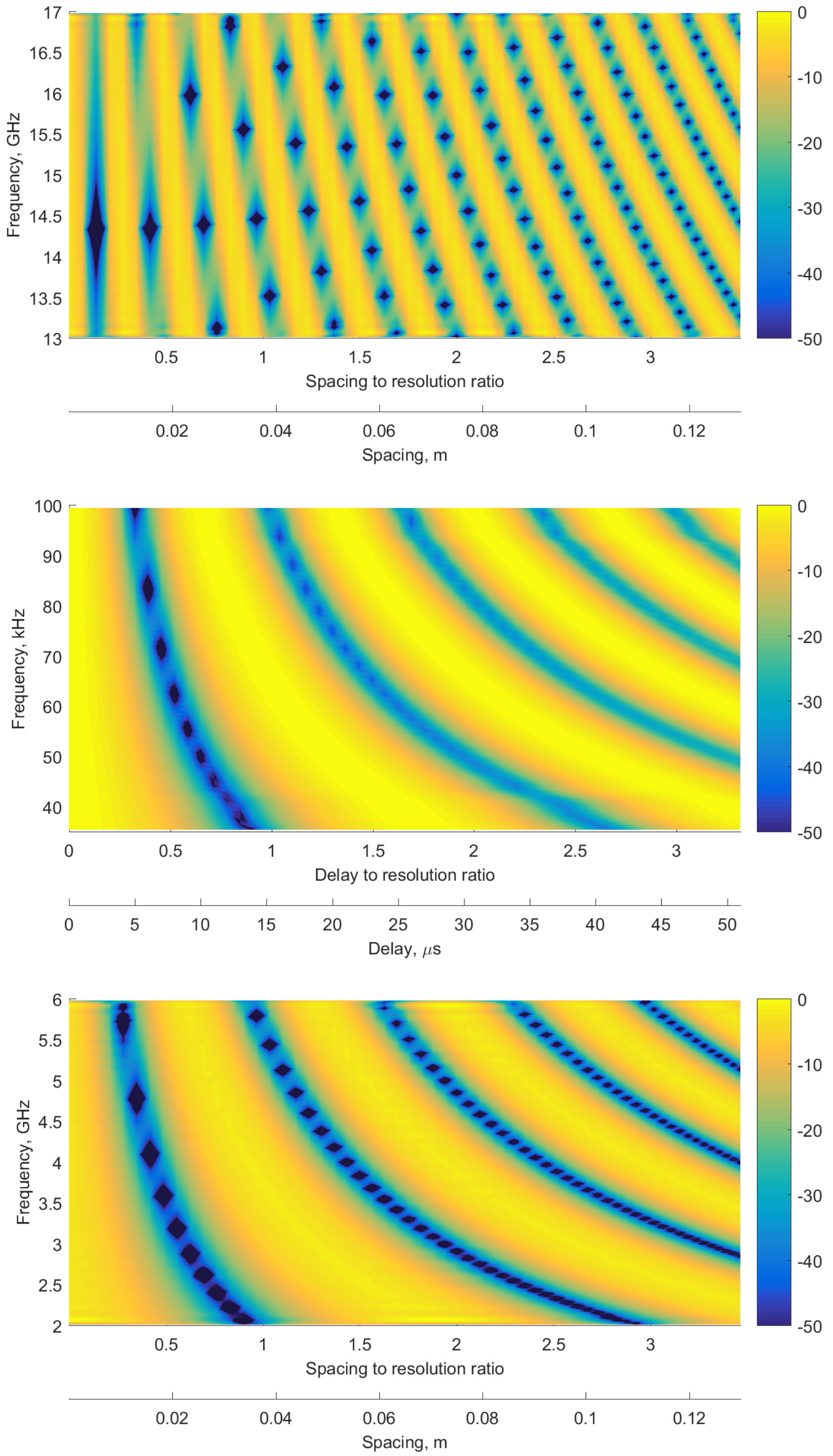

Figure 6.20: BSCT frequency profiles for simulated data, SNR = 68 dB. Top plot at RF, central frequency 15 GHz, middle plot at ultrasound, central frequency 67.5 kHz, bottom plot at RF, central frequency 4 GHz

6.5 Evaluation of model performance in noise

The range and spacing profiles were analysed for returns from the same target but at different noise level using the small spheres experiments. The noise level was increased in steps by $(7+10+4)$ dB. The outputs of BSCT and MF can be compared visually in Fig. 6.21. The true spacing is identified for SNR values 36, 30 and 20 dB. At SNR = 16 dB the spacing profile looks random. It should be emphasized that the BSCT performs worse than the MF for lower SNR. The fall-off in performance at reduced SNR is steeper with this detection scheme than with a matched filter since the noisy signal is effectively being correlated with a copy of itself rather than with a ‘clean’ reference. A key paper on the subject of noisy references is [111] where the advantages for detection in passive MIMO radar networks are developed.

The effect of pure Gaussian noise is shown using simulated data. The SNR was 17 dB. An example range and spacing profiles are shown in Fig. 6.22 for target spacing 0.122 m. The second target is much easier to be identified in the BSCT spacing profile in the simulation than in the small spheres experiment. It is likely that an interference from the environment makes the difference. The MF range profiles are not so sensitive to week interfering scatterers as the two target peaks are clearly distinguishable both in Fig. 6.21 and in Fig. 6.22.

The spheres experiment demonstrates the effect of the clutter. Multiple non-target related peaks are observed in the BSCT output for the spheres (Fig. 6.21). These become even more obvious if the spacing profiles for the plates, the rods and the spheres are compared. The range and spacing profiles for different targets are shown in Fig. 6.23. Both the rods and spheres experiments have similar SNR but the residual background is stronger for the spheres. The background scatterers act as additional targets and change the problem to multiple (more than two) close scatterers resolution.

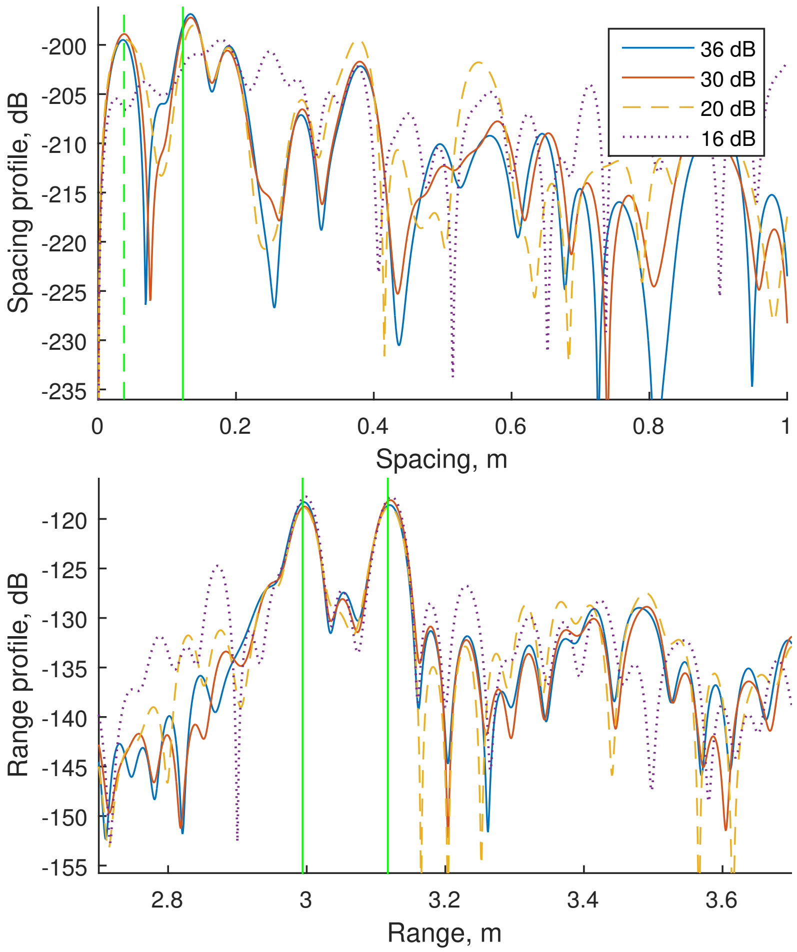

Figure 6.21: Spacing and range profiles for weak targets: two spheres. SNR is progressively reduced

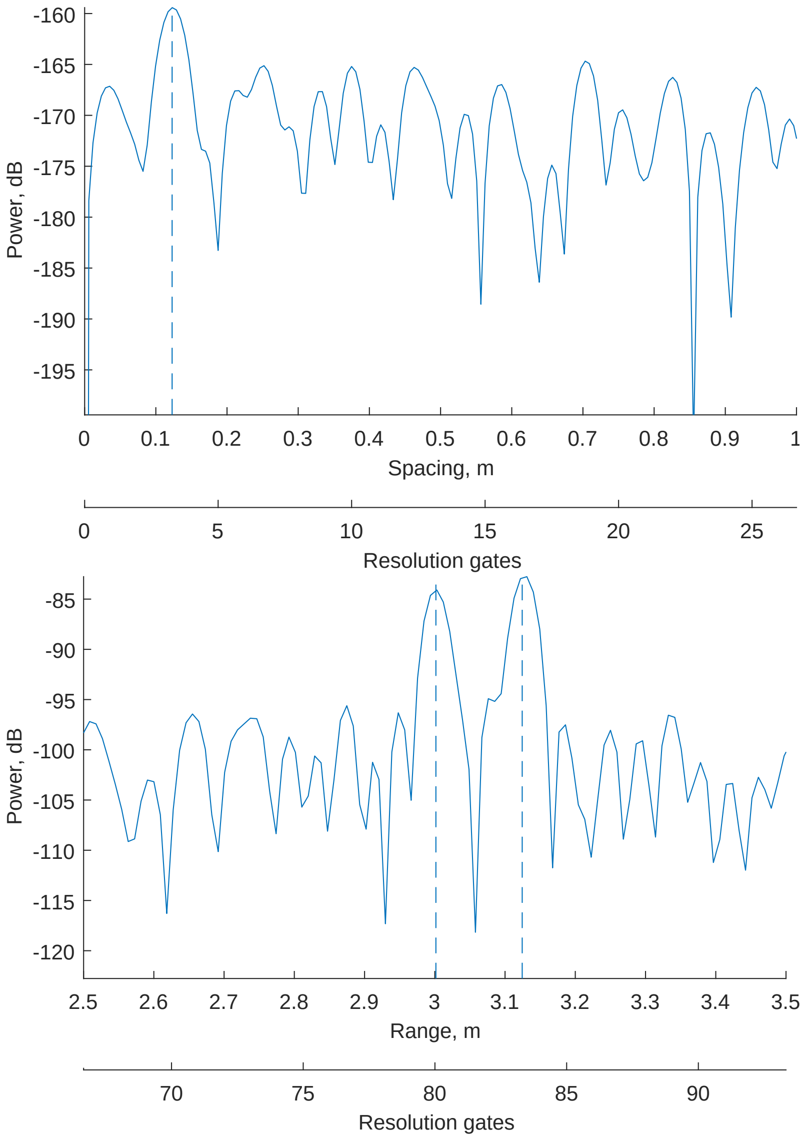

Figure 6.22: Spacing and range profiles for simulated targets separated by 0.122 m. The SNR is 17 dB

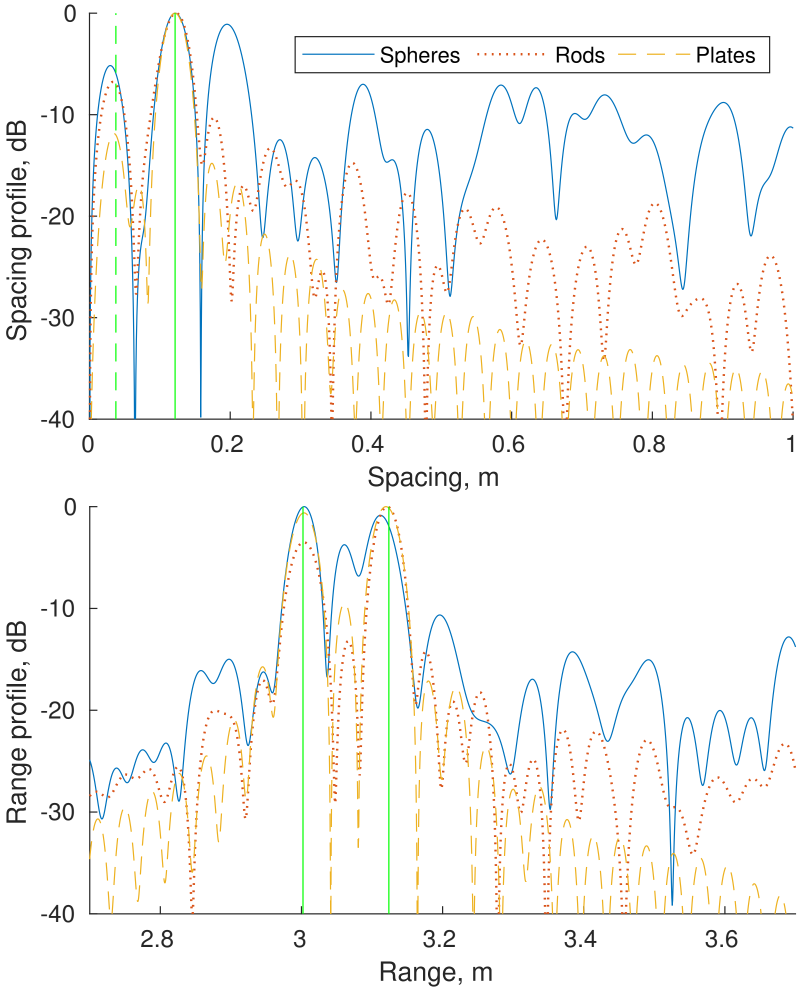

Figure 6.23: Spacing and range profiles for flat plates, vertical rods and spheres. The SNR is 70, 32 and 36 dB respectively. The target strength and noise level also differ between the targets

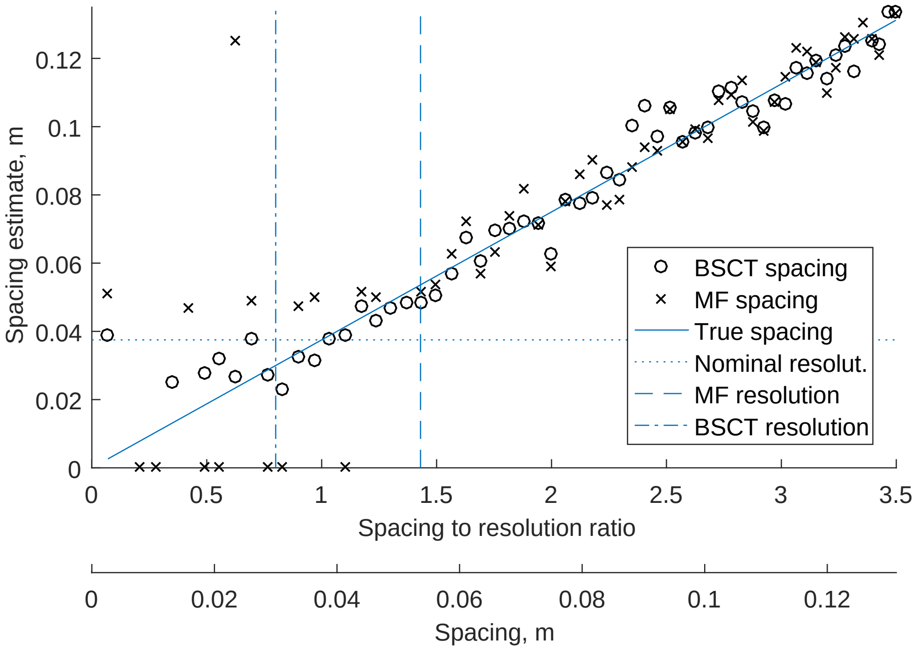

Figure 6.24: Target spacing estimates for simulated targets at variable spacing. The SNR is 17 dB

The spacing estimates using the BSCT and the MF profiles for simulated targets and white Gaussian noise are shown in Fig. 6.24. The improvement in the resolution is still observed.

6.6 Summary

The frequency response of two close targets was measured with a VNA in the range 13–17 GHz. The BSCT algorithm was described with special attention on the preprocessing steps necessary for real world measurements and the optional integration with other popular “superresloution” techniques.

The BSCT capability to process radar measurements was confirmed. The range resolution was expressed relative to the nominal resolution. The spacing in resolution gates was varied in two ways – either by changing the bandwidth of the waveform or by changing the physical spacing between the targets. The BSCT spacing profiles demonstrated 1.5–2 times better resolution potential than the MF range profiles. It was also shown that exploiting the phase information for further improvement of the resolution will be harder compared to the ultrasound measurements case.

As expected, the MF performed better than the BSCT at low SNR. In addition the BSCT response interpretation can be complicated by the presence of interfering scatterers. The loss of SNR and the response in case of different scatterer magnitudes and more then two scatterers will be considered in the next chapter. Other areas of future research will be also discussed.

Chapter 7

Supplementary estimates and challenges

A further discussion of additional research challenges relating to the developments in this thesis follow. In particular, an approximation of the signal-to-noise ratio; extension for the case of different size targets; connection of the BSCT with the autocorrelation function are provided.

Acoustic signal processing in bats can be related to a wide variety of additional topics that are subject to active research. Extensive development or even a literature review on all of them could not be covered in a single work. In this last chapter only the main ideas will be discussed and why the author consider them connected to his work as areas for future research.

7.1 Generalization for different scatterer magnitudes

In Chapter 4 only the case where the two targets are the same size has been investigated. It is easy to show that the model is valid for targets of different size. Equation (4.9) is modified by assuming different amplitudes A_1 and A_2 of the scatterers.

$$x(t) = A_1 x_C(t-t_1)e^{-j2\pi f_0 t_1} + A_2 x_C(t-t_2)e^{-j2\pi f_0 t_2}$$

$$\begin{aligned} X(f) &= A_1 X_C(f)e^{-j2\pi(f+f_0)t_1} + A_2 X_C(f)e^{-j2\pi(f+f_0)t_2} \\ &= A_1 X_C(f)e^{-j2\pi f^I t_1}\left(1+\eta e^{-j2\pi f^I(t_2-t_1)}\right) \\ &= A_1 X_C(f)e^{-j2\pi f^I t_1}\left(1+\eta e^{-j2\pi f^I \tau}\right) \end{aligned} \tag{7.1}$$

where $\eta = A_2/A_1$ and $f^I = f + f_0$.

The energy spectral density becomes

$$\begin{aligned} P(f) &= X(f)X(f)^* \\ &= 2A_1A_2P_C(f)\left[\cos(2\pi f\tau + \psi_\tau) + \frac{\eta^2+1}{2\eta}\right] \end{aligned} \tag{7.2}$$

If both signals are the same size the envelope goes through zero and the variation in power is $4A^2$ peak to peak. If they are different sizes then the power varies from $(A_1 - A_2)^2$ to $(A_1 + A_2)^2$, a range of $4A_1A_2$.

Above equation is similar to (4.10). A notable difference is that the cosine is summed with a constant that is bigger than one so the “zeroes” of the spectrum will not be so “deep”. When the mean value of the spectrum is removed as in Sec. 4.3.1 this difference will disappear.

7.2 Representation of more than two scatterers

The spectrum of three overlapping echoes was analysed in [47, 48]. The conclusion was that the spectral block generates spurious delay estimates or “ghost peaks” when more than two echoes are present. Of course this is part of the spacing profile concept. A peak is generated for each possible spacing between the scatterers. Lets consider the most simple case of more than two scatterers, i.e. lets $x(t)$ is a return from a target consisting of three scatterers

$$\begin{aligned}
x(t) &= x_C(t-t_1)e^{-j2\pi f_0 t_1} + x_C(t-t_2)e^{-j2\pi f_0 t_2} + x_C(t-t_3)e^{-j2\pi f_0 t_3} \\
X(f) &= X_C(f)e^{-j2\pi(f+f_0)t_1} + X_C(f)e^{-j2\pi(f+f_0)t_2} + X_C(f)e^{-j2\pi(f+f_0)t_3} \\
&= X_C(f)e^{-j2\pi f^I t_1}\left(1 + e^{-j2\pi f^I(t_2-t_1)} + e^{-j2\pi f^I(t_3-t_1)}\right)
\end{aligned} \tag{7.3}$$

The energy spectral density $E(f)$ is

$$\begin{aligned}
E(f) &= X(f)X(f)^* \\
&= E_C(f)\left(1 + e^{-j2\pi f^I \tau_{21}} + e^{-j2\pi f^I \tau_{31}}\right)\left(1 + e^{-j2\pi f^I \tau_{21}} + e^{-j2\pi f^I \tau_{31}}\right)^* \\
&= 2E_C(f)\left(\cos(2\pi f^I \tau_{21}) + \cos(2\pi f^I \tau_{31}) + \cos(2\pi f^I \tau_{32}) + 3/2\right)
\end{aligned} \tag{7.4}$$

where τ_{ij} is the delay between the scatterer i and scatter j. This can be compared to the corresponding equation for two scatterers (4.10). Each pair of scatterers is represented by a cosine. All derivations from Chapter 4 can be repeated here. Inverse FT will convert each cosine to a positive and a negative peak at $\pm\tau_{ij}$ on the time axes.

Lets discuss the most general case of multiple targets. The frequency profile of BSCT (6.2) can be compared to the Daniel spectral estimation method (3.12). Therefore it can be assumed that the BSCT frequency profile represents the spectral energy of the target return. The IFFT of the spectral energy is the autocorrelation function (ACF) of the signal. Thus the spacing output can be considered a modified autocorrelation where the zero lobe is removed.

The relationship between the BSCT and the ACF is shown for two scatters target in Fig. 7.1. The loss of absolute scatterer position is shown in Fig. 7.2 for the case of three scatterers.

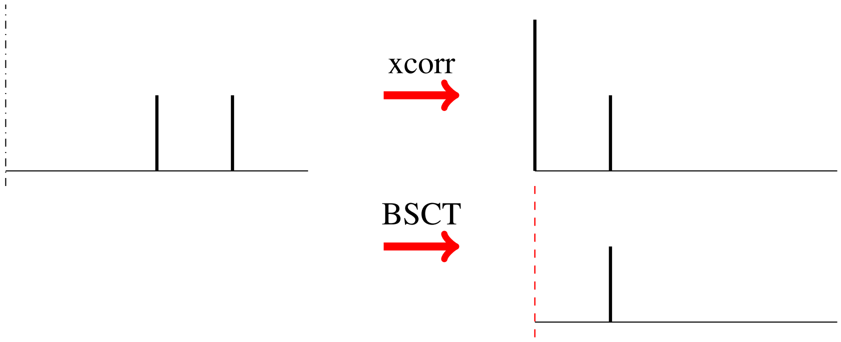

Figure 7.1: BSCT of two impulses as compared with autocorrelation

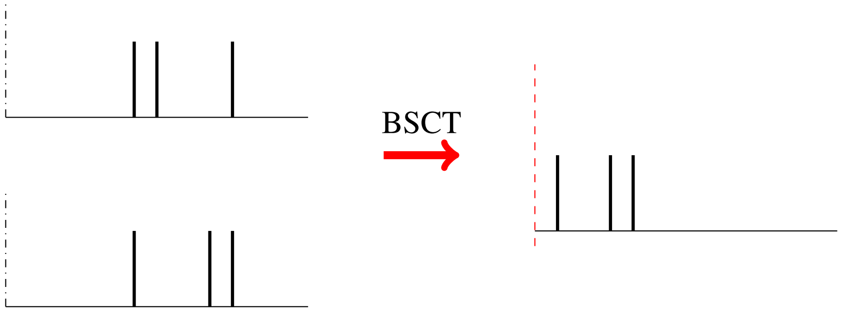

Figure 7.2: BSCT of three impulses. Location information is lost

7.3 SNR after BSCT transformation

A fall-off in BSCT performance at reduced SNR was already observed in Sec. 6.5. This was expected as the noisy signal is correlated with a copy of itself rather than with a “clean” reference. How big is the loss of SNR relative to the MF is of major concern for any practical application of the algorithm. The BSCT SNR is evaluated by simulation of a simple scenario – a band limited impulse waveform $x_C = A\delta(t)$ and two point scatterer target $x_T = \delta(t-\tau) + \delta(t+\tau)$.

The following steps were implemented and run in MATLAB (Listing B.9).

1. generate noise waveform sequence $w[n]$ with variance σ^2

2. generate signal $s[n]$ containing two impulses with amplitude A at $n = \pm p$

3. $\text{SNR} = A^2/\sigma^2$
4. sum the noise and signal, $x[n] = w[n] + s[n]$
5. apply BSCT transformation, $y[n] = \text{ApplyBSCT}(x[n])$
6. get BSCT signal impulse magnitude at index $2p$, i.e. $A_{\text{BSCT}} = y[2p]$
7. calculate BSCT noise power σ^2_{BSCT} as the variance of the signal with discarded values at index $\pm 2p$
8. the SNR for BSCT is $\text{SNR}_{\text{BSCT}} = A^2_{\text{BSCT}}/\sigma^2_{\text{BSCT}}$

The relationship between the SNR for BSCT and MF is shown in Fig. 7.3 for different signal lengths M. It can be seen that the BSCT SNR is reduced relative to the MF SNR by 6 dB for high SNRs. The ratio of the signal energy and the noise power is reduced 4 times. For low SNR the change in dB for BSCT is two times the change in dB of the SNR. The critical SNR below which the performance is sharply degraded depends on the signal length or the time-bandwidth product. For the bat-like waveform it is approx. 15 dB.

Analytical treatment of the SNR could be subject of future work. It can be further extended to account for targets of different size.

7.4 Open questions and future work

Explaining bat echolocation is not a simple task. While the core features of the existing models were extracted in the previous chapters, they haven't been studied in the context of alternative high resolution and deconvolution techniques. I addition, bat auditory system neural processing can be correlated with the state of the art research in signal processing and machine learning and thus inspire further studies.

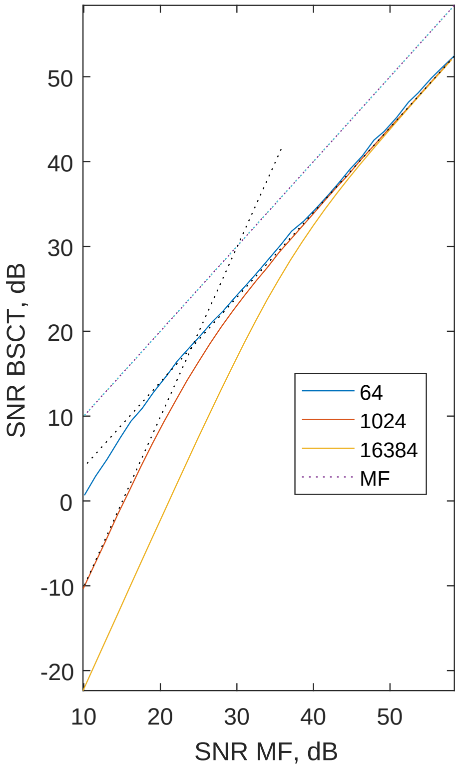

Figure 7.3: BSCT SNR as a function of signal SNR and the time bandwidth M

Bioinspired waveforms and sparse sensing The specific waveforms that bats use and the hyperbolic frequency sampling in the receiver are another area of potential research. These can be associated with the recent research in the field of compressed sensing and sparse signal reconstruction [112, 113].

Neural coding The representation of the signals in the brain is different. There is no regular sampling at constant rate. Neurons exchange information through neural spikes which provide a kind of binary coding on a continuous time axis. The physiological limitation of the firing rate in the context of the echolocation means single or at most a few spikes per frequency channel per echo. A massively parallel processing is the expected solution. Considering the cost of the neural activity, ideas for optimal computational architectures can be foreseen.

Non-linear signal processing and neural networks In bat auditory system there is non-linear transformation of the magnitude of the signal, which in this work was assumed to be squaring. But it could be also just the magnitude or some power different from 2. The deep learning techniques can provide much more flexible framework for handling multi-layer non-linearities. It would be interesting if the processing described in this research is implemented as neural network. This will allow smooth transition from target resolution to target recognition. A recent developments in the field of deep learning is the introduction of the *batched normalization* technique [114]. It can be connected to the mechanism for zero lobe suppression that was show to be important for resolving close targets. The added flexibility of different low and high pass filter implementation can allow tuning the model to specific targets and clutter environment.

Different domain applications The proposed technique can be studied in the context of the Doppler frequency and direction of arrival domains. Research in these domains can bring into consideration many established methods for comparison, interpretation and improvement. For example, two recently introduced methods for direction-of-arrival estimation are compared in [94], sparse signal covariance and sparse Bayesian frameworks.

Use of the phase information The “phase” information of the frequency domain representation in SCAT/BSCT also contain information about the spacing of the targets. This is not currently exploited in BSCT. At RF bands it is not so valuable as in the case of ultrasound, which is obvious from Fig. 6.20. Still future research can try to improve the algorithm by preserving the phase. Such approach for studying the complex output of the MF processor was shown to be successful by Rihaczek [104, 105].

Use of superresolution methods Superresolution techniques are methods for parameter estimation that provide resolution in range, frequency or direction of less than one resolution gate. They differ in the assumed signal model and noise characteristics. The BSCT algorithm allows some of the steps to be implemented using such superresolution and sidelobe supression techniques (Sec. 6.2). This means that the “prior art” in superresolution can be applied directly without having to carry out extensive development of the algorithms. Further research can explore the benefits of such approach. Direct comparison can be done also although the output of the BSCT is different, e.g. a spacing profile instead of a range profile.

Cognitive sensing The ultimate goal of a cognitive sensing system involves integration of the data collection and processing with the higher level tasks as target detection and classification, accurate localization and tracking, autonomous navigation and collision avoidance.

7.5 Summary

The BSCT receiver properties were studied for more complex scenarios. It was shown analytically that the model application is not restricted to targets of the same size. For more than two scatterers the spacing profile concept should be interpreted properly as it provides pictures that are different from the range profiles. The SNR after BSCT transformation is reduced by approximately 6 dB for high SNR and even more for low SNR. Analytical treatment of the BSCT SNR could be subject of future research. Other areas of future research were highlighted, e.g. exploitation of the BSCT phase for improved estimates and application of the model at different domains.

Chapter 8

Conclusions

The aim of this study was to investigate the mechanisms bats use to process echo acoustic signals and investigate if there are lessons that can be learned and ultimately applied to radar systems. The basic principles of the bat auditory system processing were studied and applied to radio frequencies.

After a review of the existing literature on bat echolocation capabilities and bat auditory system research, the main features of bat processing were derived. The FM bats are able to discriminate small shifts in the range of a single target close to the statistical limit, to resolve two target spacing differences as small as 2 μs (less than one third of the Rayleigh limit) and to discriminate stochastic targets based on their roughness. Their signal processing chain most likely does not rely on phase information. The absolute ranging is not so accurate – about 60 μs. The perception of the target also changes if another target is closer than about 60 μs. These are the features that have to be provided by the monaural auditory system models and that should be compatible with the bats amazing performance on a variety of tasks.

Existing models differ in the level of details and biological plausibility as shown in Chapter 2. The Spectrogram Correlation And Transformation (SCAT) receiver is a model of the auditory system that was proposed by Saillant *et al.* for the bat *Eptesicus fuscus*. It was selected for further analysis not only because it is one of the most frequently referenced studies. It is relatively simple yet biologically plausible, can be considered a functional model but provides a neural implementation at all stages. The temporal and spectral processing can be modelled separately, which is also an advantage when analytical models have to be done. The main insights from the analysis of SCAT can be summarized as:

- The cochlear block splits the signal into multiple narrowband channels
- All channels go through non-linear transformation and smoothing
- The temporal block performs signal compression and low resolution target ranging
- The spectral block performs fine range resolution in the frequency domain

It was recapped that when the signal in the time domain is concentrated in a very short interval it will be wider in the frequency domain. Therefore switching the domain can bring advantages when the sampling rate is limited. An impulse can not be sampled in time domain using finite sampling rate. This problem does not exist in the frequency domain. The same is valid for two impulses. In the frequency domain they are represented by a cosine which spans from minus infinity to plus infinity. In real measurements the magnitude and phase information can be collected only for a limited range of frequencies – a bandpass filtered version of the target response. This again will limit our capabilities to restore the original impulses.

In this thesis I have presented a baseband receiver that allows an analytical treatment of the output of a SCAT-like processing and that can also be applied to RF signals. Simulation and experimental results show that proposed baseband spectrogram transformation model gives a spectral output comparable with the output of the original spectrogram correlation and transformation receiver. This implies that

- processing of target echoes with a receiver based on the bat auditory system can be applied to signals that are centred on very high carrier frequencies, such as radar signals.
- the output of the spectral block does not depend on the phase information of the carrier signal and is a form of non-coherent signal processing; the spectral block will be more robust to loss of signal coherence than the matched filter.

The output of the Baseband SCAT (BSCT) has been compared analytically with that of the conventional matched filter for two closely spaced scatterers. It was shown that by removing the signal power which is present in all the frequency bins, the variations can then give the target separation. This is a biologically/neurologically plausible idea and changes the two-target problem to the much simpler one of estimating a single parameter (the modulation rate in the frequency domain). Results have shown that a bat-inspired spectrogram transformation can provide better range resolution performance than that of a conventional matched filter.

The model have been verified first with a set of laboratory experiments at ultrasound, using phantom echoes and real targets. The frequency range and bandwidth were based on bat echolocation call. In Chapter 5 the enhanced resolution of two scatterers was demonstrated experimentally by processing ultrasound measurements with BSCT receiver.

The feasibility of the BSCT receiver for radio frequency signals was demonstrated in Chapter 6. The experimental work is an evidence that the bat-inspired approach is robust to real targets. Pairs of flat plates, vertical rods and spheres were used to represent targets with two main reflectors. The enhanced resolution of two scatterers was demonstrated by processing radio frequency measurements with the BSCT receiver.

Looking more closely to the interference patterns for different relative positions between the scatterers it can be seen that the general shape and, in particular, the locations of the zeroes, are preserved between the experiments and the simulations. These features are likely to be significant for any scheme for resolving the close-spaced targets and this result indicates that the new algorithm, like the SCAT algorithm, retains the information which will later be needed to resolve the targets. Utilising the phase information in the BSCT spacing profiles can be subject of future research.

A note on the significance of the results

It can be argued whether improvement relative to the Rayleigh limit is an impressive performance in the context of the state of the art algorithms for superresolution that involve covariance matrices inversions or complex optimization and parameter search procedures. But this is the place to cite Rihaczek, 1996, "We have spent the past twenty years analysing real data from a variety of man-made targets ... we are led to the conclusion that the entire class of approaches based on mathematical target models is totally impractical and will not provide the required radar performance" and "the backscattering behaviour of general man-made targets is extremely complicated ... This is the reason for the failure in practice of maximum likelihood processing, maximum entropy processing, and other superresolution methods"[104, pp. 7].

The importance of the two point resolution problem was justified by Rihaczek [104, 105]. Rihaczek points out that resolving two scatterers is the only problem for which a moderate superresolution can be achieved if the complex response is utilized (i.e. the phase information from the receiver output is not discarded). In the typical high-resolution radar the majority of the range cells will contain composite responses [104, p. 450]. Three types of responses can be defined: (1) ones generated by single scatterer, (2) responses generated by two scatterers, and (3) responses generated by more than two scatterers. The general recommendation for the third case is to be approximated with two main scatterers if possible. [105, Sec. 1.3]. If this is not possible than the resolution of the radar is not adequate to its application.

Finally, we do not claim that BSCT gives better results than the conventional super-resolution techniques. A rigorous comparison to these techniques can be subject of future research. We haven't looked at its stability either, but as it may well be what bats have been doing for 50M years, and worked in our experiments, it is probably quite stable and certainly worth looking at further [115]. Although we must admit that it is just a hypothesis that bats use something like this, it is clear that it works.

Appendixes

Technical details that are important for the practical realisation of the models are provided as appendixes. This includes datasets, data structures, algorithms, exploratory data analysis, and data acquisition routines. Even though they do not add scientific value to the thesis they will make possible independent verification and validation of the results.

Appendix A

Exploratory analysis supplement

A.1 Physical target measurements with ultrasound

Important part of the ultrasound experiment was getting the ground truth (the real distance to the rods) with good accuracy, e.g. at least 0.5 mm, which corresponds to 3 μs time delay. Such accuracy is hard to achieve with mechanical ruler as the shape of the rods is not perfect and the exact phase centre as a function of the turntable position is unknown.

Exploration of the effect of the non-stationary environment and target deviations from perfect shape

The measurements of the central rod are shown for experiments (experiments 6-9 from Appendix C) with the same position of the turntable (Fig. A.1). Rod position is estimated using match filter. Wider scattering arownd specific angular positions (80^0 and 270^0) is due to the interference with the second rod and should be ignored.

The above chart shows that there is variation in estimated distance to the fixed central rod from experiment to experiment of about 1.5 mm. Additional variation of about 1.5 mm is observed at each single experiment due to imperfect target shape. This means that target

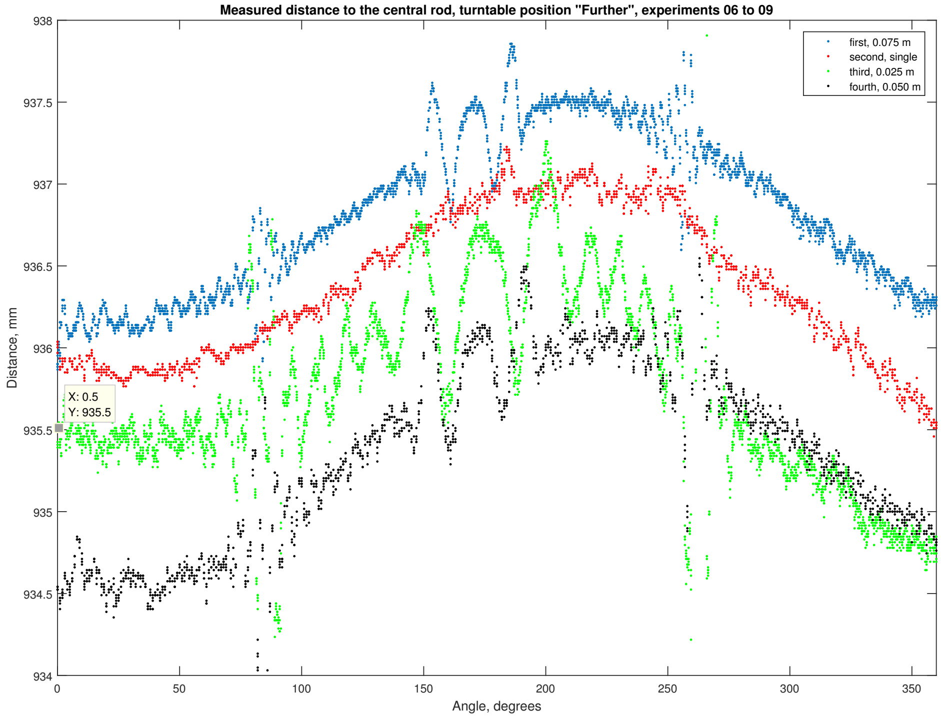

Figure A.1: Measured distance to the central rod for different perspectives (angles), four different experiments

distance calculated based on echo time delay can vary over 3 mm from measurement to measurement.

These measurements confirm the previous observation that the air is not a stationary environment and coherent signal processing is limited. Therefore in order to be able to do precise evaluation of measurement accuracy an estimate of the target position (ground truth) is needed at each angle and for each experiment accounting for both the environment at that particular moment and the target shape at that particular view angle.

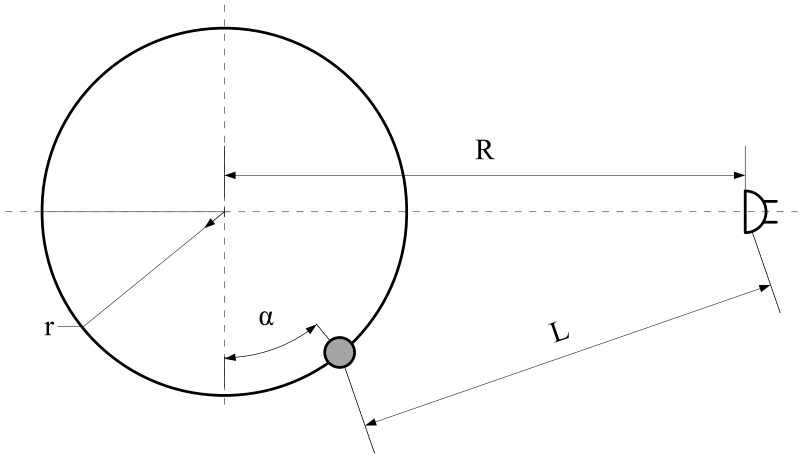

Figure A.2: Distance to a vertical rods on a turntable, important parameters

Estimation of the true rod locations

The precise distance from the speaker to reflecting surfaces and back to the microphone was estimated by curve fitting over multiple measurements at different turntable positions. It was based on the fact that the peak of the matched filtered signal provides unbiased estimate of the target location for a single target. This is good approximation of reality also for more targets when they are sufficiently separated. Therefore in order to estimate the true distance to and between the rods all measurements were used excluding the one in which the targets are closely spaced and match filter estimates are unreliable.

The relationship for the distance L between a point outside a circle and a point on the periphery of the circle is expressed based on the circle radius r, circle point angle α and the distance between the outside point and circle centre R (Fig. A.2):

$$L^2 = r^2 + R^2 - 2rRsin(\alpha - \alpha_0) \tag{A.1}$$

The precise distance from the speaker to reflecting surfaces and back to the microphone was estimated by curve fitting over multiple measurements at different turntable positions. The method used was "Nonlinear Least Squares" with "Trust-Region" algorithm. The distance to the table R, the radial position of the rod r and the initial angle shift α_0 were considered unknown model parameters. The independent variable was the angle α that set the turntable position. The dependant variable was the distance to the target L. It was measured by taking the peak location of the match filtered echo.

The procedure to get the ground truth:

- if there are more than one target, separate them for independent curve fitting

- fit the curve defined by (A.1) for the unknown model parameters R, r and α_0 based on measured distance L and corresponding angle α

- identify and remove outliers (these are the measurements when the rods are very close)

- fit the curve ignoring the outliers

- check model fit performance visually and based on selected statistics

- calculate estimates of the distance L based on the fitted model and save as true delay for each measurement;

The procedure for data fitting was applied for all experiments (see Appendix C). Curve fitting routines were verified by visual inspection of the measured distances and the fitted curves (Fig. A.3, experiment #9)

The importance of actual position estimation becomes obvious if the regions where the spacing between the targets is small are zoomed (Fig. A.4).

Evaluation of the accuracy of the range ground true

The accuracy of the estimate can be quantified by the root mean squared error (standard error) as 0.2643. Based on 1.96 standard errors it was concluded that the error of the estimate is less than 0.52 mm in 95% of all measurements.

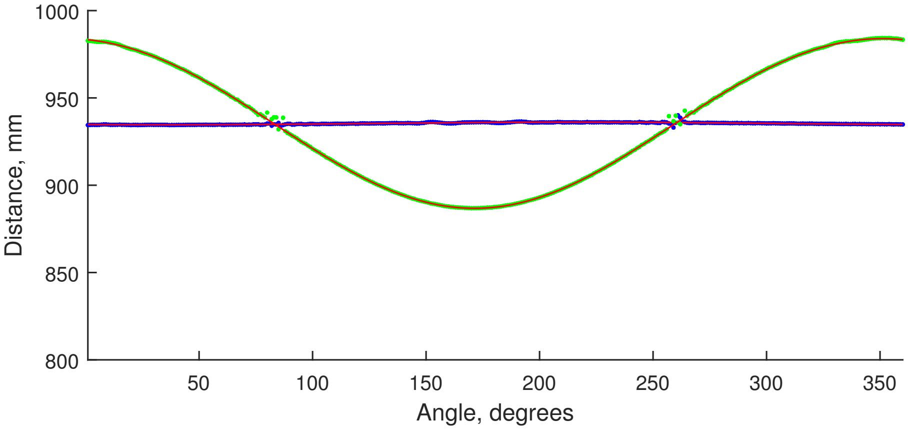

Figure A.3: Measured distances and fitted model, two rods, one in the centre and one at 50 mm

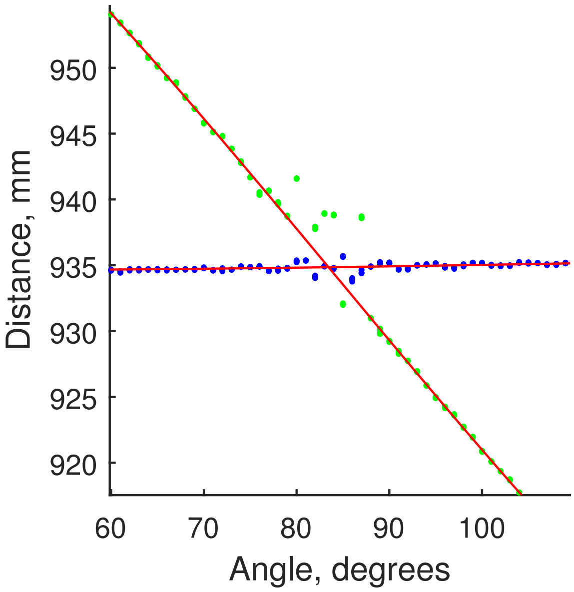

Figure A.4: Measured distances and fitted model, two rods, rods close spacing region

A.2 Turntable dimensions and backscattering

A turntable LT360EX, LinearX Systems, Battle Ground,WA, USA was used with additional support plate to fix the targets and provide variable spacing relative to the remote sensor (radar or ultrasound) (Fig. A.5) [116]. This target support structure is potential source of clutter interference. It can have significant effect on the return especially for weak targets. Therefore it is important to know the geometry of the support in details.

The overall dimensions of the turntable are 457x457x104 mm. The height of the chassis is 84 mm. The diameter of the platter is 406 mm and the height is 19 mm. On the top of the turntable platter a target support disk is mounted with a diameter of 240 mm and height 40 mm (Fig. A.6). Reflections from the front edge of the turntable chassis (x_1), the turntable platter (x_2) and the support disk (x_3) can be expected. The case when the antenna centreline is approximately at the level of turntable and the targets mounting points is explored further. Assuming a distance to the turntable centre $x_0 = 3.063$ m the above locations are $x_1 = x_0 - 0.457/2 = 2.835$ m, $x_2 = [2.860, 2.867]$ m and $x_3 = 2.943$ m.

A High Range Resolution Profiles of the turntable and support plate (further referred to as background) is shown on Fig. A.7a for 4 GHz signal. When the target rods are added the range profile changes but the front rod is hard to discriminate (Fig. A.7b). The range resolution profiles for a variety of different spacings of the rods can be observed on Fig. A.8 for two rod target and on Fig. A.9 for two small spheres. The range profiles are dominated by the reflection from the turntable platter.

The unwanted scatterers were removed by subtracting the background. The background removal is not perfect due to disturbances in the system, e.g. during mounting/dismounting the targets or due to vibrations from turntable operation. On Fig. A.10 a sequence of two rods HRRPs are presented at different positions of the turntable. As the experiment progress the background removal becomes less effective and the scatter-

Figure A.5: Turntable and support plate. Two small spheres are fixed into a grooves directly on the support plate

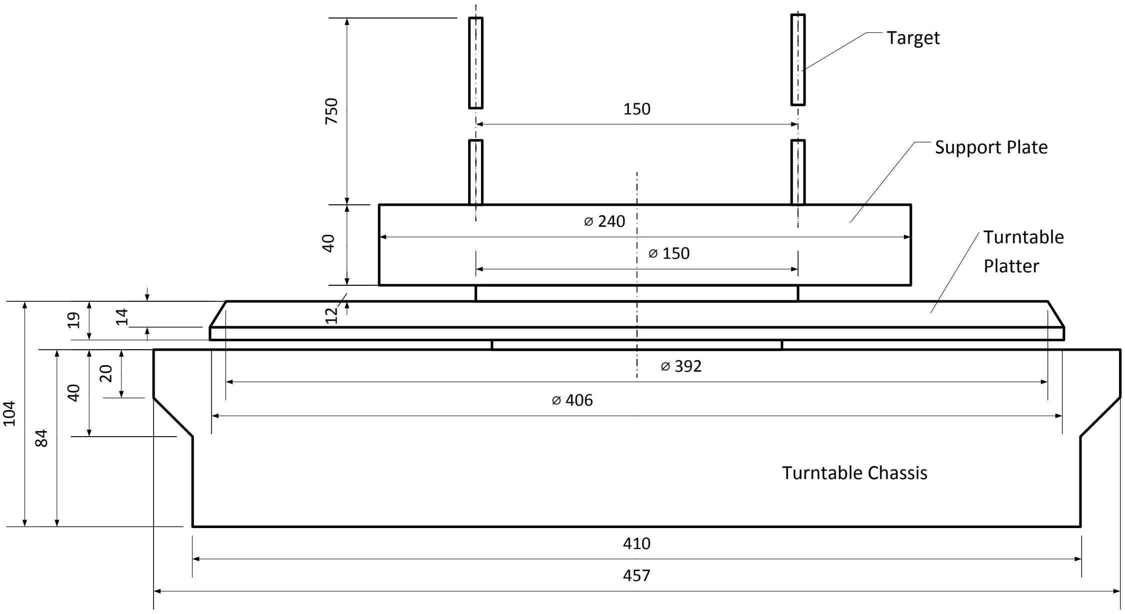

Figure A.6: Dimensions in mm of the turntable and the support plate with rod targets

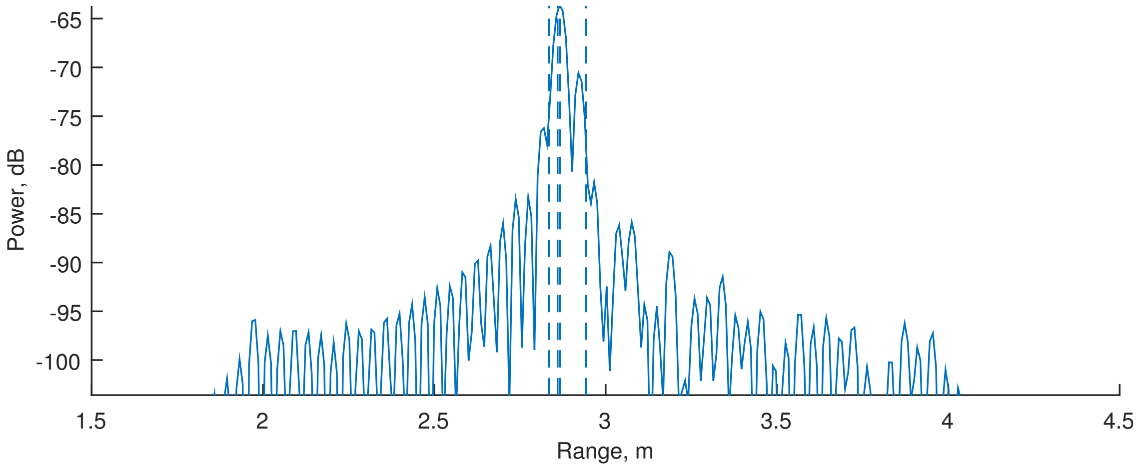

(a) Background HRRP. The dashed vertical lines mark the positions of the main turntable scatterers

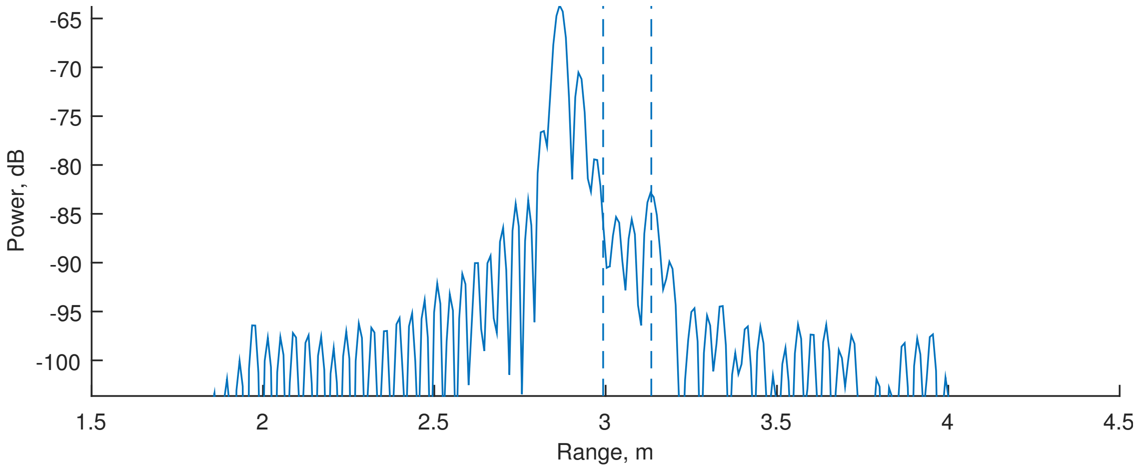

(b) Turntable plus two rods HRRP. The dashed vertical lines mark the rod locations

Figure A.7: HRRP for the background (top) and for the target plus background (bottom). The dashed vertical lines mark the positions of the main turntable scatterers at the top figure and the rod locations at the bottom figure. Signal bandwidth is 4 GHz

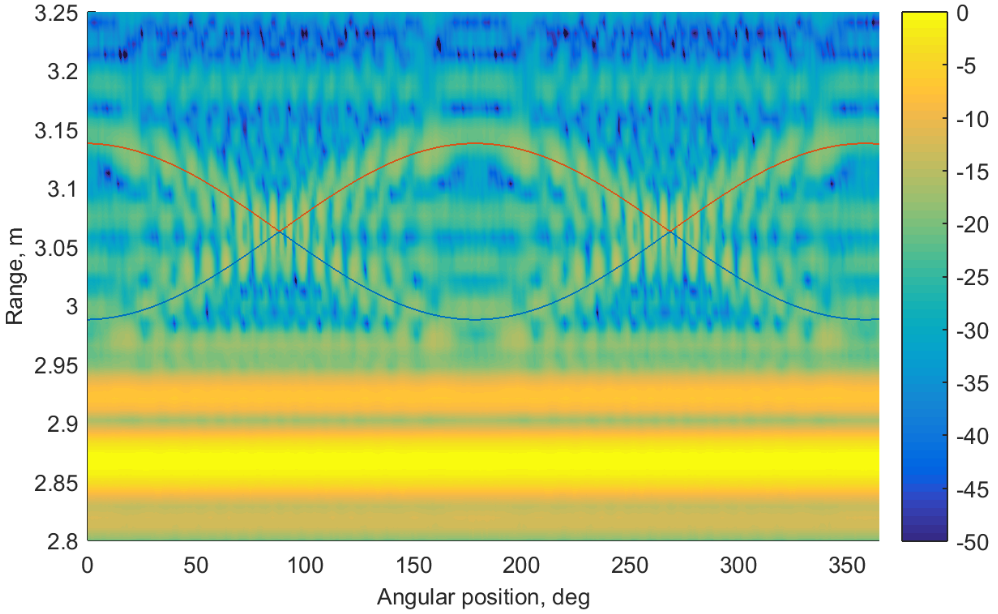

Figure A.8: HRRPs, no background removal, vertical rods

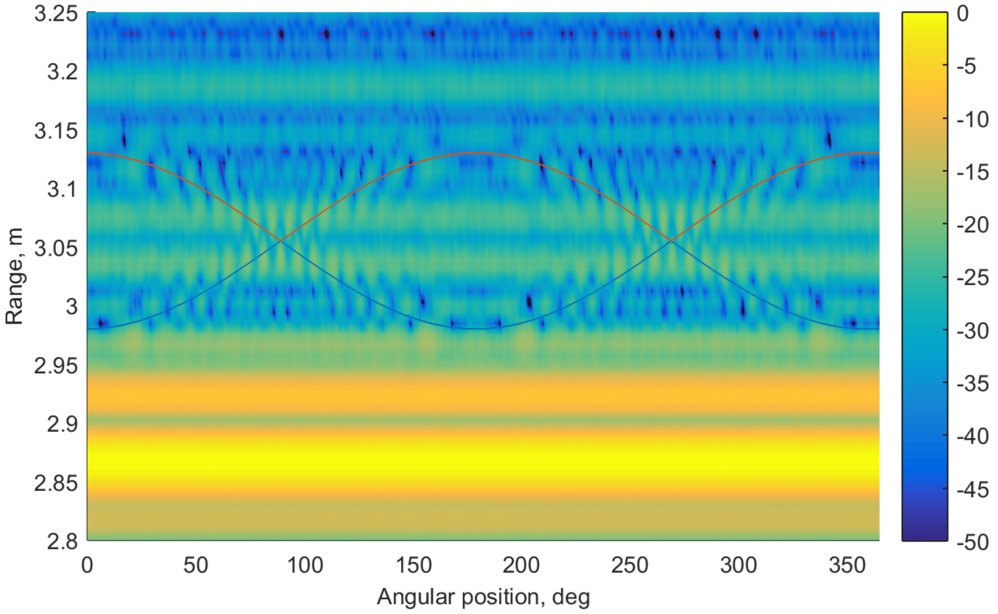

Figure A.9: HRRPs, no background removal, small spheres

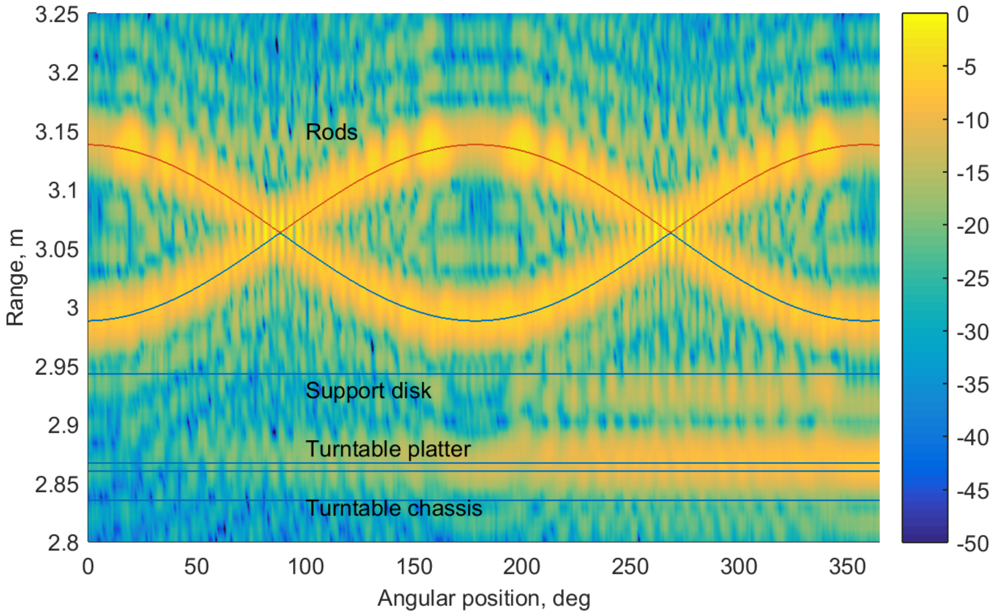

Figure A.10: HRRP for vertical rods. Background removal effectiveness degrade with the accumulation of turntable rotation steps

ers from the turntable and the target support plate start to be clearly distinguishable. For clarity the range profiles collected at 20 and 339 degrees are shown on Fig. A.11. Both measurements are performed with rod spacing of a 0.14 m. While on the first plot the background is successfully reduced below the noise level, in the second plot the turntable scatterers are comparable with the rod scatterers. For these 4 GHz bandwidth measurements the lobes representing the targets are clearly separable in both cases. Next the range profiles are shown for two small spheres (Fig. A.12). In this case there is no adverse tendency with time but the targets are 10 dB weaker and the impact of the residual background should be stronger.

The initial experiments with rods (Ex0 and Ex6) were performed with the antenna centreline at the level of rod tips or approximately 0.7 m above the rods mounting points. The distance to the turntable centre was 2 m and 3 m respectively (Fig. A.13a). With these arrangements each rod produced two distinguishable reflections separated by about 10 cm

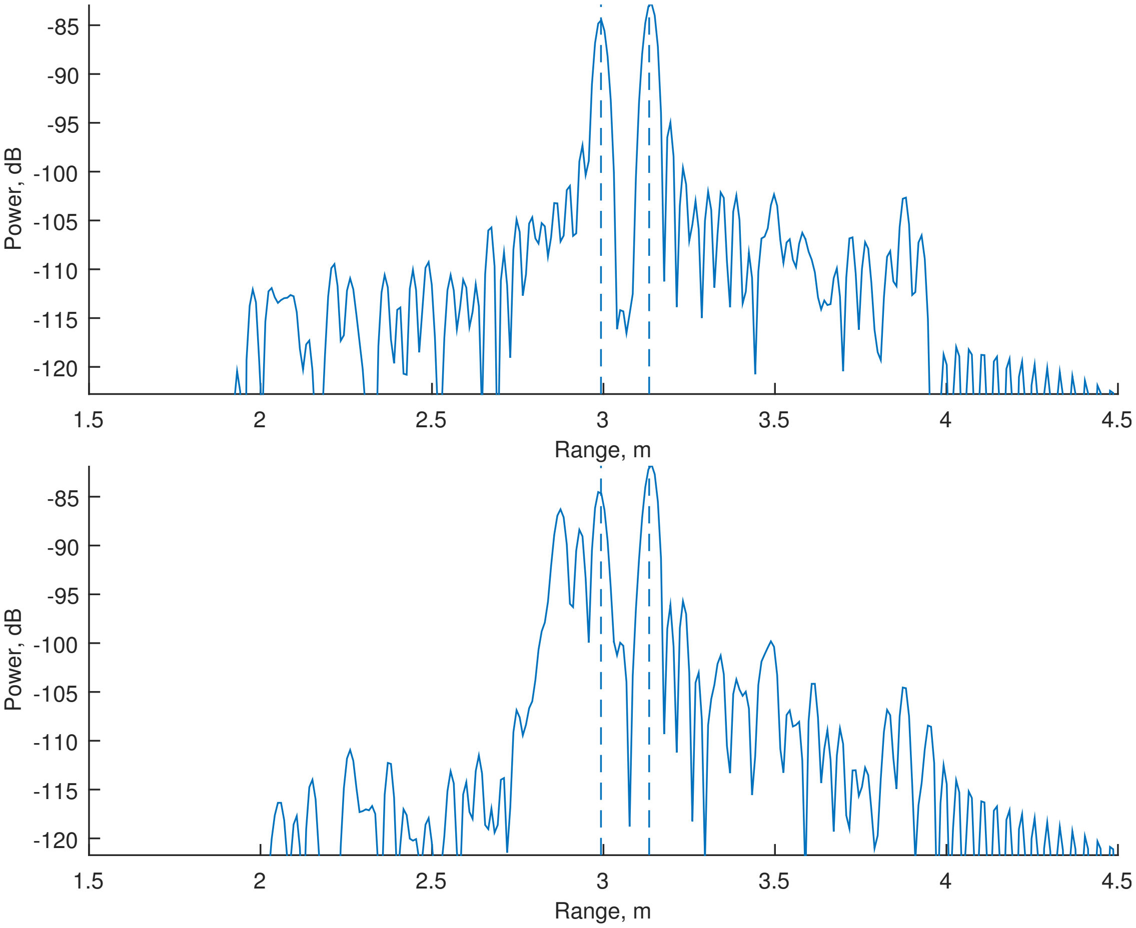

Figure A.11: HRRP for rods after background removal. The top plot is at 20 deg, the bottom at -20 deg. After a 320 steps the background removal is not perfect and the return from the turntable platter is visible. The dashed vertical lines mark the true positions of the rods

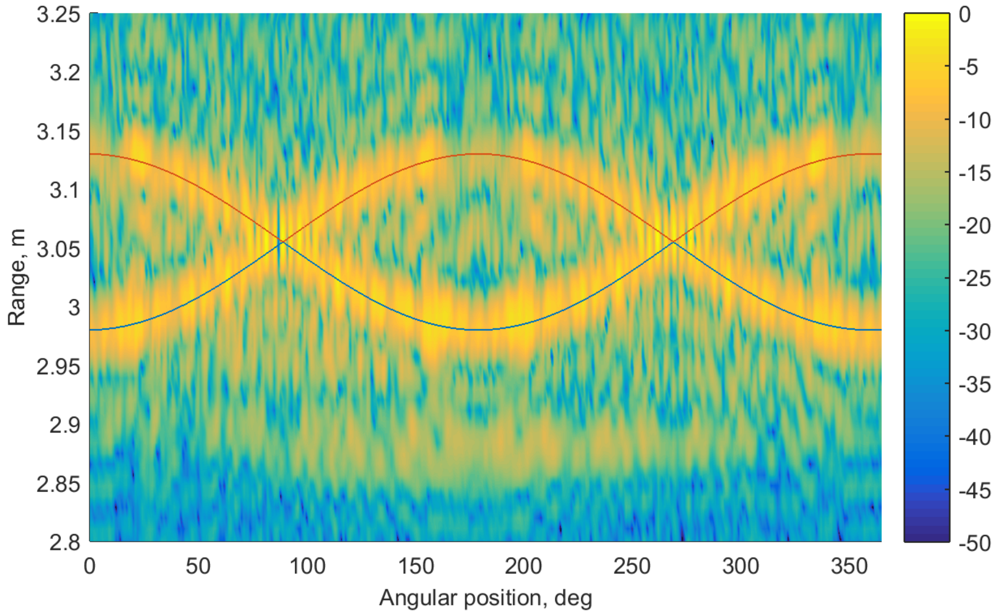

Figure A.12: HRRP for small spheres, 10 dB less power than the rods in Fig. A.10

– one from the tip and one from the support attachment point (Fig. A.14, Ex6). These pairs of scatterers have fixed spacing between them that is not related to the turntable angular position. Another complication was the clutter range distribution. Even though the power of the background was reduced (see Tab. C.4), the main clutter scatterer was overlapping with the front rod tip scatterer for Ex6 (Fig. A.15a) and with the rear rod for Ex0 (Fig. A.15b).

These settings can be used to explore the interference between two targets each consisting of two scatterers at fixed spacing. They have not been explored further as these present more complicated scenario than the one studied of just two close scatterers. The background scatterers were mixed with the target and each rod produced two scattering centres. In order to suppress the reflection from the tips of the rods the whole turntable was lifted up relative to the antenna beam (Fig. 6.3b, Fig. A.13b).

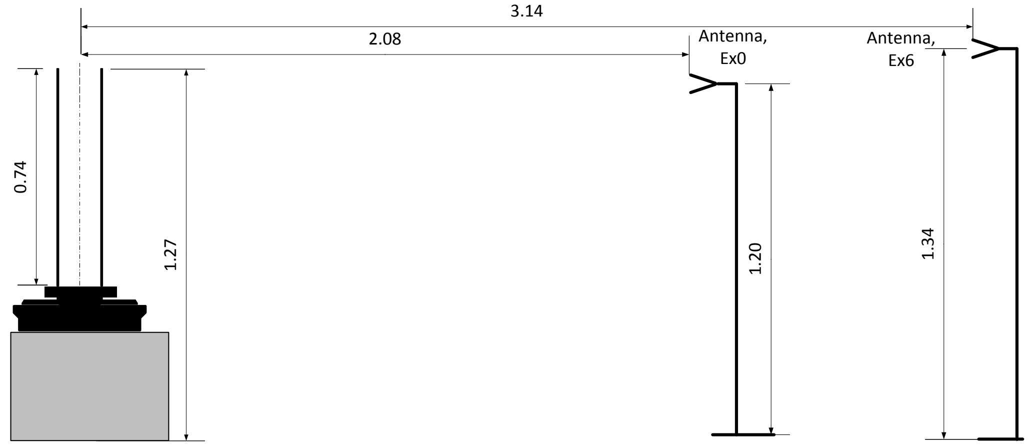

(a) Experiment Ex0 and Ex6

(b) Experiment Ex8

Figure A.13: Different arrangement of the experiments with two rods on a turntable, Ex0, Ex6 and Ex8 (final)

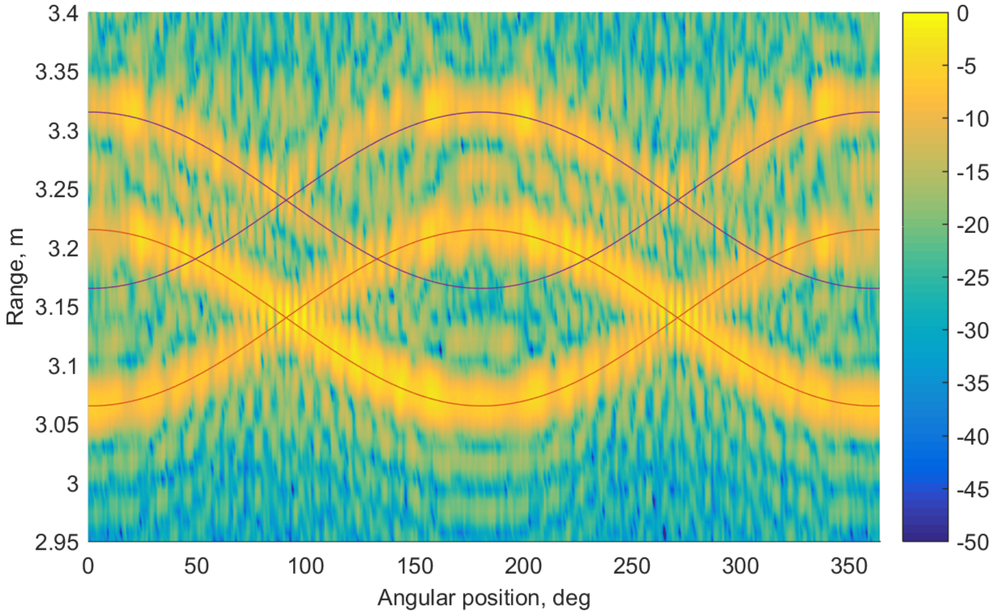

Figure A.14: Target HRRPs as a function of turntable position for two vertical rods. Two scatterers per rod are observed separated by 0.1 m. The actual scatterers positions are shown with continuous curves.

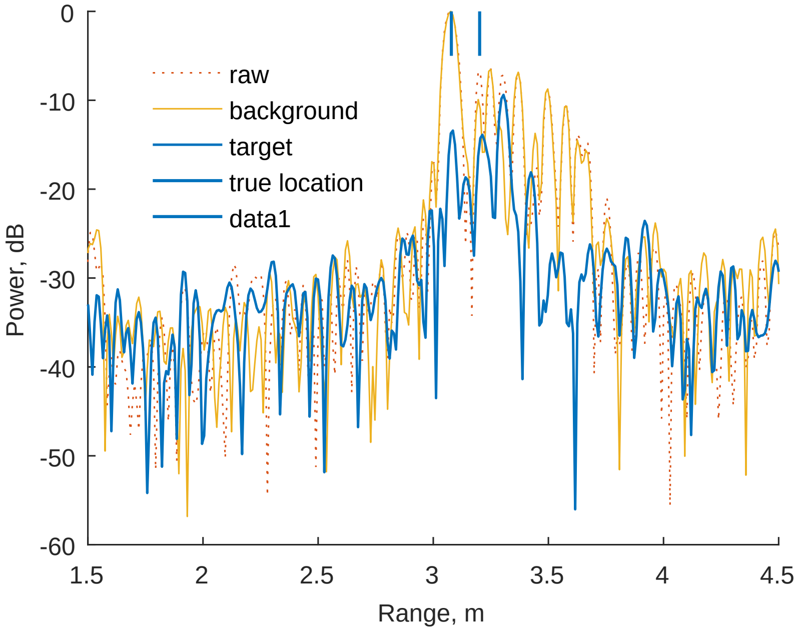

(a) Experiment Ex6

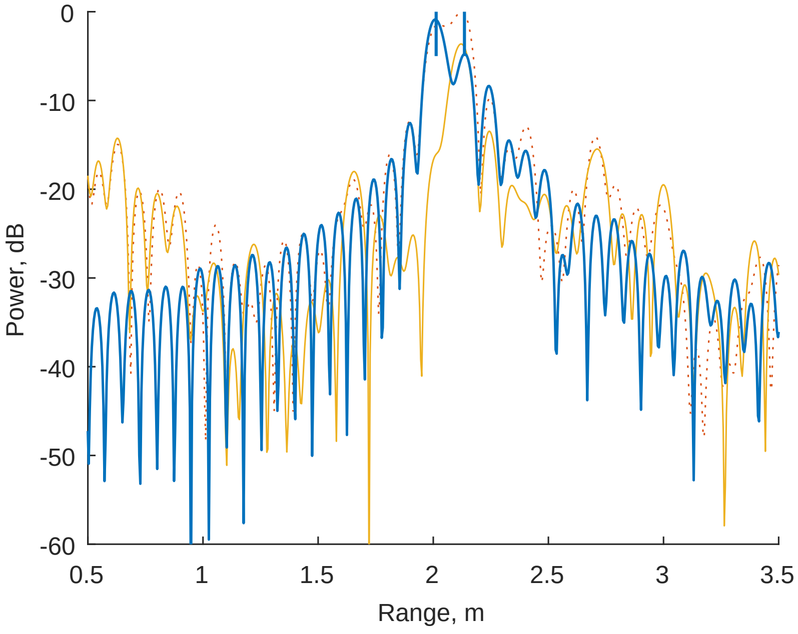

(b) Experiment Ex0

Figure A.15: Target as a point scatterer evaluation. HRRP of representative measurements of two targets separated by 0.12 m. The background is shown as separate lines. Each rod is represented by two scatterers. The second scatterer of the front rod overlaps with the second rod so three peaks in total are observed. The main background scatterer is very close to one of the targets.

Appendix B

Selected algorithms and standard signal processing practices applied

Different good practices for signal processing can be applied to improve the performance of BSCT

B.1 Utilities

Listing B.1: Load RF data from a folder

```
function [ x, seqNo ] = GetFreqResponses( keyword, mode, folder )
%GETFREQRESPONSES Get complex frequency response and file index (e.g. angle)
%   keyword: the name in the filename without the extension
%   mode: 'single' for specific measurement
%         'average' for the mean of multiple measurements
%         'all' for array of measurements
%         'advanced' for better file filtering, output as 'all'
%   seqNo: sequence number of the experiment or number of averaged
%   measurements

if nargin < 3
    folder = '.';
end
if nargin<2
    filename = [keyword, '.txt'];
    seqNo = GetIndex(filename);
    if ~isnan(seqNo)
```

```
        mode = 'single';
    else
        mode = 'all';
    end
end

curdir = cd(folder);

switch mode
    case 'single'
        fnames = GetFilenames(keyword);
        filename = fnames{1};
        x = getFreqResponse(filename);
        seqNo = GetIndex(filename);
    case 'average'
        fnames = GetFilenames( keyword );
        nFiles = length(fnames);
        x = getFreqResponse(fnames{1});
        for i = 2: nFiles
            x = x + getFreqResponse(fnames{i});
        end
        x = x/nFiles;
        seqNo = nFiles; % the number of averaged measurements
    case 'all'
        filenames_wildcard = [keyword, '*.txt'];
        files = dir(filenames_wildcard);
        nFiles = length(files);
        x1 = getFreqResponse(files(1).name);
        nSamples = length(x1);
        x = zeros(nSamples, nFiles);
        seqNo = zeros(1, nFiles);
        x(:,1) = x1;
        seqNo(1) = GetIndex(files(1).name);
        for i = 2: nFiles
            x(:,i) = getFreqResponse(files(i).name);
            seqNo(i) = GetIndex(files(i).name);
        end
    case 'advanced'
        fnames = GetFilenames( keyword );
        nFiles = length(fnames);
        x1 = getFreqResponse(fnames{1});
        seqNo = zeros(1, nFiles);
        nSamples = length(x1);
        x = zeros(nSamples, nFiles);
        x(:,1) = x1;
        seqNo(1) = GetIndex(fnames{1});
        for i = 2: nFiles
            x(:,i) = getFreqResponse(fnames{i});
            seqNo(i) = GetIndex(fnames{i});
        end
    otherwise
            error('mode should be single, average or all')
end

[seqNo, I] = sort(seqNo);
x = x(:,I);
```

```

cd(curdir)
end

function fnames = GetFilenames( keyword )
    files = dir([keyword, '*.txt']);
    regex_filter = [keyword, '\d*.txt'];
    fnames = {files.name}.';
    FIND = @(str) cellfun(@(c) ~isempty(c), regexp(fnames, str, 'once'));
    fnames = fnames(FIND(regex_filter));
end

function angle_deg = GetIndex(filename)
    angle_string = regexp(filename, '(\d+).txt$', 'tokens');
    angle_deg = str2double([angle_string{:}]);
end
```

Listing B.2: Get ultrasound measurements

```
%% Set experiment
pause(30);
numSeparatedMeasurements = 5;
pause_duration = 1;

set_scp.fs = 10e6;
set_scp.N = 100e3;
set_scp.ch_range = [2, 0.8];

set_gen.fs = set_scp.fs;
set_gen.gen_amplitude = 0.1;
set_gen.burst_count = 1;

set_signal.f1 = 100e3;
set_signal.f2 = 35e3;
set_signal.T = 0.002;

set_target.type = 'rods_double'; % phantom
set_target.param = struct();
set_target.param.centre = false;
set_target.param.loc = 0.025;

set_turntable.on = true;
set_turntable.step = 2;
set_turntable.velocity = set_turntable.step/5;
set_turntable.acceleration = 2;


trigerer = 2; % 0:gen, 1:ch1, 2:ch2
note = 'max dist';

s = genWaveform(set_gen.fs, set_signal.f1, set_signal.f2,...
    set_signal.T, @chirp, set_gen.fs*set_signal.T*2, 0 );
set_gen.waveform = s;

plot(s)
```

```

delays_low = (0:5:50)*1e-6;
delays_medium = (60:20:200)*1e-6;
delays_large = (250:50:600)*1e-6;
delays = [delays_low, delays_medium, delays_large];
angles = 0:set_turntable.step:360;

%% Set TiePie

LibTiePieNeeded
[scp, gen] = InitializeTiePie(LibTiePie);
gen = SetGen(gen, set_gen);
scp = SetSCP(scp, set_scp);
scp = SetTriger(scp, trigerer);

%% Set Turntable

h = SetTurntable(set_turntable);

%% Fire!
gen.OutputOn = true;
gen.setData(s)

if strcmpi(set_target.type,'phantom')
    params = delays;
else
    params = angles;
end

for param = params
    % prepare waveform
    if strcmpi(set_target.type,'phantom')
        set_target.param.tau = param;
        delay_samples = round(param*set_gen.fs);
        sDelayed = delay_seq( s, delay_samples );
        sInterf = s + sDelayed;
        gen.setData(sInterf)
    else
        set_target.param.angle = param;
        command_to_send = sprintf('goto ccw %s', num2str(param));
        fprintf(h, command_to_send);
        pause(5)
    end

    % collect data
    for i = 1:numSeparatedMeasurements
        pause( pause_duration*rand )
        fprintf('at %.1f deg\n', param)
        data = single_measurement( scp, gen );
        tpd = struct( 'data', data, 'set_target', set_target,...
    'set_signal', set_signal, 'set_scp', set_scp, 'set_gen', set_gen, ...
    'trigerer', trigerer, 'seq', i, 'set_turntable', set_turntable, 'note', note);
        save_data(tpd )
    end
end
```

```

%% Everything off

gen.OutputOn = false;
clear scp
clear gen
fclose(h);
delete(h)
clear h
```

B.2 Target peak localisation algorithm

Target location has to be determined from the output of the receiver. In the context of this work the spacing between the targets was estimated as the location of highest peak in the BSCT spacing profile. The corresponding spacing based on the MF range profile was calculated as the distance between the two highest peaks.

The peak detection algorithms use a set of rules to isolate the most significant peaks from the random fluctuations (Listing B.3). Different settings for selecting up to three targets are shown on Fig. B.1.

- A threshold equal to the mean signal power plus two standard deviations was used in order to suppress the noise (Fig. B.1a).

- The minimal peak prominence to consider it as a separate peak was set to 3 dB (Fig. B.1b, Fig. B.1e).

- A second threshold at -10 dB from the maximal value was introduced to suppress the sidelobes (Fig. B.1b)

The localisation in its simplest form is just scaling the index of the sample having higher value than its neighbours. The index based target range estimate can be improved by fitting different curves to the samples. Such algorithms are discussed in [117, Sec.

Listing B.3: Peak detection algorithm

```
function [plocs, pmags] = get_peaks( s, npks, sortStr, th_dB )
%GET_PEAKS Find the index and the magnitude of the peaks
%   above a noise and sidelobes defined thresholds
%   s - input signal vector, NOT in dB
%   npks - max number of peaks to return
%   sortStr - boolean
%   th_dB - distance between the threshold and the max value, in dB

    s_db = db(s);
    thresh1 = db(2*std((s))+mean((s)));
    thresh2 = max(s_db) - th_dB;
    thresh = max(thresh1, thresh2);

    [~, plocs] = findpeaks(s_db, ...
        'MinPeakProminence', 3,...
        'MinPeakHeight', thresh,...
        'NPeaks', npks,...
        'SortStr', sortStr);

    pmags = s(plocs);
end
```

13.15]. The one used in the thesis was parabolic interpolation of the absolute values of the signal

$$m_k = m_k + 0.5\frac{|s(m_{k+1})| - |s(m_{k-1})|}{2|s(m_k)| - |s(m_{k+1})| - |s(m_{k-1})|} \tag{B.1}$$

The implementation of (B.1) is given in Listing B.4.

Interpolation provides a simple way to surpass the limitation of the accuracy imposed by the sampling interval, i.e. when the true location is located somewhere between the samples (Fig. B.1c). Similar effect can be achieve by reducing the sampling interval to the desired accuracy but creating range profiles with more points is more computationally expensive. The effect of interpolation is obvious on Fig. B.2 - the step transition of the estimates around the true values (Fig. B.2a) is smoothed (Fig. B.2b).

Listing B.4: Interpolate peak values using parabolic interpolation

```
function [iploc, ipmag] = peak_interp(s, plocs)
%PEAK_INTERP Interpolate peak values using parabolic interpolation
%   Based on SMS Tools by Xavier Serra
%   https://github.com/MTG/sms-tools/blob/master/software/models/
   utilFunctions.py
%   More advanced algorithms in Lyon, Sec. 13.15 Spectral peak location
%   algorithms
%
%   s: processor output vector,
%   ploc: locations of peaks vector
%
%   iploc, ipmag: interpolated peak locations and magnitudes

    val = abs(s(plocs));              % magnitude of peak bin
    lval = abs(s(plocs-1));           % magnitude of bin at left
    rval = abs(s(plocs+1));           % magnitude of bin at right
    iploc = plocs + 0.5*(lval-rval)./(lval-2*val+rval); % center of parabola
    ipmag = val - 0.25*(lval-rval).*(iploc-plocs);      % magnitude of peaks
end
```

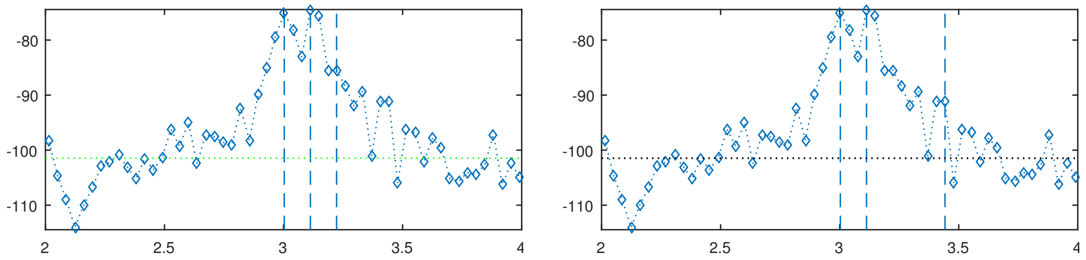

(a) Noise threshold (b) At least 3 dB prominence

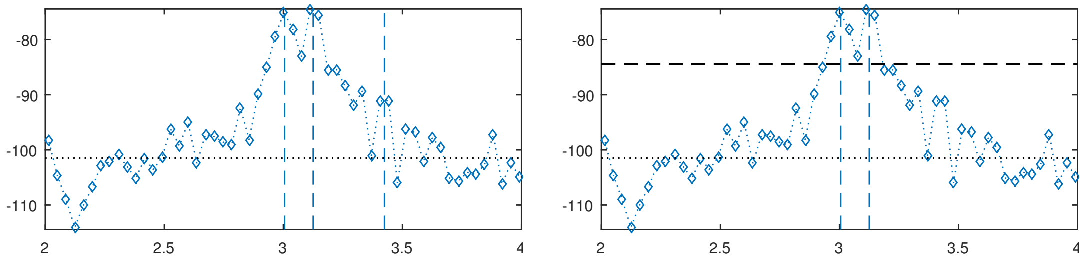

(c) With interpolation (d) Sidelobe supression threshold

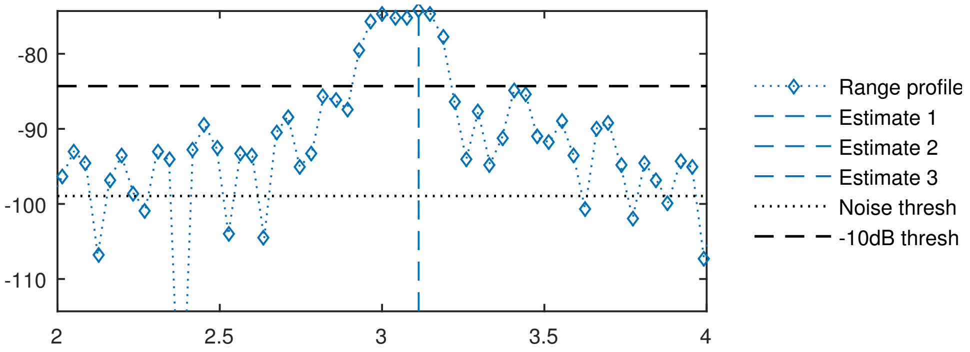

(e) Reduced bandwidth

Figure B.1: Localisation of the three strongest peaks of a signal

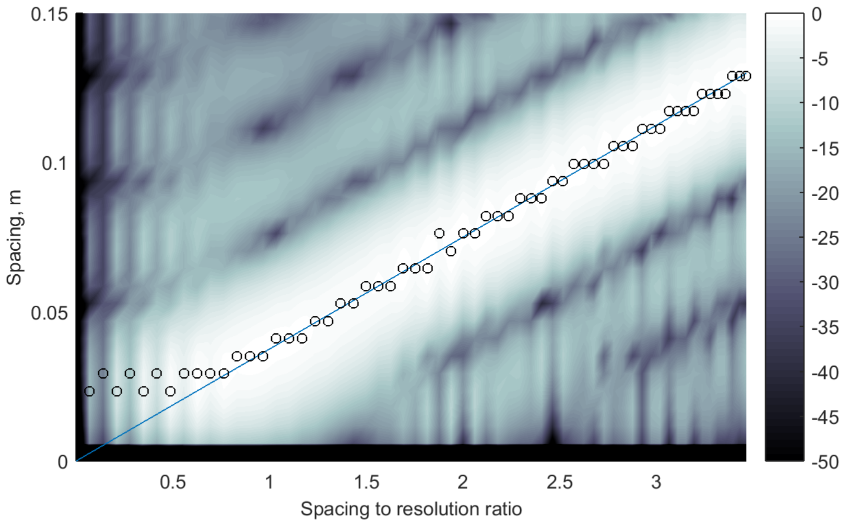

(a) no interpolation

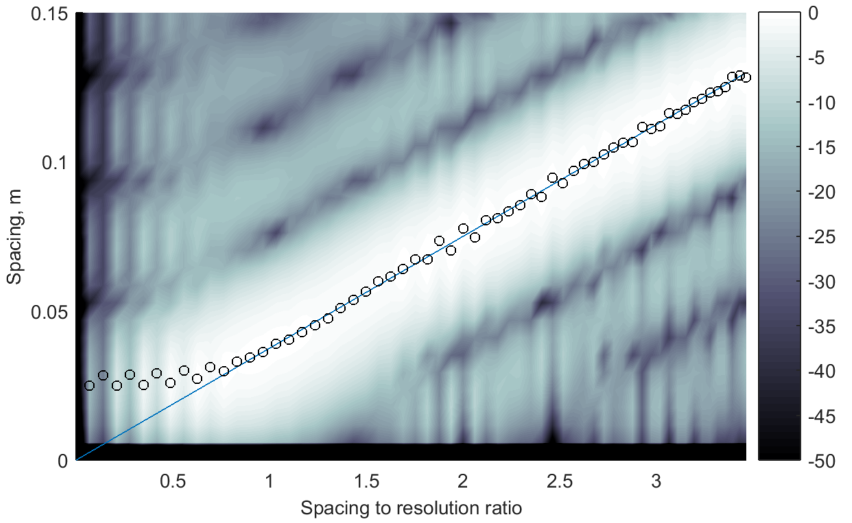

(b) interpolated peak locations

Figure B.2: Peak locations fitted over simulated spacing profiles with and without interpolation. The true location of the target is denoted by the diagonal line

B.3 Estimation of the target frequency response

The spectrum of the target has to be insulated from the spectrum of the environment. This operation involve restricting the return signal to a short range around the target (Sec. 6.2). Even though trivial, this operation degrades the available bandwidth to some extent as the lowest and highest frequencies are skewed. The output of different approaches are shown on Fig. B.3. Simple discarding of all data outside the range interval in time domain in this example leads to increase of the power of lower frequencies and decrease for the higher frequencies – the amplitudes are shifting towards a common value as sampling leads to a periodic signal. Zero padding skews the spectrum in the other direction. In total about 100 MHz of the total 4 GHz are affected.

Improvement in the frequency response estimation can be achieved using the Papoulis-Gerchberg spectrum extrapolation technique [107, 108]. Our implementation is provided in the Listing B.5. The resulting curve follows the expected sinusoidal pattern with less distortions (Fig. B.3). The spectral analysis of the target is out of the scope of this research. Interesting questions as which algorithm best estimates the zeroes locations, which are more robust to strong scatterers outside the window, etc. will not be investigated. Only the simplest range restriction algorithm will be used, i.e. zeroing all samples outside preselected range around the target scatterers.

Listing B.5: Target range gating

```
function S_gated = RestrictRange(S, range_window, DeltaF, mode)
%RESTRICTRANGE Isolate the frequency response of the targets
% S_gated in selected range window
%   RestrictRange( S, range_window, DeltaF, mode )
%   S - full response, frequency domain
%   range_window: range boundaries in meters, e.g. [1, 5]
%   DeltaF: sampling step in frequency
%   mode: 'none' - do nothing
%         'crop' - window in time domain
%         'trim' - zero pad in freq. and window in time domain
%         'filter' - filter the frequency response
%         'papoulis' - extrapolate response, 100 iterations

c = 3e8; % speed of light, m/s
range_window_sec = 2*range_window/c;
N = length(S);

switch mode
    case 'none'
        S_gated = S;
    case 'filter'
        fc = range_window_sec*DeltaF*2;
        [b,a]=butter(2,fc, 'bandpass');
        S_gated = filtfilt(b, a, S);
    case 'crop'
        s = ifft(S);
        deltaT = 1/(N*DeltaF);
        index1 = floor(range_window_sec(1)/deltaT);
        index2 = ceil(range_window_sec(2)/deltaT);
        s(1:index1,:) = 0;
        s(index2:N,:) = 0;
        S_gated = fft(s);
    case 'trim'
        NN = 2*N;
        s = ifft(S, NN);
        deltaT = 1/(NN*DeltaF);
        index1 = floor(range_window_sec(1)/deltaT);
        index2 = ceil(range_window_sec(2)/deltaT);
        s(1:index1,:) = 0;
        s(index2:NN,:) = 0;
        S_gated = fft(s, NN);
        S_gated = S_gated(1:N);
    case 'papoulis'
        NN = 2*N;
        s = ifft(S, NN);
        deltaT = 1/(NN*DeltaF);
        index1 = floor(range_window_sec(1)/deltaT);
        index2 = ceil(range_window_sec(2)/deltaT);
        S_gated = fft(s, NN);
        for i = 1:100
            S_gated(1:N,:) = S;
            s = ifft(S_gated);
            s(1:index1,:) = 0;
            s(index2:NN,:) = 0;
            S_gated = fft(s, NN);
        end
        S_gated = S_gated(1:N,:);
end
```

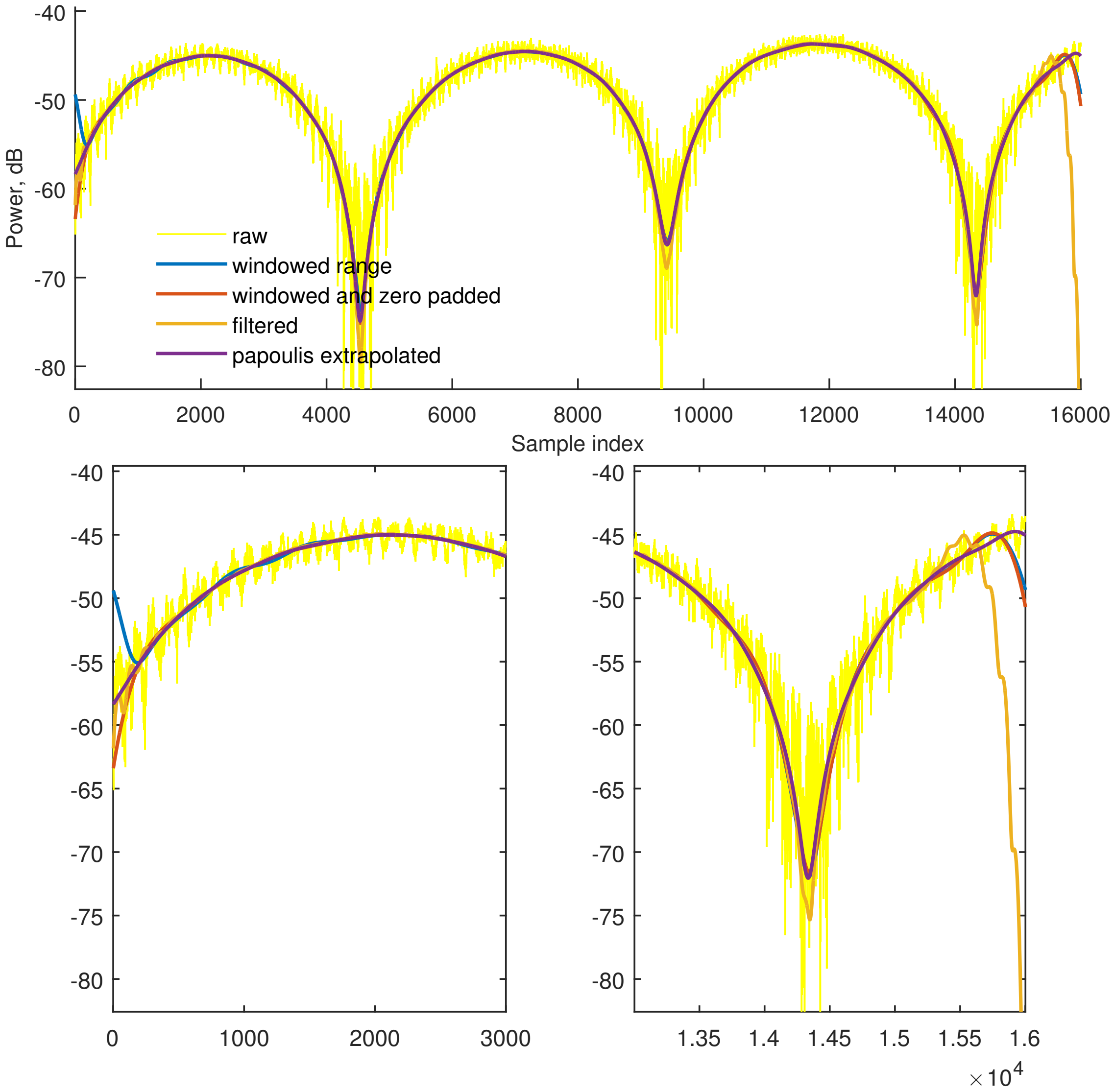

Figure B.3: Target interference pattern and increased frequency response error close to the band limits. Different algorithms for truncating the signal in range provide different skewing.

B.4 Discrete axes scale

Discrete axis scaling to frequency, time or range Digital signal processing transform sequences of numbers. Real signals are continuous functions of time, range, frequency or angle. While the sampling theory is well developed and mature subject it still worth paying special attention to the implementation details.

The relationship for switching from a measurement sample index to frequency or time/range scale is simple:

$$x = \Delta_x \cdot n + x_1 \tag{B.2}$$

where Δ_x is the discrete step in physical units and n is the index sequence starting from zero and having N values. The starting point on the x-axis x_1 can be anywhere but normally it is either zero or it centres the signal around the zero. Example implementation is provided in Listing B.6, where the input parameters are the step Δ_x and the shift x_1.

Listing B.6: Scale frequency axis from sample index to Hz/s/m

```
function x = ScaleX( N, deltaX, x1 )
%SCALEX Generate a scale for the abscissa
%   N: number of points of the signal
%   deltaX: the step between the points, Hz, s, m, rad,
%   x1: the x value of the first point

    if nargin < 3
        x1 = -floor(N/2)*deltaX;
    end

    if nargin < 2
        deltaX = 1; % just a sample index
    end

    n = 0:N-1;
    x = n*deltaX + x1;

end
```

Scaling the X axis of the FFT pair A function is provided for calculation of the x-axis points in the pair domain directly from the number of points N and the sampling interval Δ from the original domain. If the period of the transformed signal is T, the sequence is normally presented in one of the following intervals:

- zero starting [0, T), e.g. the output of FFT of complex signal is from 0 to $f_s - \Delta_F$;
- positive, half [0, T/2], e.g. the output of FFT of real signal is from 0 to $f_s/2$;
- zero centred, [-T/2, T/2), e.g. the output of cross correlation or for ‘fftshift’-ed FFT.

Listing B.7: Scaling the X-axis of the FFT pair

```
function [xT, deltaT] = ScalePairX( N, DeltaX, mode, dim )
%SCALEX Generate a scale for the FFT pair abscissa
%   N: the total number of points, including any zero padding
%   DeltaX: the step between the points
%   mode:
%        'none', zero start, [0, T) or (0:N-1)*deltaT
%        'half', half of the points, [0, T/2], (0:N/2)*deltaT
%        'full', zero centred, [-T/2, T/2)
%   dim: the scale used, from {'Hz', 'm', 's', 'index', 'cycle'}
%
%   deltaT: the step in the pair domain
%
%   example: ScalePairX(4, 1, 'full') --> [-0.50, -0.25, 0, 0.25]
%   example: ScalePairX(4, 1/4, 'full') --> [-2, -1, 0, 1]
%   example: ScalePairX(8, 1/4, 'half') --> [0, 0.5, 1, 1.5, 2]

    switch dim
        case 's', 'Hz';
            C = 1;
        case 'm'
            C = 3e8/2;
    end

    deltaT = C*1/(N*DeltaX);
    N_halved = floor(N/2);

    if strcmpi(mode, 'none')
        xT = (0:N-1)*deltaT;
    elseif strcmpi(mode, 'half')
        xT = (0:N_halved)*deltaT;
    elseif strcmpi(mode, 'full')
        xT = (-N_halved:N_halved-1)*deltaT;
    end
end
```

The sampling interval Δ_T in the pair domain is calculated as

$$\Delta_{\mathrm{T}} = \frac{K}{N \cdot F} = \frac{1}{N \cdot \Delta_F} \tag{B.3}$$

where K is the number of samples in the original signal (e.g. points in the frequency profile), N is the zero padded signal length, F is the duration of the original signal in the corresponding physical dimension (e.g. signal bandwidth in Hz) and Δ_F is the sampling interval for the original signal.

Listing B.8: Auxiliary relationships for switching the domain

```
function deltaX = DeltaX( K, spanF, N )
%DELTAX Sampling interval of the Fourier-transform pair
%   K: number of samples
%   N: number of points after zero padding
%   spanF: signal duration/bandwidth

        deltaX = (K / N) * (1 / spanF);

end

function spanX = SpanX( N, deltaX )
%SPANX Calculate signal duration/bandwidth

        spanX = N*deltaX;

end
```

Y axis scaling

Switching from sinusoidal amplitudes to spectral density The spectral density describe how much signal amplitude is present per unit of bandwidth [118]. Therefore each sinusoidal amplitude should be divided by the bandwidth it represents. For constant sampling rate of one and complex representation this bandwidth is $\frac{1}{K}$, where K is again the number of available data points. The spectral density becomes K times the amplitude of the sinusoid.

Scaling after IFFT The spectral density magnitude in the frequency domain has dimension expressed per unit bandwidth. To preserve the Parseval's theorem, the output of the IFFT need to be scaled appropriately.

$$\Delta_T \sum_{i=1}^{M} |s_i|^2 = \Delta_F \sum_{k=1}^{M} |S_k|^2 \tag{B.4}$$

therefore,

$$\mathrm{var}(s) = \frac{\Delta_F}{\Delta_T} \mathrm{var}(S) = \Delta_F B_C \,\mathrm{var}(S) \tag{B.5}$$

$$\begin{aligned} \mathrm{var}(s) &= \Delta_F B_C M \,\mathrm{var}(\mathcal{F}^{-1}(S)) \\ &= B_C^2 \,\mathrm{var}(\mathcal{F}^{-1}(S)) \\ &= \mathrm{var}(B_C \mathcal{F}^{-1}(S)) \end{aligned} \tag{B.6}$$

The scaling constant for the signal after IFFT operation is the sampling frequency B_C:

$$s = B_C \mathcal{F}^{-1}(S) \tag{B.7}$$

B.5 Simulation of the SNR for BSCT

Listing B.9: BSCT SNR simulation

```
M = 160;
m = 0:M−1;

%% Noise
N0 = 10; % Noise power
nt = randn(1,M)∗sqrt(N0); % Noise waveform

%% Signal
A = 50; % Signal amplitude
nPk = 20; % Impulse location
st = zeros(1, M);
st([p+1, M−p+1]) = A; % Signal waveform

%% Signal plus noise
snt = st + nt;

%% BSCT transformation
snf = fft(snt); % Frequency domain representation of the waveform
snf_power = snf.∗conj(snf); % Power spectral density
snf_power_avg = mean(snf_power); % Mean spectral power

snf_bsct = snf_power − snf_power_avg; % BSCT frequency profile
snt_bsct = ifft(snf_bsct);  % BSCT time profile

%% The BSCT noise component
bsct_noise  = snt_bsct;
bsct_noise([2∗p+1, M−2∗p+1]) = nan; % discard signal peaks
bsct_noise_var = var(bsct_noise,'omitnan'); % BSCT noise power

%% The BSCT signal component
bsct_peak  = snt_bsct(2∗p+1);

%% SNR
snr = A^2/N0; % SNR of the waveform
bsct_snr = bsct_peak^2/bsct_noise_var % SNR of BSCT
```

B.6 Simulation of RF measurements data

To run the simulation the power of the signal need to be known.

Listing B.10: Simulate the frequency response of two scatterers in white Gaussian noise

```
function [s, A] = simulateSpectrum(f, d, L, rms_ampl, SNRdb)
% SIMULATESPECTRUM return frequency response of two impulses plus noise (WGN)
%
%    d - distance between the impulses, m
%    f - frequencies axis, cloumn vector
%    L - distance to the first impulse, m
%    rms_ampl - signal rms amplitude
%    SNRdb - noise power in dB

c = 3e8;
tau = 2*d/c;
t1 = 2*L/c;
N = length(f);
rng('shuffle') % shuffle the random numbers!!!

SNR = 10^(SNRdb/10);
cosine_rms = rms_ampl*sqrt(SNR/(SNR+1));
A = sqrt(2)*(cosine_rms);

phase_shift = 0;
s = A*cos(pi*f*tau-phase_shift);
s = exp(-1j*pi*f*tau).*exp(-1j*2*pi*f*t1).*s;

sigma = rms_ampl./sqrt(SNR+1);
mu = 0;

noise_amp = normrnd(mu, sigma, N, length(d))*sqrt(N/2);
noise_phase = (2*rand(N,length(d)) - 1) * pi;
noise = noise_amp.*exp(-1j*noise_phase);
s = s + noise;
```

Appendix C

Datasets and data structures

C.1 Ultrasound measurements dataset

An experiment was set to measure the distance between two closely spaced objects with ultrasound.

In order to be able to explore the characteristics of both the target and the environment, multiple experiments were performed (Table C.1). Measurements were performed at three different positions of the turntable, designated based on the distance to the emitter/receiver as L (low, experiment #5), M (medium, experiments #1 to #4)) and H (high, experiments #6 to #13). In part of the experiments one of the rods was positioned in the centre so it should not be influenced by the angular position of the turntable (#1 to #9). The non-centred rod was positioned at 25, 50, 75 mm of the centre. This way the distance between the rods was varied from 25 mm to 150 mm.

Each rod arrangement was observed from multiple perspectives at constant step (0.5, 1, 2 or 5 degrees) covering the whole 360^0 diapason. Each individual measurement was repeated five times.

Table C.1: Ultrasound experiment settings

Id #	N targets	Distance	Radius mm	Central rod	Step deg	Note
1	2	M	75	Y	0.5	1
2	2	M	50	Y	0.5	1
3	2	M	50	Y	0.5	1
4	2	M	50	Y	0.5	2
5	2	L	50	Y	0.5	
6	2	H	75	Y	0.5	
7	1	H	0	Y	1	
8	2	H	25	Y	0.5	
9	2	H	50	Y	1	
10	0	H	–	–	–	
11	1	H	75	N	1	
12	2	H	75	N	5	
13	2	H	25	N	2	

Notes: 1 – high vibrations, 2 – turntable moved sideway

C.2 Radio-frequency measurements dataset

The experiment data are organised into folders. Each experiment has its own folder with all collected measurements. In addition to the measurement files the experiment folder contains a file named ‘setup.m’ with all important parameters of the measurement – the VNA settings, target parameters and file naming conventions. Short description of these parameters is provided in Table C.2.

Each measurement file contains a list of numbers. The odd sequence numbers represent frequency magnitudes in dB. The even sequence numbers represent the phases in degrees. The name of the file consists of a keyword, a number and an extension ‘.txt’. The keyword is used to discriminate the measurements in the folder, e.g. background, single plate, two plates. The number either encodes the position of the turntable or is a simple sequence number for multiple measurements of fixed target. A script for loading the text files produced by VNA and LabView into Matlab array of complex numbers is provided in Listing B.1.

The main characteristics of the experiments are summarized in Table C.3. The last three columns give the number of measurements of the background, of two targets at fixed spacing and of single target respectively.

Table C.2: RF experiments, variables in the setup.m file

Variable	Dim	Description	Subject	Application
id	label	Experiment ID	Code	Naming of output files
DeltaF	Hz	Frequency step, Δ_F	VNA	Scale axis
f1	Hz	Lower frequency, f_1	VNA	Scale axis
ifbw	Hz	Intermediate Frequency Bandwidth	VNA	Noise estimates
target	label	Two scatterers measurements	Code	Load measurements
targetC	label	Single scatterer measurements	Code	Load measurements
bckgr	label	Background measurements	Code	Load measurements
turntable_centre[1]	m	Turntable range	Target	Ground true
fix_deg[1]	deg	Zero angle correction	Target	Ground true
R[1]	m	Target to turntable centre	Target	Ground true
locs_m[2]	m	True ranges	Target	Ground true
d[2]	m	True spacing	Target	Ground true
targetRange	m	Range to consider	Code	Processed window
c	m/s	Speed of light	Constant	

[1] – applicable for targets on turntable

[2] – applicable for fixed targets

Table C.3: List of RF experiments with parameters

ID	f1 GHz	Bc GHz	Δ_F kHz	K \#	IFBW Hz	L1[1] m	d[2] m	Bgr \#	Two \#	One \#
Plate, separate column supports										
Ex1	13	2	250	8001	100k	3.075	0.289	10	10	10
Ex2	13	2	250	8001	100k	3.071	0.288	10	10	10
Ex3	13	4	250	16001	100k	3.068	0.285	10	10	10
Ex4	13	4	250	16001	100k	3.065	0.124	10	10	10
Ex5	13	4	250	16001	100k	3.035	-	5	0	5
Ex5K	13	4	250	16001	100k	3.030	-	5	0	5
Plates, shared table support										
Ex10	13	4	250	16001	2k	3.100	0.111	4	10	0
Ex11	13	4	250	16001	2k	3.089	0.122	1	5	0
Ex12	13	4	1000	4001	0.5k	3.089	0.122	10	10	0
Rods										
Ex0	10	2	500	4001	1k	2.074	var	2	1	1
Ex6	13	4	250	16001	100k	3.14	var	10	1	10
Ex8	13	4	250	16001	100k	3.063	var	10	1	0
Spheres										
Ex9D	13	4	250	16001	2k	3.055	var	10	1	10
Ex9C	13	4	250	16001	10k	3.055	var	10	1	5
Ex9	13	4	250	16001	100k	3.055	var	5	1	0
Ex9B	13	4	250	16001	300k	3.055	var	10	1	10

[1] – distance from the antenna to the closest plate or to the turntable centre

[2] – applicable for two scatterers measurements

Table C.4: List of RF experiments with noise estimates

ID	N0 dB/Hz	Noise dB	Bckgr dB	Signal dB	SNR dB
Plate, separate column supports					
Ex1	-59.4	87.6	99.6	113.8	26.2
Ex2	-59.5	87.5	100.0	135.2	47.7
Ex3	-59.3	90.7	102.1	137.3	46.7
Ex4	-59.3	90.7	102.6	141.2	50.5
Ex5	-59.3	90.7	102.4	144.7	54.0
Ex5K	-59.3	90.7	102.4	145.0	54.3
Plates, shared table support					
Ex10	-76.0	74.0	123.8	144.5	70.4
Ex11	-76.1	73.9	123.8	143.9	70.0
Ex12	-82.1	73.9	124.1	143.9	70.0
Rods, two at angle 36					
Ex0	-79.8	70.2	113.4	121.9	51.7
Ex6	-59.3	90.7	124.1	112.1	21.4
Ex8	-59.3	90.7	140.7	121.7	31.1
Sphere, single					
Ex9D	-76.1	73.9	141.2	110.7	36.8
Ex9C	-69.2	80.8	141.2	110.7	29.9
Ex9	-59.6	90.4	141.2	110.0	19.5
Ex9B	-55.1	94.9	141.2	110.7	15.8

Note: the signal in time domain is scaled by its bandwidth

References

[1] A. W. Rihaczek, *Principles of high-resolution radar*. New York: McGraw-Hill, 1969.

[2] D. Blacknell and H. D. Griffiths, eds., *Radar Automatic Target Recognition (ATR) and Non-Cooperative Target Recognition (NCTR)*. Stevenage, UK: Institution of Engineering and Technology, 2013.

[3] H. D. Griffiths, C. J. Baker, and D. Adamy, *Stimson's Introduction to Airborne Radar*. Stevenage, UK: Institution of Engineering and Technology, 3rd edition ed., 2014.

[4] D. von Helversen, "Object classification by echolocation in nectar feeding bats: size-independent generalization of shape.," *Journal of comparative physiology. A, Neuroethology, sensory, neural, and behavioral physiology*, vol. 190, pp. 515–21, 7 2004.

[5] A. Balleri, H. D. Griffiths, C. J. Baker, K. Woodbridge, and M. W. Holderied, "Analysis of acoustic echoes from a bat-pollinated plant species: Insight into strategies for radar and sonar target classification," *IET Radar, Sonar and Navigation*, vol. 6, no. 6, pp. 536–544, 2012.

[6] I. Geipel, K. Jung, and E. K. V. Kalko, “Perception of silent and motionless prey on vegetation by echolocation in the gleaning bat micronycteris microtis,” *Proceedings of the Royal Society of London B: Biological Sciences*, vol. 280, no. 1754, 2013.

[7] C. J. Baker, G. E. Smith, A. Balleri, M. Holderied, and H. D. Griffiths, “Biomimetic echolocation with application to radar and sonar sensing,” *Proceedings of the IEEE*, vol. 102, no. 4, pp. 447–458, 2014.

[8] C. J. Baker, H. D. Griffiths, and A. Balleri, “Biologically inspired waveform diversity,” in *Waveform Design and Diversity for Advanced Radar Systems* (F. Gini, A. De Maio, and L. Patton, eds.), vol. 22 of *Radar, Sonar, Navigation and Avionics*, ch. 6, pp. 149–172, Institution of Engineering and Technology, 2012.

[9] J. R. Barchi, J. M. Knowles, and J. A. Simmons, “Spatial memory and stereotypy of flight paths by big brown bats in cluttered surroundings,” *Journal of Experimental Biology*, vol. 216, no. 6, pp. 1053–1063, 2013.

[10] N. Levanon and E. Mozeson, *Radar signals*. IEEE Press; Hoboken, NJ; Wiley-Interscience, 2004.

[11] P. M. Woodward, *Probability and information theory, with applications to radar*. London, England: Pergamon Press, 1953.

[12] C. E. Cook and M. Bernfeld, *Radar Signals: An Introduction to Theory and Application*. New York: Academic Press, 1967.

[13] P. A. Saillant, J. A. Simmons, S. P. Dear, and T. A. McMullen, “A computational model of echo processing and acoustic imaging in frequency-modulated echolocat-

ing bats: The spectrogram correlation and transformation receiver," *The Journal of the Acoustical Society of America*, vol. 94, pp. 2691–2712, 11 1993.

[14] I. Matsuo, K. Kunugiyama, and M. Yano, "An echolocation model for range discrimination of multiple closely spaced objects: transformation of spectrogram into the reflected intensity distribution," *The Journal of the Acoustical Society of America*, vol. 115, pp. 920–928, 2 2004.

[15] L. Wiegrebe, "An autocorrelation model of bat sonar," *Biological cybernetics*, vol. 98, no. 6, pp. 587–595, 2008.

[16] J. D. Altringham, *Bats : biology and behaviour*. Oxford University Press, 1996.

[17] G. D. Pollak and J. H. Casseday, *The Neural Basis of Echolocation in Bats*. Berlin, Heidelberg: Springer Berlin Heidelberg, 1989.

[18] A. N. Popper and R. R. Fay, eds., *Hearing by Bats*. New York, NY: Springer New York, 1995.

[19] M. Vater and M. Kössl, "Comparative aspects of cochlear functional organization in mammals," *Hearing Research*, vol. 273, no. 1–2, pp. 89 – 99, 2011. Comparative Studies of the Ear.

[20] M. Kössl, J. Hechavarria, C. Voss, M. Schaefer, and M. Vater, "Bat auditory cortex – model for general mammalian auditory computation or special design solution for active time perception?," *European Journal of Neuroscience*, vol. 41, no. 5, pp. 518–532, 2015.

[21] J. Simmons, M. Fenton, and M. O'Farrell, "Echolocation and pursuit of prey by bats," *Science*, vol. 203, no. 4375, pp. 16–21, 1979.

[22] M. E. Bates, J. A. Simmons, and T. V. Zorikov, "Bats use echo harmonic structure to distinguish their targets from background clutter.," *Science (New York, N.Y.)*, vol. 333, pp. 627–30, 7 2011.

[23] J. A. Simmons, "The resolution of target range by echolocating bats," *The Journal of the Acoustical Society of America*, vol. 54, no. 1, pp. 157–173, 1973.

[24] A. Boonman and J. Ostwald, "A modeling approach to explain pulse design in bats," *Biological cybernetics*, vol. 97, pp. 159–172, 8 2007.

[25] J. Simmons, "Perception of echo phase information in bat sonar," *Science*, vol. 204, no. 4399, pp. 1336–1338, 1979.

[26] C. F. Moss and H. U. Schnitzler, "Accuracy of target ranging in echolocating bats: acoustic information processing," *Journal of Comparative Physiology A*, vol. 165, no. 3, pp. 383–393, 1989.

[27] D. Menne, I. Kaipf, I. Wagner, J. Ostwald, and H. Schnitzler, "Range estimation by echolocation in the bat eptesicus fuscus: Trading of phase versus time cues," *The Journal of the Acoustical Society of America*, vol. 85, no. 6, pp. 2642–2650, 1989.

[28] J. A. Simmons, M. Ferragamo, C. F. Moss, S. B. Stevenson, and R. A. Altes, "Discrimination of jittered sonar echoes by the echolocating bat, eptesicus fuscus: The shape of target images in echolocation," *Journal of Comparative Physiology A*, vol. 167, pp. 589–616, 11 1990.

[29] J. A. Simmons, P. A. Saillant, J. M. Wotton, T. Haresign, M. J. Ferragamo, and C. F. Moss, "Composition of biosonar images for target recognition by echolocating bats," *Neural Networks*, vol. 8, no. 7-8, pp. 1239–1261, 1995.

[30] S. Schmidt, “Perception of structured phantom targets in the echolocating bat, megadermalyra,” *The Journal of the Acoustical Society of America*, vol. 91, no. 4, pp. 2203–2223, 1992.

[31] J. M. Wotton, M. J. Ferragamo, and M. I. Sanderson, “The emergence of temporal hyperacuity from widely tuned cell populations,” *Network: Computation in Neural Systems*, vol. 15, no. 3, pp. 159–177, 2004.

[32] A. W. Rihaczek, “Radar resolution of ideal point scatterers,” *IEEE Transactions on Aerospace and Electronic Systems*, vol. 32, pp. 842–845, April 1996.

[33] R. Simon, M. Knörnschild, M. Tschapka, A. Schneider, N. Passauer, E. K. V. Kalko, and O. von Helversen, “Biosonar resolving power: echo-acoustic perception of surface structures in the submillimeter range.,” *Frontiers in physiology*, vol. 5, p. 64, 1 2014.

[34] J. A. Simmons, C. F. Moss, and M. Ferragamo, “Convergence of temporal and spectral information into acoustic images of complex sonar targets perceived by the echolocating bat, eptesicus fuscus,” *Journal of Comparative Physiology - A Sensory, Neural, and Behavioral Physiology*, vol. 166, no. 4, pp. 449–470, 1990.

[35] J. A. Simmons, M. J. Ferragamo, and C. F. Moss, “Echo-delay resolution in sonar images of the big brown bat, eptesicus fuscus,” *Proceedings of the National Academy of Sciences*, vol. 95, pp. 12647–12652, 10 1998.

[36] J. A. Simmons, E. G. Freedman, S. B. Stevenson, L. Chen, and T. J. Wohlgenant, “Clutter interference and the integration time of echoes in the echolocating bat, eptesicusfuscus,” *The Journal of the Acoustical Society of America*, vol. 86, no. 4, pp. 1318–1332, 1989.

[37] M. E. Bates and J. A. Simmons, “Perception of echo delay is disrupted by small temporal misalignment of echo harmonics in bat sonar,” *The Journal of experimental biology*, vol. 214, no. 3, pp. 394–401, 2011.

[38] J. A. Simmons and J. E. Gaudette, “Biosonar echo processing by frequency-modulated bats,” *IET Radar, Sonar and Navigation*, vol. 6, no. 6, pp. 556–565, 2012.

[39] J.-E. Grunwald, S. Schörnich, and L. Wiegrebe, “Classification of natural textures in echolocation,” *Proceedings of the National Academy of Sciences of the United States of America*, vol. 101, no. 15, pp. 5670–5674, 2003.

[40] U. Firzlaff, S. Schörnich, S. Hoffmann, G. Schuller, and L. Wiegrebe, “A neural correlate of stochastic echo imaging,” *Journal of Neuroscience*, vol. 26, no. 3, pp. 785–791, 2006.

[41] S. Schörnich, *Time Domain Echo Analysis in the Bat Phyllostomus Discolor*. PhD thesis, Ludwig-Maximilians-Universität München, 2 2008.

[42] S. Schörnich and L. Wiegrebe, “Phase sensitivity in bat sonar revisited,” *Journal of comparative physiology.A, Neuroethology, sensory, neural, and behavioral physiology*, vol. 194, pp. 61–67, 1 2008.

[43] D. Vanderelst, J. Steckel, A. Boen, H. Peremans, and M. W. Holderied, “Place recognition using batlike sonar,” *eLife*, vol. 5, p. e14188, aug 2016.

[44] R. D. Patterson, K. Robinson, J. Holdsworth, D. Mckeown, C. Zhang, and M. Allerhand, “Complex sounds and auditory images,” in *in Proc. 9th Int. Symp. Hearing Audit., Physiol. Perception*, pp. 429–446, 1992.

[45] R. D. Patterson, M. H. Allerhand, and C. Giguère, “Time-domain modeling of peripheral auditory processing: a modular architecture and a software platform.,” *The Journal of the Acoustical Society of America*, vol. 98, pp. 1890–4, 10 1995.

[46] R. Meddis, “Auditory-nerve first-spike latency and auditory absolute threshold: A computer model,” *The Journal of the Acoustical Society of America*, vol. 119, no. 1, pp. 406–417, 2006.

[47] H. Peremans and J. Hallam, “The spectrogram correlation and transformation receiver, revisited,” *The Journal of the Acoustical Society of America*, vol. 104, no. 2, pp. 1101–1110, 1998.

[48] M. Park and R. Allen, “Pattern-matching analysis of fine echo delays by the spectrogram correlation and transformation receiver,” *The Journal of the Acoustical Society of America*, vol. 128, no. 3, pp. 1490–1500, 2010.

[49] M. I. Sanderson, N. Neretti, N. Intrator, and J. A. Simmons, “Evaluation of an auditory model for echo delay accuracy in wideband biosonar.,” *The Journal of the Acoustical Society of America*, vol. 114, pp. 1648–59, 9 2003.

[50] N. Neretti, M. I. Sanderson, N. Intrator, and J. A. Simmons, “Time-frequency model for echo-delay resolution in wideband biosonar,” *The Journal of the Acoustical Society of America*, vol. 113, no. 4, pp. 2137–2145, 2003.

[51] B. Fontaine and H. Peremans, “Bat echolocation processing using first-spike latency coding,” *Neural Networks*, vol. 22, no. 10, pp. 1372–1382, 2009.

[52] K. T. Loncich, *A biologically inspired model of bat echolocation in a cluttered environment with inputs designed from field Recordings*. PhD thesis, Boston College, 11 2014.

[53] M. I. Sanderson and J. A. Simmons, "Neural responses to overlapping FM sounds in the inferior colliculus of echolocating bats.," *Journal of neurophysiology*, vol. 83, pp. 1840–55, 4 2000.

[54] J. Reijniers and H. Peremans, "On population encoding and decoding of auditory information for bat echolocation," *Biological cybernetics*, vol. 102, no. 4, pp. 311–326, 2010.

[55] D. Goodman and R. Brette, "The brian simulator," *Frontiers in Neuroscience*, vol. 3, p. 26, 2009.

[56] D. Mountain, D. Anderson, G. Bresnahan, A. Brughera, S. Deligeorges, A. Hubbard, and V. Vajda, "Earlab: A virtual laboratory for auditory experimentation," 2007.

[57] S. Kim, R. Allen, and D. Rowan, "Range dependent characteristics in the head-related transfer functions of a bat-head cast: Part 1. monaural characteristics," *Bioinspiration and Biomimetics*, vol. 7, no. 4, 2012.

[58] S. b. Kim, R. Allen, and D. Rowan, "Range dependent characteristics in the head-related transfer functions of a bat-head cast: Part 2. binaural characteristics," *Bioinspiration and Biomimetics*, vol. 7, no. 4, 2012.

[59] R. Burkard and C. F. Moss, "The brain-stem auditory-evoked response in the big brown bat (eptesicus fuscus) to clicks and frequency-modulated sweeps," *The Journal of the Acoustical Society of America*, vol. 96, no. 2, pp. 801–810, 1994.

[60] J. A. Simmons, "Bats use a neuronally implemented computational acoustic model to form sonar images," *Current Opinion in Neurobiology*, vol. 22, no. 2, pp. 311 – 319, 2012. Neuroethology.

[61] J. A. Simmons, "Temporal binding of neural responses for focused attention in biosonar.," *The Journal of experimental biology*, vol. 217, pp. 2834–43, 8 2014.

[62] M. Warnecke and J. A. Simmons, "Target shape perception and clutter rejection use the same mechanism in bat sonar," *Journal of Comparative Physiology A*, vol. 202, no. 5, pp. 371–379, 2016.

[63] J. A. Simmons, J. Gaudette, and M. Warnecke, "Biosonar inspired signal processing and acoustic imaging from echolocating bats," in *Biologically-Inspired Radar and Sonar: Lessons from Nature* (A. Balleri, H. Griffiths, and C. Baker, eds.), ch. 2, Stevenage, UK: IET, 2017.

[64] I. Matsuo, "A model of range discrimination of multiple objects by using the linear period modulation signal," in *7th European Conference on Noise Control 2008, EURONOISE 2008*, pp. 1703–1708, 2008.

[65] I. Matsuo, "Evaluation of the echolocation model for range estimation of multiple closely spaced objects," *The Journal of the Acoustical Society of America*, vol. 130, no. 2, pp. 1030–1037, 2011.

[66] I. Matsuo, "Echolocation of static and moving objects in two-dimensional space using bat-like frequency-modulation sound," *Frontiers in Physiology*, vol. 4, no. July, p. 149, 2013.

[67] B. Fontaine and H. Peremans, "Determining biosonar images using sparse representations," *The Journal of the Acoustical Society of America*, vol. 125, no. 5, pp. 3052–3059, 2009.

[68] D. A. Hague, J. R. Buck, and I. Bilik, “A deterministic compressive sensing model for bat biosonar,” *The Journal of the Acoustical Society of America*, vol. 132, no. 6, pp. 4041–4052, 2012.

[69] I. E. Dror, M. Zagaeski, and C. F. Moss, “Three-dimensional target recognition via sonar: A neural network model,” *Neural Networks*, vol. 8, no. 1, pp. 149–160, 1995.

[70] Y. Yovel, M. O. Franz, P. Stilz, and H.-U. Schnitzler, “Plant classification from bat-like echolocation signals,” *PLOS Computational Biology*, vol. 4, pp. 1–13, 03 2008.

[71] A. van den Oord, S. Dieleman, H. Zen, K. Simonyan, O. Vinyals, A. Graves, N. Kalchbrenner, A. Senior, and K. Kavukcuoglu, “Wavenet: A generative model for raw audio,” in *Arxiv*, 2016.

[72] M. Vespe, G. Jones, and C. Baker, “Lessons for radar,” *IEEE Signal Processing Magazine*, vol. 26, pp. 65–75, 1 2009.

[73] A. Balleri, K. Woodbridge, C. J. Baker, and M. W. Holderied, “Classification of flowers by bats: comparison with the radar case,” in *2009 International Waveform Diversity and Design Conference, WDD 2009*, vol. Kissimmee,, pp. 1–3, 2009.

[74] L. L. Burton and H. Lai, “Active sonar target imaging and classification system,” in *Detection and Remediation Technologies for Mines and Minelike Targets II*, vol. 3079, pp. 19–33, Society of Photo-Optical Instrumentation Engineers, 1997.

[75] F. Devaud, G. Hayward, and J. J. Soraghan, “P1g-3 evaluation of a bio-inspired range finding algorithm (bira),” in *IEEE Ultrasonics Symposium, 2006*, vol. 1, pp. 1381–1384, 2006.

[76] F. Schillebeeckx, F. D. Mey, D. Vanderelst, and H. Peremans, "Biomimetic sonar: Binaural 3d localization using artificial bat pinnae," *The International Journal of Robotics Research*, vol. 30, no. 8, pp. 975–987, 2011.

[77] J. Reijniers and H. Peremans, "Biomimetic sonar system performing spectrum-based localization," *IEEE Transactions on Robotics*, vol. 23, pp. 1151–1159, Dec 2007.

[78] S. Haykin and M. Moher, *Communication Systems*. John Wiley & Sons, 5th ed., 2010.

[79] P. Stoica and R. Moses, *Spectral Analysis of Signals*. Pearson Prentice Hall, 2005.

[80] J. Browne, "Radar systems now rely on data converters." `http://defenseelectronicsmag.com/systems-amp-subsystems/radar-systems-now-rely-data-converters`, 2013. [Online; accessed 11-July-2017].

[81] T. H. Einstein, "Generation of high resolution radar range profiles and range profile auto-correlation functions using stepped-frequency pulse train," Tech. Rep. ADA149242, Massachusetts Inst of Tech Lexington Lincoln Lab, October 1984.

[82] P. Tait, *Introduction to radar target recognition*. IEE Radar, Sonar and Navigation Series: 18, Stevenage IEE 2005, 2005.

[83] D. Gabor, "Theory of communication. part 1: The analysis of information," *Journal of the Institution of Electrical Engineers - Part III: Radio and Communication Engineering*, vol. 93, pp. 429–441(12), November 1946.

[84] D. O. North, “An analysis of the factors which determine signal/noise discrimination in pulsed-carrier systems,” Tech. Rept. PTR-6C, RCA Laboratorie, Princeton, N. J, June 1943. Reprinted in [85].

[85] D. O. North, “An analysis of the factors which determine signal/noise discrimination in pulsed-carrier systems,” *Proceedings of the IEEE*, vol. 51, pp. 1016–1027, July 1963.

[86] P. W. B.A. and I. D. M. T.R.E., “Xcii. a theory of radar information,” *The London, Edinburgh, and Dublin Philosophical Magazine and Journal of Science*, vol. 41, no. 321, pp. 1001–1017, 1950.

[87] S. M. Bozic, *Digital and Kalman Filtering*. Hodder Arnold, 1979.

[88] N. S. Sharma and J. R. Buck, “A generalized linear filter approach for sonar receivers,” in *2009 IEEE 13th Digital Signal Processing Workshop and 5th IEEE Signal Processing Education Workshop, DSP/SPE 2009*, no. 1, pp. 507–512, 2009.

[89] N. S. Sharma, J. R. Buck, and J. A. Simmons, “Trading detection for resolution in active sonar receivers,” *The Journal of the Acoustical Society of America*, vol. 130, no. 3, pp. 1272–1281, 2011.

[90] S. D. Blunt and K. Gerlach, “Adaptive pulse compression via MMSE estimation,” *IEEE Transactions on Aerospace and Electronic Systems*, vol. 42, pp. 572–584, April 2006.

[91] S. M. Kay, *Fundamentals of Statistical Signal Processing: Estimation Theory*. Upper Saddle River, NJ, USA: Prentice-Hall, Inc., 1993.

[92] L. Rayleigh, “Xxxi. investigations in optics, with special reference to the spectroscope,” *Philosophical Magazine Series 5*, vol. 8, no. 49, pp. 261–274, 1879.

[93] "Definition of Rayleigh criterion in English." `https://en.oxforddictionaries.com/definition/rayleigh_criterion`. Oxford Dictionaries, [Online; accessed: 2017-06-20].

[94] A. Das, D. Zachariah, and P. Stoica, "Comparison of two hyperparameter-free sparse signal processing methods for direction-of-arrival tracking in the hf97 ocean acoustic experiment," *IEEE Journal of Oceanic Engineering*, vol. PP, no. 99, pp. 1–10, 2017.

[95] A. Balleri, *Biologically inspired radar and sonar target classification.* PhD thesis, University College London, Department of Electronic and Electrical Engineering, December 2010.

[96] R. Lyons, "Digital envelope detection: The good, the bad, and the ugly." `https://www.dsprelated.com/showarticle/938.php`, 2016. [Online; accessed 25-April-2017].

[97] R. F. Lyon, A. G. Katsiamis, and E. M. Drakakis, "History and future of auditory filter models," in *Proceedings of 2010 IEEE International Symposium on Circuits and Systems*, pp. 3809–3812, May 2010.

[98] J. R. Klauder, A. C. Price, S. Darlington, and W. J. Albersheim, "The theory and design of chirp radars," *Bell System Technical Journal*, vol. 39, pp. 745–808, 7 1960.

[99] E. Zauderer, *Partial Differential Equations of Applied Mathematics.* Wiley-Interscience, 2006.

[100] S. P. Dear, J. Fritz, T. Haresign, M. Ferragamo, and J. A. Simmons, “Tonotopic and functional organization in the auditory cortex of the big brown bat, eptesicus fuscus,” *Journal of neurophysiology*, vol. 70, no. 5, pp. 1988–2009, 1993.

[101] S. Hoffmann, U. Firzlaff, S. Radtke-Schuller, B. Schwellnus, and G. Schuller, “The auditory cortex of the bat phyllostomus discolor: Localization and organization of basic response properties,” *BMC Neuroscience*, vol. 9, no. 1, pp. 1–17, 2008.

[102] *MATLAB and Curve Fitting Toolbox Release 2015a, User’s Guide*. Natick, Massachusetts, United States: The MathWorks, Inc., 2015.

[103] B. R. Mahafza, *Radar Systems Analysis and Design Using MATLAB Third Edition*. Chapman and Hall/CRC, 2013.

[104] A. W. Rihaczek and S. J. Hershkowitz, *Radar resolution and complex-image analysis*. Boston : Artech House, 1996.

[105] A. W. Rihaczek and S. J. Hershkowitz, *Theory and practice of radar target identification*. Boston : Artech House, 2000.

[106] Anritsu Company, Texas 75081, USA, *The Essentials of Vector network Analysis*, 2009. PN: 11410-00476A.

[107] A. Papoulis, “A new algorithm in spectral analysis and band-limited extrapolation,” *IEEE Transactions on Circuits and Systems*, vol. 22, pp. 735–742, September 1975.

[108] R. Gerchberg, “Super-resolution through error energy reduction,” *Optica Acta: International Journal of Optics*, vol. 21, no. 9, pp. 709–720, 1974.

[109] M. I. Grace, *Measurement of Radar Cross Section Using the “VNA Master” Handheld VNA*. Anritsu Company, Texas 75081, USA, B ed., 9 2011. PN: 11410-00604.

[110] A. W. Rihaczek and S. J. Hershkowitz, "Man-made target backscattering behavior: applicability of conventional radar resolution theory," *IEEE Transactions on Aerospace and Electronic Systems*, vol. 32, pp. 809–824, April 1996.

[111] D. E. Hack, L. K. Patton, B. Himed, and M. A. Saville, "Detection in passive mimo radar networks," *IEEE Transactions on Signal Processing*, vol. 62, pp. 2999–3012, June 2014.

[112] E. J. Candès, J. K. Romberg, and T. Tao, "Stable signal recovery from incomplete and inaccurate measurements," *Communications on Pure and Applied Mathematics*, vol. 59, no. 8, pp. 1207–1223, 2006.

[113] D. L. Donoho, "Compressed sensing," *IEEE Transactions on Information Theory*, vol. 52, pp. 1289–1306, April 2006.

[114] S. Ioffe and C. Szegedy, "Batch normalization: Accelerating deep network training by reducing internal covariate shift," in *Proceedings of The 32nd International Conference on Machine Learning, pp. 448–456, 2015*, vol. 37, (Lille, France), pp. 448–456, 2015.

[115] A. Stove. private communication, 2017.

[116] LinearX Systems Inc., Tualatin, OR, United States, *LT360EX Precision Turntable User Manual*, 2010. PN: 910-0019.

[117] R. G. Lyons, *Understanding Digital Signal Processing*, vol. 1. Pearson Education, 2010.

[118] S. W. Smith, *The scientist and engineer's guide to digital signal processing*. California Technical, 1997.